Sensor based mitigation of implant related RF safety hazards in MRI by E-field steering

Dissertation
zur Erlangung des akademischen Grades
Doktoringenieur
(Dr.-Ing.)

Von
M.Sc. Berk Silemek
geb. am 18.12.1990 in Ankara, Türkei

genehmigt durch die Fakultät für Elektrotechnik und Informationstechnik
der Otto-von-Guericke-Universität Magdeburg

Gutachter:

Prof. Dr. rer. nat. Georg Rose
Prof. Dr. rer. nat. habil. Oliver Speck
Prof. Dr. rer. nat. Michael Bock

Einreichung am 11.05.2023
Promotionskolloquium am 07.12.2023

Summary

MRI is a state-of-the-art medical imaging technology utilizing non-ionizing electromagnetic radiation to generate images of the body with high soft-tissue contrast. However, MRI of patients with implants has the potential risk of excessive RF-induced tissue heating. The RF field of the scanner may couple to the metallic conductors of the implants and increase the power absorption. The problem cannot be precisely solved due to the variety of patient, device, and exam-specific configurations, although the underlying physical and physiological aspects of RF-induced tissue heating are well-established. Currently, implant manufacturers are solely responsible to demonstrate compliance of their devices with applicable standards. Often, their compliance settings require using low-power MRI, which results in poorer diagnostic capability of the MR images. In order to maintain diagnostic imaging capabilities and lower the risk for RF-induced heating, mitigation strategies are needed. One promising technique is the so-called parallel transmission (pTx). By exploiting the additional degrees of freedom of a pTx system, the induced E-fields around the implant can be suppressed and the rest of the tissue can be imaged without the risk of implant-related RF burns. To characterize the pTx settings in terms of implant safety, the E-field or temperature rise must be known. Sensors embedded in implants could provide measurements from these critical components that can be used to steer the RF settings of the MR system to guarantee the safe scanning of patients with implants. In this thesis, measurement-based methods to assess and mitigate the RF-induced heating of the implants by using parallel transmission are investigated. First, a pTx implant safety testbed was developed allowing to systematically investigate different sensors, scenarios, and pTx safety settings. Next, a real-time pTx mitigation method based on time-domain E-field probes was implemented. This method was further developed and applied to miniaturized root-mean-square sensors, which can be embedded in realistic implant hardware. Finally, a proof-of-concept study is presented, which resembles a clinically relevant setting, using a wireless reference implant with embedded sensors together with realistic implant lead trajectories from patients with deep brain stimulation devices. In summary, this thesis conceptualizes and demonstrates “smart” implants with embedded sensors communicating with the MRI scanner for the RF safety of patients with implants.

Zusammenfassung

MRT ist eine hochmoderne medizinische Bildgebungstechnologie, die nichtionisierende elektromagnetische Strahlung verwendet, um Bilder des Körpers mit hohem Weichteilkontrast zu erzeugen. Die MRT von Patienten mit Implantaten birgt jedoch das potenzielle Risiko einer übermäßigen HF-induzierten Gewebeerwärmung. Das HF-Feld des Scanners kann mit dem metallischen Leiter des Implantats koppeln und die Leistungsabsorption erhöhen. Das Problem kann aufgrund der Vielzahl von patienten-, geräte- und untersuchungsspezifischen Konfigurationen nicht genau gelöst werden, obwohl die zugrunde liegenden physikalischen und physiologischen Aspekte der HF-induzierten Gewebeerwärmung gut bekannt sind. Derzeit sind Implantathersteller allein dafür verantwortlich, die Konformität ihrer Produkte mit den geltenden Normen nachzuweisen. Häufig erfordern ihre Compliance-Vorgaben die Verwendung von Low-Power-MRT, was zu einer schlechteren Diagnosefähigkeit der MR-Bilder führt. Um die Möglichkeiten der diagnostischen Bildgebung aufrechtzuerhalten und das Risiko einer HF-induzierten Erwärmung zu verringern, sind Minderungsstrategien erforderlich. Eine vielversprechende Technik ist das sogenannte parallele Senden (pTx). Durch Ausnutzung der zusätzlichen Freiheitsgrade eines pTx-Systems können die induzierten E-Felder um das Implantat herum unterdrückt und der Rest des Gewebes ohne das Risiko von implantatbedingten HF-Verbrennungen abgebildet werden. Zur Charakterisierung der pTx-Einstellungen muss das E-Feld oder der Temperaturanstieg bekannt sein. In Implantate eingebettete Sensoren könnten Messungen dieser kritischen Größen liefern, die zur Steuerung der HF-Einstellungen des MR-Systems verwendet werden können, um ein sicheres Scannen von Patienten mit Implantaten zu gewährleisten. In dieser Arbeit werden messtechnische Methoden zur Beurteilung und Minderung der HF-induzierten Erwärmung der Implantate durch paralleles Senden untersucht. Zunächst wurde ein pTx-Implantat-Prüfstand entwickelt, der es ermöglicht, verschiedene Sensoren, Szenarien und pTx-Sicherheitseinstellungen systematisch zu untersuchen. Als nächstes wurde eine Echtzeit-pTx-Milnderungsmethode basierend auf Feld-Sonden für zeitaufgelöste E-Feld-Messungen konzipiert. Dieses Verfahren wurde weiterentwickelt und auf miniaturisierte Effektivwertsensoren angewendet, die in realistische Implantathardware eingebettet werden können. Schließlich wird eine Proof-of-Concept-Studie vorgestellt, die eine klinisch relevante Situation nachbildet und eingebettete Sensoren auf einem drahtlosen Referenzimplantat verwendet, dessen Trajektorien den Elektroden von Tiefenhirnstimulationsgeräten realistisch nachgebildet sind. Zusammenfassend konzipiert und demonstriert diese Arbeit „smarte“ Implantate mit eingebetteten Sensoren, die mit dem MRI-Scanner für die HF-Sicherheit von Patienten mit Implantaten kommunizieren.

Table of Contents

List of Abbreviations

ADC	Analog to Digital Converter
AIMD	Active Implantable Medical Devices
ASTM	American Society for Testing and Materials
BLE	Bluetooth Low Energy
BY	By Attribution
CC	Creative Commons
CEM43	Cumulative Equivalent Minutes at 43 ℃
COSI	Cost Effective Open Source Imaging
CP	Circularly Polarized
DAC	Digital to Analog Converter
DBS	Deep Brain Stimulator
FA	Flip Angle
FBG	Fiber Bragg Grating
FDTD	Finite Difference Time Domain
fMRI	Functional Magnetic Resonance Imaging
FOV	Field of View
GRE	Gradient Echo
GUI	Graphical User Interface
LSB	Least Significant Bit
IEC	International Electrotechnical Commission
ISO	International Organization for Standardization
OP	Orthogonal Projection
MoTLiM	Modified Transmission Line Method
MRI	Magnetic Resonance Imaging
NC	Non Commercial
ND	Non Derivative
NM	Null Modes
NTC	Negative Thermal Coefficient
PIN	Positive-Intrinsic-Negative
ppm	Parts Per Million
pTx	Parallel Transmission
PVP	Polyvinylpyrrolidone
RF	Radiofrequency
RMS	Root Mean Square
ROI	Region of Interest
RS	Recommended Standard
SAR	Specific Absorption Rate
SI	Signal Intensity
SMA	Subminiature Version A
SNR	Signal to Noise Ratio
SoC	System on Chip

TD	Time Domain
TDS	Time Domain Sensor
TE	Echo Time
TR	Repetition Time
TS	Technical Specification
UART	Universal Asynchronous Receiver-Transmitter
UHF	Ultra High Field
USB	Universal Serial Bus
WC	Worst Case

1. Introduction

Life expectancy has increased in many countries compared to 50 years ago and it is highly correlated with accessible healthcare systems.[1] Healthcare systems utilize medical devices for various diagnostic and/or therapeutic purposes. MRI is one of the best diagnostic tools, allowing non-invasive imaging of the soft tissue with high contrast and functional characteristics of the organs (i.e., brain connectomes) without harmful ionizing radiation. Another established healthcare tool are implantable medical devices that are commonly used for therapeutic purposes. Millions of people with implantable devices may require an MRI examination; however, MRI of patients with implantable devices is often contraindicated because of safety concerns.[2,3]

MRI utilizes static and time-varying electromagnetic fields that interact with nuclei of the Hydrogen atoms in the human body. The static (B_0) magnetic field typically ranges between 0.5-7T in most of today's clinical MRI systems. The time-varying gradient fields (f = 0-10 kHz) alter B_0 for spatial encoding. Another time-varying electromagnetic field is the RF magnetic field B_1 (f = 21-297 MHz), which is generated by the radiofrequency (RF) coils to tilt spin isochromat.

These fields pose a safety concern to patients and staff, and therefore, must be rigorously regulated. For example, ferromagnetic objects can be attracted by the "invisible" B_0-field, and may cause fatal incidents.[4,5] The gradient system may induce currents on the peripheral nerve system, stimulating the skeletal muscles or myocardium.[6,7] Moreover, biological tissues absorb the transmitted RF fields which is transformed into tissue temperature increase. Therefore, MR safety is regulated by international standards.[8] MR manufacturers have the sole responsibility to implement the defined safety mechanisms in their systems. On top of these safety hazards, a growing number of patients that require an MRI exam have medical implants, which pose an additional safety risk.

Implantable medical devices are devices that are immersed into the human body, partially or as a whole, by a clinical procedure, and intended to remain for at least 30 days.[9] These devices can further be categorized into passive implantable

medical devices or active implantable medical devices (AIMDs). The term “active” is used when the device needs external energy, non-human generated, source to function. Many passive implants such as certain protheses do not necessarily consist of metallic components. AIMDs, however, by definition, have an external power generator and highly conductive metallic components for their functional purposes. Many types of these devices, such as deep brain stimulators (DBS), cardiac pacemakers, and spinal cord stimulators interact with the target tissue by using a metallic lead with a tip electrode.

1.1. MR safety of patients with implants

The metallic components of the implants may interact with the electromagnetic fields produced during an MRI examination. The scanner’s B_0 field may induce a torque on the implants that causes dislodgment, either due to ferromagnetic materials used in the implant or due to induced currents in electrically conductive components.[10] Moreover, the ferromagnetic materials inside the implants may disturb the B_0 field, affecting the diagnostic quality of the images.[11] Increasing the slew-rate of the gradient fields may induce eddy currents on the surface of the large implants (i.e. hip implants) and heat the surrounding tissue.[12–15] Fast slew-rates affect not only the passive implants; AIMDs may malfunction because of the time-varying gradient and RF fields.[10,11] One of the most common contraindications to scan patients with AIMDs is caused due to the interaction between RF fields and the long conductors of AIMDs.[2,16] Currents are being induced on the conductors leading to secondary E-fields that may amplify the local specific absorption rate (SAR) substantially. The amplified SAR can drastically elevate tissue temperature, then, inducing tissue damage. A serious threat, which is confirmed by multiple reported incidents of RF-induced heating during MRI scans of patients with AIMDs.[17,18]

AIMDs such as cardiac pacemakers or neurostimulators typically consist of a housing containing the electronics connected over a long electrically insulated lead to an uninsulated electrode tip. In this setup, SAR amplification occurs mostly at the implant tip and the induced E-field amplitude depends on parameters such as the E-field distribution and amplitude of transmitted by the RF coil, the average

RF power determined by the imaging technique and the transmitted RF frequency.[19] The patient-specific properties such as tissue electrical conductivity and permittivity, and implant position or implant lead trajectory alter the amount of induced E-field.[2] Furthermore, electrical length of the leads, insulation thickness, dielectric constant, and termination impedance of the lead wire are device-specific electromagnetic variables that influence tip heating.[20]

1.2. The standards for RF safety practice with implants

The regulatory bodies mandate implant manufacturers to demonstrate compliance of their devices, e.g., by guaranteeing safe SAR limits during MR scans. The standard American Society for Testing and Materials (ASTM), currently referred to as ASTM International, introduced three labeling categories for the devices used in MRI.[21] The term *MR safe* describes the devices that present no known safety hazard and can be used in all MR environments. *MR unsafe* label is given to the devices that pose known safety hazards in all MR environments. *MR Conditional* devices do not pose known safety hazards in the MR environment within specific settings and conditions. Implants have metallic components, which create at least an image artifact that can create diagnostic hazards; therefore, they cannot be *MR safe*.[22] Any non-specified MRI of patients with implants beyond the manufacturer's guidelines is referred to as "off-label" use and has potentially severe implications for the technologist/MRI operator.[23] The most common off-label use of implants is scanning patients with non-MR conditional pacemakers.[24,25]

One relevant standard to evaluate RF-safety of passive implants is ASTM F2182.[26] This standard covers test methods to evaluate passive implant heating for whole-body 2 W kg^{-1} SAR for 1.5T and 3T environments produced by a body-coil in a circularly polarized (CP) RF-field. Although it is limited to passive implants, the described techniques can be applied and suitable for AIMDs.

The International Electrotechnical Commission (IEC) 60601-2-33 is the most pertinent safety and performance standard for an MR device. It briefly touches on the threat of RF-induced heating of the implants.[27] In its latest edition, the

standard introduces the $B_{1,RMS}^{+}$ measurand to assess RF-induced heating. $B_{1,RMS}^{+}$ is well-calibrated in the MR scanners for typical CP excitation and, by the standard, it should be displayed in the scanner software.

The most recent and comprehensive standard for the MR safety of AIMDs is International Organization for Standardization/Technical Specification (ISO/TS) 10974:2018.[28] It specifically defines procedures for the implant manufacturers to assess the compliance of their devices for MR safety. It is specific to scanners with a 1.5T field strength and cylindrical body-coil transmission. For the RF safety of AIMDs, it prescribes a four-tiered approach. Each tier has its compromise between accuracy and complexity. No electromagnetic modeling must be performed for the *Tier 1* approach. *Tier 2* requires the simulated E-fields in the implant volume. In *Tier 3*, the AIMD should be modelled electromagnetically, and the transfer function[29] must be determined either via simulations or experimental measurements. *Tier 4* is the most complex one because it requires the full electromagnetic simulation by modeling the AIMD together with the corresponding electromagnetic properties of the tissue by using realistic anatomical models. For *Tier 4*, the required electromagnetic simulations may challenge state-of-the-art computational abilities.

In reality, due to its complexity only few implant manufacturers engage in a *Tier 4* approach for MR conditional labeling. And even if, the patient, exam, and device specific (both MR and implant) degrees of freedom to correctly assess the induced SAR are large, resulting in overly conservative RF power limits for an MRI exam, strongly impacting imaging quality. For example the SAR limit for head imaging of a patient with an *MR conditional* DBS implant is reduced from 3.2 W kg^{-1} in normal mode when scanning a patient without implant to only 0.2 W kg^{-1}.[8,30] More advanced mitigation methods are needed to exploit the potential of MRI of patients with implants.

1.3. Mitigation methods for RF related hazards

In most commercial 1.5T and 3T MRI systems, only the CP mode is available using a body RF coil. Such a single transmit mode cannot be changed and, therefore,

only magnitude and duration of the RF power can be adjusted during imaging. Therefore, first attempts to mitigate RF-induced heating focused on the development of low-SAR imaging techniques or implant engineering, because the RF field distribution of the MRI hardware could not be changed. These device-specific innovations included lead modifications[31–37], active electrical circuits[38,39], or the use of MRI-compatible materials.[40]

The concept of using multi-channel RF transmission, so-called parallel transmission (pTx), to shape the RF excitation in the region of interest first emerged in hyperthermia studies[41–44]; later, in MRI.[45–48] This technique empowers independent adjustments of the RF excitation parameters (i.e., amplitude, phase and waveform) of multichannel RF transmit coils. This increased degree of freedom grants steering the hazardous E-field away from the implant, and substantially minimizes RF-induced currents, simultaneously preserving the overall imaging quality elsewhere.[49–65] To precisely perform such adaptations of the E-field and B_1^+; the induced implant current, field, or temperature rise needs to be known.

Electromagnetic simulation tools provide a good understanding and estimations for the E-field distribution and temperature rise by using virtual human models or complex implant lead trajectories.[66–68] However, simulations are still not patient and exam-specific and variations between models, implant positions and RF transmission conditions may alter the induced tip SAR significantly.[58,69] This uncertainties can only be accounted for by large safety margins, resulting in a frequent overestimation of the actual safety risk. Therefore, alternative measurement-based methods are needed for an accurate risk determination in vivo and in situ.

Measurement-based methods for pTx mitigation of implant heating are rare because dedicated pTx hardware is not readily accessible. One proposed method uses MR images to estimate RF-induced implant currents and to steer the E-field away from the implant.[56,57] The major drawback of this method is the additional time required to acquire the MR images and its robustness to imaging artifacts that may impact the pTx mitigation results. In addition, patient and/or RF coil

motion may also alter SAR,[70,71] thus questioning the validity of this approach for long-lasting measurements.

Another measurement-based technique uses external time-domain (TD) current sensors that can be mounted on implant wires to find an RF excitation vector that minimizes the currents on the conductor wire.[61,72,73] Although fast measurements are possible, it appears difficult if not undoable to implement the proposed bulky current sensors to synchronously detect and mitigate currents in realistic implants. In addition, this technique requires additional B_1^+-mapping to optimize for the MR imaging quality, which naturally increases scan time.

1.4. Sensor-based mitigation of RF induced implant heating

This thesis focuses on novel measurement-based pTx mitigation methodologies using embedded sensors in implants, which prevent hazardous E-field distributions and simultaneously preserve imaging quality. The work can be extended to a novel safety concept, where an AIMD can communicate with an MR scanner in order to assess and mitigate RF induced implant heating without disturbing the current clinical workflow. In order to reach this goal, extensive hardware developments were performed, and rigorous test methods were implemented and investigated to prove its feasibility. The thesis is structured as follows:

1) Development and construction of the necessary hardware to perform automated experimental evaluations for RF safety testing of implants under various RF exposure scenarios. A modular and scalable pTx implant safety testbed is introduced for this purpose.

2) Development of pTx-based methodology to utilize a sensor-signal and perform sensor-based mitigation of RF-induced heating while MR imaging quality is maintained. The developed pTx mitigation methodology is initially applied and demonstrated using external time-domain E-field sensors. Then, the method is extended to phase-insensitive miniaturized root-mean-square (RMS) sensors that can be potentially embedded in a realistic implant casing or at the implant tip.

3) Development and translation of the sensor-based mitigation of RF-induced heating to realistic exposure conditions within a 3T MRI by using home-built wireless implant hardware with embedded RMS sensors that can communicate with the MR systems. In this setting, several realistic implant lead trajectories derived from patient data of DBS devices are implemented to successfully detect the RF heating hazard and substantially reducing it by adjusting the pTx transmission settings, automatically.

The work presented in this thesis was performed as part of the projects “Medical Implant Manufacturers’ Safety Procedures (MIMAS)”[74] and “Standardisation for safe implant scanning in MRI (STASIS)”.[75]

2. Theoretical background

When a patient, regardless of an implant being present, is scanned with an MRI machine, three different electromagnetic fields are utilized to create an MR image:

1) Static magnetic field B_0 (~0.5-7T) generated by the MR magnet
2) Time-varying G_x, G_y, G_z (<10 kHz) magnetic fields generated by the gradient coils
3) Time-varying B_1 (~20-300 MHz) magnetic field generated by the RF coils

In a static magnetic field[1], B_0, a transversal magnetization precesses at an intrinsic Larmor frequency, ω_0, which is a function of the gyromagnetic ratio, γ, (26.75105×10^7 for hydrogen) and can be written as $\omega_0 = \gamma B_0$. The net magnetization, $\boldsymbol{M}$ is in the same direction as B_0 which can be perturbed by a time-varying electromagnetic field, B_1, at Larmor frequency oriented perpendicular to B_0 with B_0 in z-direction. Then, the variation in the magnetization can be written using the Bloch equation[76]:

$$\frac{d\boldsymbol{M}}{dt} = \gamma \boldsymbol{M} \times \boldsymbol{B} - \frac{M_x \hat{\boldsymbol{\imath}} + M_y \hat{\jmath}}{T_2} - \frac{(M_z - M_0)\hat{k}}{T_1} \tag{2.1}$$

where, M_0 is the steady-state magnetization in the z-direction, $\boldsymbol{B}$ is the vector sum of all applied magnetic fields (i.e., $\boldsymbol{B} = B_0\hat{k} + B_1\hat{\imath} + B_1\hat{\jmath}$), M_x, M_y and M_z are the magnetization components in the cartesian coordinate system, $\hat{\imath}$, $\hat{\jmath}$ and $\hat{k}$ denotes the unit vector components along the x, y and z axes, T_1 and T_2 are the longitudinal and transversal relaxation times, respectively, describing the magnetization's return back to equilibrium. They are tissue dependent and ultimately determine the MR imaging contrast. While B_0 and B_1 make the basis of the magnetic

[1]Please note that the term magnetic flux density, B is often referred as "magnetic field" in the MR context, which is closely related to the term magnetic field intensity, H. This relationship can be represented using the permeability constant, μ, as B = μH. In addition, bold notation is used for the vectoral components except for the named fields B_0 and B_1.

resonance, the gradient fields ($\boldsymbol{G}$) are needed for spatial encoding, i.e. they manipulate the magnetization suitably to create an MR image.[77]

RF coils or antennas generate the time-varying B_1, which according to the Maxwell-Faraday equation is accompanied by an E-field:

$$\boldsymbol{\nabla} \times \boldsymbol{E} = -\partial \boldsymbol{B}/\partial t \tag{2.2}$$

where, $\boldsymbol{\nabla} \times$ is the curl operator and $\boldsymbol{E}$ denotes electric field vector and ∂ denotes partial derivative operation. In the investigated range of RF transmission frequencies the E-field is the main contributor to RF-induced heating through molecular vibration and rotation due to ionic and electric currents.[78]

2.1. RF safety in MRI

In general, the analysis of RF safety, regardless of an implant being present, can be divided into four different components as shown in Figure 2.1. The presence of a conductive implant does not change the steps but complicates the problem since electrically conductive implant components change the RF field distribution in tissue. In this chapter, RF safety of implants is introduced alongside techniques that are presently used to assess and ensure implant safety in MRI.

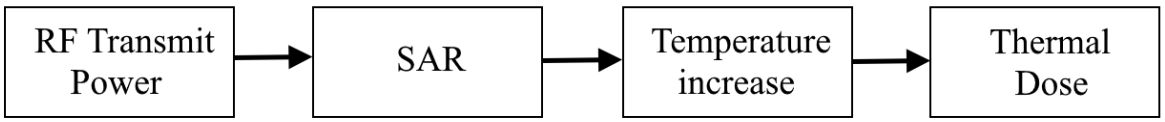

Figure 2.1 Schematic of components involved in RF safety.

Under time-varying RF fields, the current density $\boldsymbol{J}$ in tissue can be written as:

$$\boldsymbol{J} = \sigma \boldsymbol{E} \tag{2.3}$$

where, σ is the frequency and position dependent electrical conductivity of tissue. The relationship between the transmitted power from the source ($\boldsymbol{P_s}$) (e.g., from a RF coil) to the tissue can be expressed using the Poynting theorem, which uses the conservation of energy.[79(pp264-267),80(pp528-529)] The source power is equal to the sum of the dissipated power ($\boldsymbol{P_d}$) at the tissue volume due to the Ohmic losses

(thermal interactions), and the radiated electromagnetic power ($\boldsymbol{P_r}$): $-\boldsymbol{P_s} = \boldsymbol{P_d} + \boldsymbol{P_r}$ as follows

$$-\frac{1}{2}\iiint_V Re(\boldsymbol{J}^* \cdot \boldsymbol{E})dV = \frac{1}{2}\iiint_V \sigma|\boldsymbol{E}|^2 dV + \frac{1}{2}\oiint_{\partial V} Re(\boldsymbol{E} \times \boldsymbol{H}^*)\, ds \tag{2.4}$$

The symbol asterisk denotes complex conjugate operation and ∂V represents boundary surface of the volume, where electromagnetic energy is radiated. Then, the power absorbed per unit mass of the tissue can be formulated as specific absorption rate, SAR:

$$SAR = \frac{1}{V}\int_V \frac{\sigma|\boldsymbol{E}|^2}{2\rho} dV \tag{2.5}$$

where, ρ is the mass density of the tissue. SAR is used by current safety standards[8,26,28] as a measure to limit the transmitted RF power by an MRI scanner to prevent excessive tissue heating. The spatial averaging over volume (V) depends on the mass of tissue that is being used, with three different values defined by current standards: 1) *whole-body* SAR is used when SAR is averaged over the whole body 2) partial body SAR when averaged over a certain sub-volume of the human body[8] and 3) local SAR, which is usually based on a 10g average to assess local exposure. The E-field depends on the MR settings such as transmit coil (transmit coil efficiency, coil geometry) or sequence parameters (shape, duration, number and peak power of the transmitted RF pulses). SAR distribution is position and frequency dependent, as illustrated in Figure 2.2. In addition, although tedious methods such as MR-based electrical properties tomograpy[81] exist, SAR cannot be directly measured by an MR scanner because B_1^+ component is measurable in MRI. Therefore, human body models are typically used and simulated in numerical electromagnetic field simulations to estimate SAR in MRI and limit RF powers to safe transmission levels.

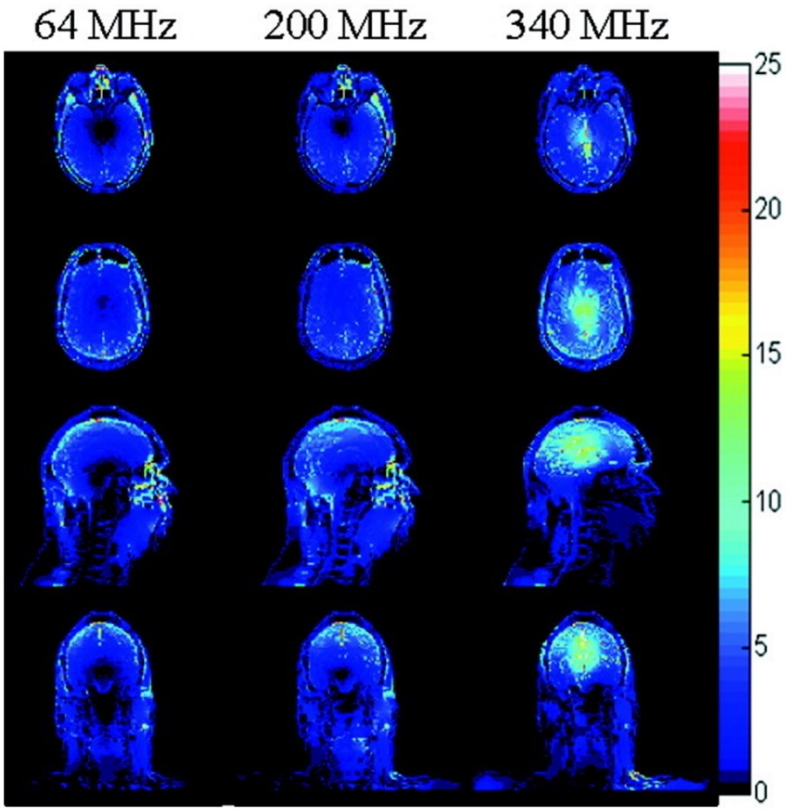

Figure 2.2 An example of SAR distributions of a head model at different RF transmission frequencies (corresponding to 1.5T, 4.7T, and 8T). SAR peaks at different locations and increases at higher frequencies. (Reproduced with permission from the Reference [82] © Wiley-Liss Inc.)

The dissipated power is converted to temperature rise (dT/dt). For homogenous, non-perfused tissue without heat conduction, it is linearly proportional to SAR:

$$SAR = c\frac{dT}{dt} \tag{2.6}$$

where c is the specific heat of the material. Equation (2.6) is only valid for a very short time period because SAR and c are non-uniform (Figure 2.2) and induce non-uniform temperature rise, which diffuses over time, e.g. via thermal conduction or perfusion. In addition, the body compensates for the temperature rise by various thermoregulation mechanisms such as perfusion. These effects are included in Penne's Bioheat Equation:

$$c\frac{dT_t}{dt} = \nabla \cdot \left(\frac{k}{\rho}\nabla T\right) + \rho_b w c_b (T_b - T) + SAR + Q_m \tag{2.7}$$

where the Laplacian operator is ∇, the mass density of the perfusing blood is ρ_b and w is the blood perfusion of the tissue, tissue thermal conductivity is k, and the temperature of the perfusing blood is T_b, and Q_m is the heat generated by

metabolic processes in the body. Figure 2.3 shows a comparison of the temperature evolution according to Equation (2.6) and Equation (2.7) for different tissue types.

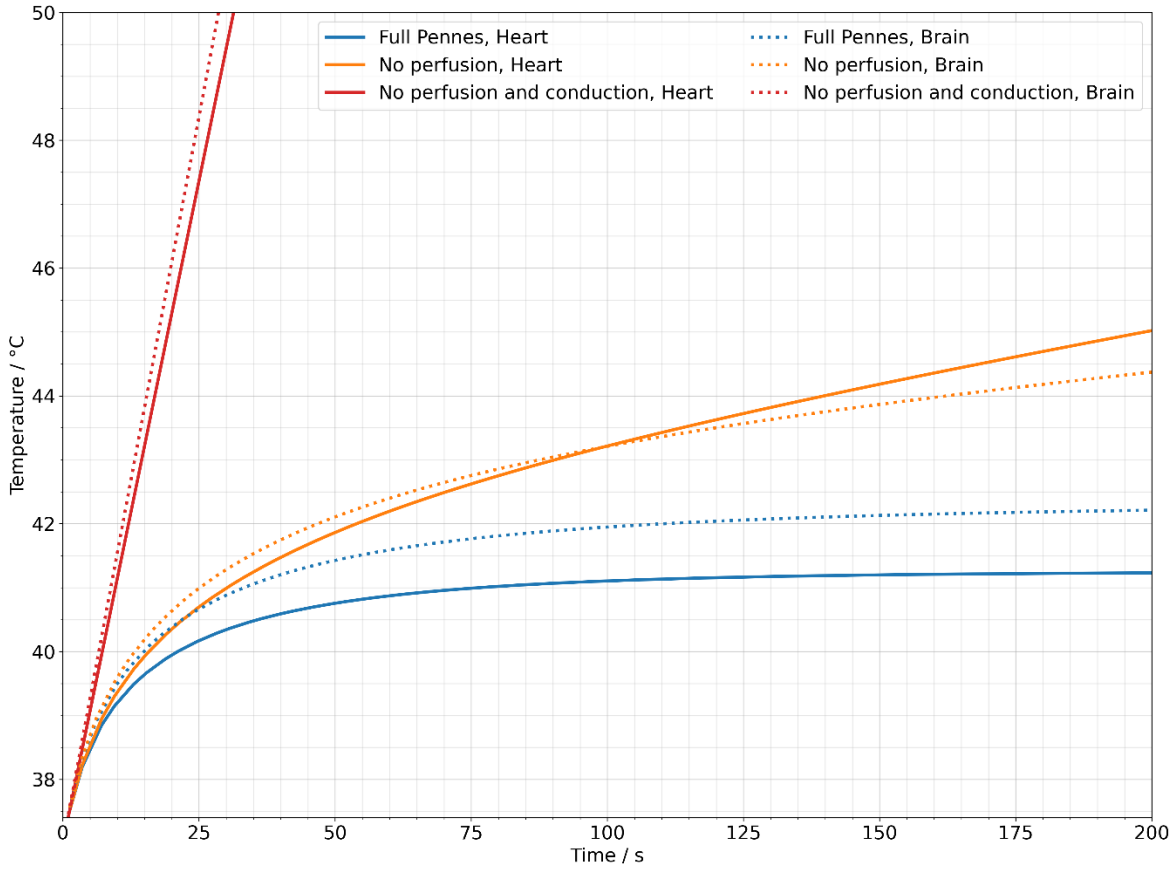

Figure 2.3 Illustration of temperature elevation of brain and heart tissues for the same RF exposure but, under different temperature models. Without conduction and perfusion (in red), temperature increases proportional to the applied power as described in Equation (2.6).

Ultimately, the risk of damage to the tissue is not only dependent on the tissue temperature, but also the duration and tissue type it is applied to. This is implemented in the thermal dose concept originating from hyperthermia studies. One widely used concept to quantify thermal dose, is the “cumulative equivalent number of minutes at 43 ℃” approach (CEM43):

$$CEM43 = \int_0^{T_{exam}} R^{(43℃ - T(t))/℃}\, dt \tag{2.8}$$

where $T(t)$ is the temperature at time point t, R is a constant that is empirically determined and is 0.25 for tissue temperatures 43 ℃ or lower, and 0.5 for temperatures above 43 ℃.[83–86] While the CEM43 concept provides a comprehensive idea behind the mechanisms of tissue damage, in current RF safety practice, SAR is being used predominantly to define safe power limits.

2.2. RF safety of implants and its assessment

Majority of implants consist of highly conductive metallic components present in the lossy body tissue. Therefore, the electromagnetic problem in previous sections needs to be modified because these conductive components alter the electromagnetic field transmitted by RF coils.

Recalling the Maxwell-Faraday Equation (2.2), the time-varying B_1 field generated by the RF coil of the scanner is accompanied by E-fields. A ratio between electric and magnetic waves (assuming a uniform electromagnetic wave traveling in the lossy body medium) can be defined as:

$$\eta_w = \sqrt{\frac{j\omega\mu}{\sigma + j\omega\varepsilon}} \tag{2.9}$$

where, η_w is the wave impedance and ε is the absolute permittivity of the material. The propagating E-field (so-called, background or incident field ($\boldsymbol{E^i}$) in the tissue medium encounters a highly conductive implant boundary (around five magnitudes higher electrical conductivity). This drastic impedance mismatch between tissue and implant is leading to most of the electromagnetic wave being reflected (Illustrated in Figure 2.4). The weak penetrating wave rapidly attenuates depending on the frequency and the electrical characteristics of the material. The depth of E-field amplitude attenuation to e^{-1} is called skin depth, δ and can be approximated as follows:

$$\delta = \left[\omega\sqrt{\mu\varepsilon}\sqrt{0.5\left[\sqrt{1+(\sigma(\omega\varepsilon)^{-1})^2}-1\right]}\right]^{-1} \tag{2.10}$$

$$\cong \sqrt{2(\omega\mu\varepsilon)^{-1}}\,, if\ (\sigma(\omega\varepsilon)^{-1})^2 \gg 1$$

The approximation in Equation (2.10)[87(pp138-143)] is given for the estimation of the skin depth for highly conductive materials. For example, the skin depth for copper at 3T MRI (128 MHz) is about 6 μm. Free charges are accumulated by the incident E-field at this thin surface (Equation (2.3)) and oscillate with the time-varying incident E-field. These induced currents create a secondary E-field on the conductor, which is superposed with the incident E-field (Figure 2.4). The frequency of the oscillation is driven by the incident E-field; however, the amplitude and the phase distribution of the current on the conductor does not only depend on the incident E-field but is modulated by surrounding medium and conductor's electrical properties.

The secondary E-field is scattered at the distal end of the conductor because of another impedance mismatch between the conductor and tissue. The amount of the scattered E-field can be magnitudes higher than the incident E-field due to much higher charge density collected over the length of the conductor. This phenomenon is referred as the "antenna effect" as the implant's conductor "collects" the electromagnetic energy and distributes it from its distal end, where the scattered peak E-field at the tip approximately occurs when the implant length is close to the half of the RF wavelength in the surrounding tissue medium, so called "resonance length".[88,89] Wavelength for the homogeneous medium to make a very coarse approximate for the conductor resonance can be calculated as:

$$2\pi\left[\omega\sqrt{\mu\varepsilon}\sqrt{0.5\left[\sqrt{1+(\sigma(\omega\varepsilon)^{-1})^2}+1\right]}\right]^{-1} \tag{2.11}$$

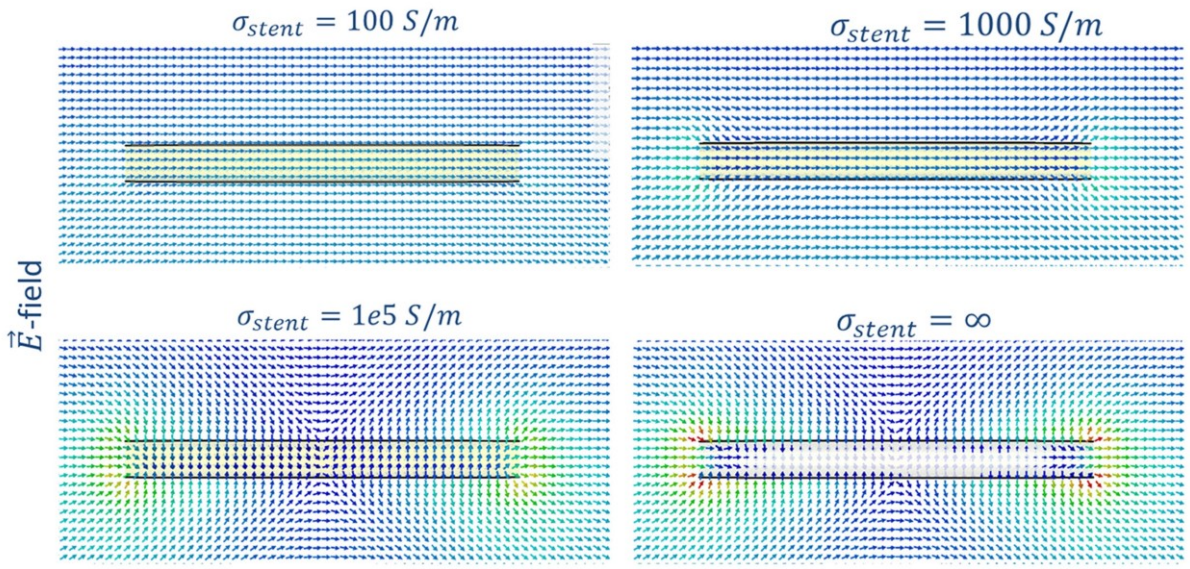

Figure 2.4 Illustration of E-fields for a metallic stent with different electrical conductivities to illustrate highly conductive materials under the same E-field distribution confines the E-field around the distal ends and behaves like an antenna and amplifies the E-field even larger than the incident E-field. (Reproduced from the Reference [2] CC BY 4.0, 2021).

The abovementioned equations in the previous chapter still hold for the scattered E-field, but with an aggravated risk of tissue heating because of its much higher intensity. However, finding a general solution to the risk of RF-induced heating of implant is not trivial because:

1) The incident E-field must be known to relate RF-induced currents on the wire, which is a patient-specific problem and usually generalized as introduced in the SAR calculations for a patient without implant.
2) Assuming patient tissue properties are known and the incident E-field on the tissue can be calculated; then, the path of implant must be known since only tangential component of the incident E-field induces currents on the implant.
3) The electrical properties of the implant, (e.g., conductance, permittivity or capacitance, inductance, insulation thickness) needs to be known as the RF-induced current is modulated by them.
4) The thermal burden to the tissue at the highly localized point (implant tip) SAR needs to be determined, which may require higher resolution temperature calculations.

Each component has its own challenges; however, they are needed for the complete RF safety assessment. The simplifications of the problem might be necessary; however, the uncertainty must be known for an accurate risk assessment. The following section introduces a detailed analysis for the RF safety problem of implants, the apprehension of which is indispensable for the procurement of a refined resolution through the proposed measurement-based methods in the thesis.

2.2.1. Numerical simulations

Numerical electromagnetic and thermal simulations are a vital part of today's implant RF safety assessments.

To solve the complex electromagnetic problem of an implant in the human body: 1) the RF coil field distribution 2) The electromagnetic properties of the implant and 3) the electromagnetic properties of the implant's surrounding, i.e. the human body needs to be known. Currently, most of the advanced electromagnetic solvers are capable of solving these complex models using virtual human models.[66,90]

Time-domain or frequency domain solvers can be utilized for the partial differential or integral forms of Maxwell's equations.[91] One challenge for the simulation approach to implant safety is the sample size difference between RF coil e.g. a whole body coil and the much smaller implant. Therefore, an RF coil and patient, for example, could be resolved using coarse grids (i.e., ~17 million cells) and much smaller implant's structure can be resolved using fine grids (i.e., ~2.5 million, for straight wire; ~15 million voxels for helical wires).[92] Therefore, full simulations using fine grids can be computationally demanding and simplifications such as using straight wire instead of helical wires increase the uncertainty.[92] The so-called Huygens' box principle[93] is a widely applied technique to account for different grid sizes for the RF safety assessments using numerical simulations and can be used if the implant does not significantly impact the scattering (S)-parameters of the RF coil.

Another more difficult challenge is the variation of implant parameters (e.g., length, diameter, path, electrical insulation, and conductivity as well as position

and orientation within the human body), various RF coils and electromagnetic differences in human body anatomies, which require a larger set of virtual human body models. The combinations of all these parameters are computationally too expensive, even for advanced electromagnetic simulators. Therefore, several simplifications were implemented to reduce the complexity of implant safety assessment.

2.2.2. Implant modeling

As the implant structure, position and orientation significantly affects the uncertainty and complicates the calculations for safety assessments, several studies proposed methods to simplify the assessment of RF-induced currents in multiple configurations, which are necessary to consider while conducting the experimental analysis.

Safety index

The basic characteristics of the conductive wire such as length and diameter of the wire, insulation thickness, and permittivity can be used to estimate its worst-case behavior (so-called, “resonance length”) that creates maximum RF-heating. The “Safety Index” is a generalized method that was proposed to predict the risk of heating caused by the implant wire using the SAR gain.[20] The SAR gain is calculated for a homogeneous tissue properties first without the implant and then, with the implant. Safety indices for different wire properties can be computed by convolving the Green’s function of the Bioheat equation with the SAR gain.[20] Safety index approximately provides how implant properties can be adjusted such that the resonance length can be avoided as shown in Figure 2.5 Usually, the resonance length for the implant wire can be found at 20 cm for 1.5T and 10 cm for 3T, which is around half of the wavelength (see Equation (2.11)) in the tissue medium. However, this is a general approximation because homogeneous tissue properties and the implant path complicate the problem and are not addressed in the Safety Index calculations.

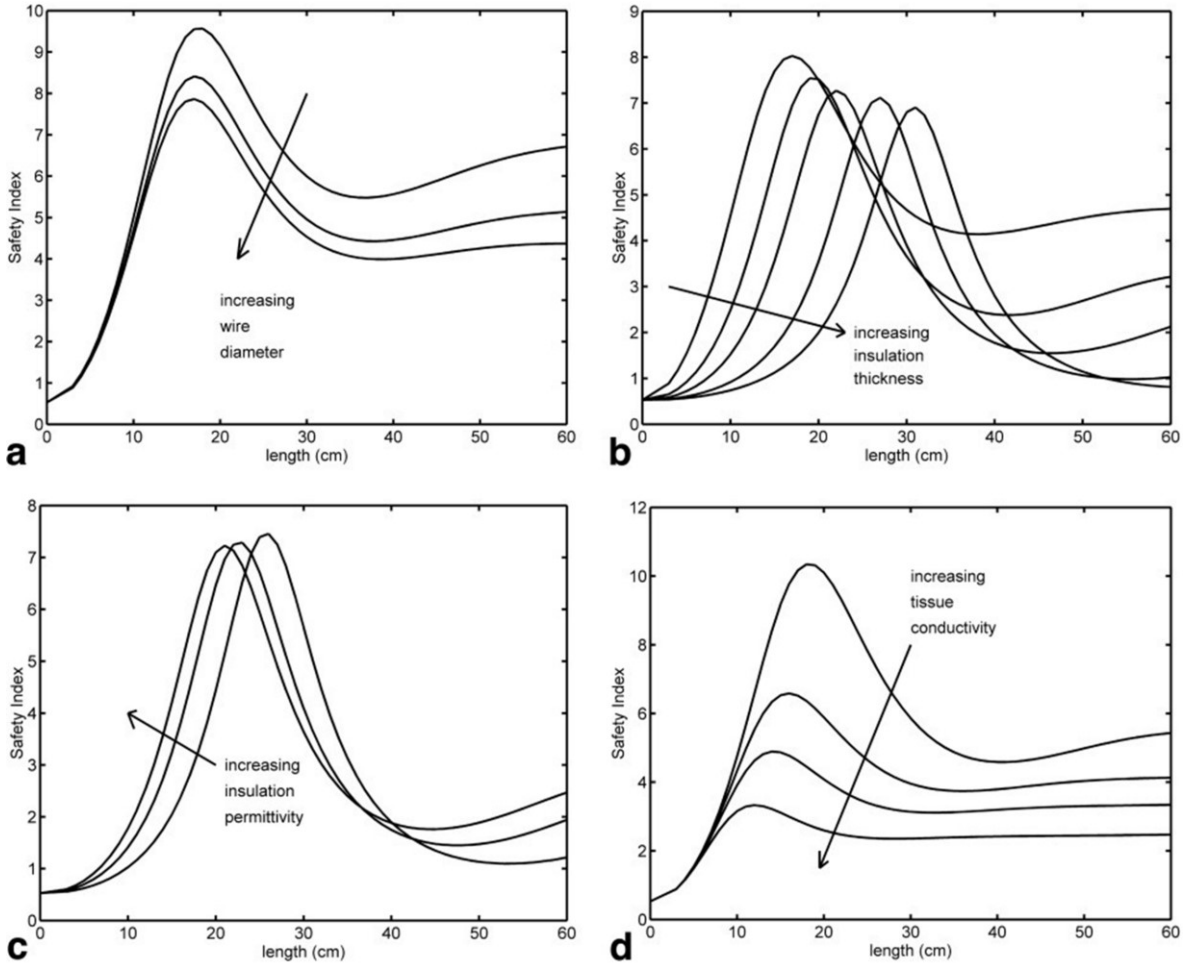

Figure 2.5 Safety index at 1.5T for different implant properties such as: wire diameter, insulation thickness, relative permittivity of insulation and electrical conductivity of tissue. (Reproduced with permission from Reference [20] © John Wiley & Sons, 2002).

Transfer function

The transfer function method is a successor of the safety index, and today it is the de-facto standard for safety assessments of elongated implants.[29] It models the scattered E-field on the implant electrode, denoted as $\boldsymbol{(E_s(p))}$, by applying multiple unit tangential E-field ($E_{tan}(l)$) excitations along the implant:

$$\boldsymbol{E_s(p)} = \boldsymbol{K(p)} \int_0^L E_{tan}(l)\, S(l) dl \tag{2.12}$$

where $S(l)$ is the complex-valued transfer function that describes how tangential E-fields along the implant wire contribute to the total field at the tip. It needs to be integrated over the length of the lead (L) with tangential E-field excitations at each implant location. $\boldsymbol{K(p)}$ is a dimensionless function to describe the scattered E-field distribution at the tissue near the electrode.

To calculate the transfer function, first, the background E-fields are computed without the implant. Then, the implant can be placed into the tissue to compute the transfer function of the implant. The first part can be done using electromagnetic simulations, including various tissue types. The second part can be done either by using simulations or experiments by applying piece-wise E-field excitations and measuring the resulting RF-induced current on the tip.[94,95] The excitation and measurement can be exchanged by using the reciprocal approach, i.e., the tip can be excited and induced current distribution along the wire can be measured.[96]

The practical value of the transfer function is the separation of the implant model from the RF coil, thus allowing fast estimations for the scattered E-field predictions for different RF excitation conditions. ISO/TS 10974 *Tier 3* requires transfer function-based simulations, which is presently the preferred method by implant manufacturers compared to full model computational simulations.[97]

The transfer function approach assumes that the implant is one-dimensional, and only characterizes the tip of the implant, where maximum RF heating is expected. In general, the incident E-field is distributed along the implant and each location of the implant contributes to the E-field distribution; thus, RF heating of the implant.

The Transfer Matrix approach, which contains the Transfer Function, represents RF-induced currents on the implant along the wire at any two locations along the implant:[98]

$$I(l_i) = \boldsymbol{T_M}(l_i, l_j)\boldsymbol{E}(l_j) \quad (2.13)$$

Where $\boldsymbol{T_M}$ is the two-dimensional complex-valued Transfer Matrix enumerating the incident E-field to the RF-induced currents between two locations l_i and l_j on the implant wire. If $i = 0$ and $j = L$, then, the Transfer Matrix represents the Transfer Function.[98–100]

Modified transmission line method

An AIMD surrounded by a tissue medium with dielectric properties can also be modelled as a coaxial line. The Modified transmission line method (MoTLiM)[101] uses this analogy to adopt the lumped element transmission line theory for an implant, which is derived from the analysis of dipole antennas inside seawater.[102] By using MoTLiM, the implant can be represented with lumped electrical elements, which can be useful solving for implant currents by using electrical definitions such as impedances and voltage sources (Figure 2.6A). Especially, for the AIMDs having a pulse generator case, affecting the amount of coupled E-field, the method can be used to extract AIMD components' electrical properties such as case, lead, and electrode.[103]

In MoTLiM, the tangential component of the incident E-field can be inserted into the telegrapher's equations to solve the current on the lead as follows:

$$I(l) + \frac{1}{k_t^2}\frac{d^2\, I(l)}{dl^2} = \frac{E_{tan}(l)}{Z} \quad (2.14)$$

Where k_t and Z are defined as the effective wavenumber and characteristic impedance of the transmission line, respectively. They are defined as follows[101]:

$$Z = k\frac{\eta H_0^{(2)}(kb) - \eta_d k_d b \mathcal{H}_1^{(2)}(kb)\, ln(a/b)}{4} \tag{2.15}$$

$$k_t = k\sqrt{\frac{k_d^2\left(\mathcal{H}_0^{(2)}(kb) - kb\, ln\,(a/b)\,\mathcal{H}_1^{(2)}(kb)\right)}{k_d^2\mathcal{H}_0^{(2)}(kb) - k^3 b\, ln\,(a/b)\,\mathcal{H}_1^{(2)}(kb)}} \tag{2.16}$$

Where, k_d is the wavenumber inside implant's wire insulation for a conductor radius of *a*, and the total radius together with the insulation is *b*. The Hankel function of the second kind to solve the differential equation for a propagating wave in a cylindrical structure is denoted with $\mathcal{H}_i^{(2)}$, i represents the order of the function, and η_d is the intrinsic impedance of the wave in the wire insulation. The voltage at the position l, $V(l)$ between the lead and the ground at infinity can be defined as:

$$V(l) = \frac{Z}{k_t^2}\frac{d\, I(l)}{dl} \tag{2.17}$$

Then, the induced current on the implant can be calculated using Equation (2.17) by imposing the following boundary conditions around the AIMD components:

$$V_c - Z_c I(-L/2) - V(-L/2) = 0 \tag{2.18}$$

$$V(L/2) - Z_e I(L/2) - V_e = 0 \tag{2.19}$$

Where V_c and Z_c are the voltage and impedance of the AIMD case, respectively. The electrode voltage and impedance are defined as V_e and Z_e, respectively. The parameters of the MoTLiM can be simulated and validated experimentally for an AIMD.[103] Then, the real part of the electrode impedance can be used to solve the power dissipation for further RF safety computations. It is worth noting that the electrical properties of the implant case may significantly change the resonance length of the implant, which has been demonstrated by experiments and MoTLiM simulations (Figure 2.6B).[38,103]

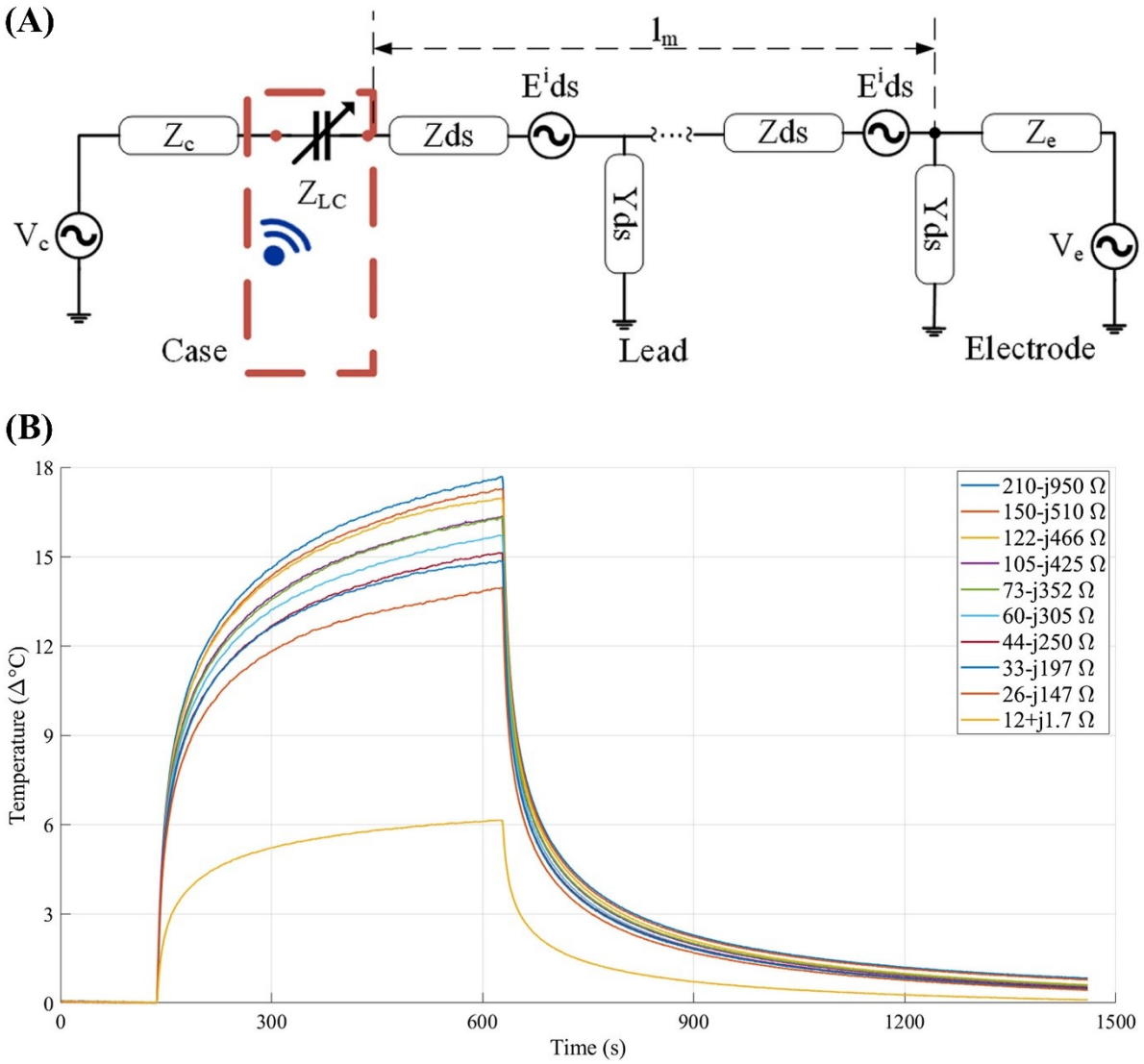

Figure 2.6 Implant modeling using the modified transmission line method (MoTLiM)[101] A) The MoTLiM representation of an AIMD is shown. The case and electrode are represented with the Thevenin equivalent by using voltage sources and impedances. The infinitesimal tangential incident E-fields on the implant lead per unit length, l, are represented as voltage sources with corresponding impedances and conductance. A variable implant lead-case impedance (capacitive) as shown in the red dashed line can alter the scattered E-field at the electrode. B) The effect of the change in lead-case impedance, Z_{LC}, for ten different values to the implant tip temperature rise was experimentally demonstrated. (Reproduced from the reference [38] with the permission from © John Wiley and Sons Inc, 2020).

Although the abovementioned implant safety assessments are broadly practiced and significant to grasp the strategies for the mitigation of RF-induced heating introduced in the next section, it is also crucial to realize that patient-specific tissue properties alter the amount of RF-induced currents on the implants, which could not be precisely predicted for all scenarios by using the abovementioned

methods. Thus, considerable safety margins are currently being applied limiting MRI of patients with implants.

2.3. The strategies to mitigate RF-indued heating

There are two main parameters to reduce implant heating: 1) by modifying the physical properties of the implant such as changing its electrical properties (see section 2.2.2.) and 2) by modifying the transmitted E-field around the implant, such that the E-field at the tip of the implant is substantially reduced. The first method requires advanced RF engineering methodologies to reduce RF coupling to the implant for a broad range of parameters (e.g., different RF frequencies, different implant orientations). In addition, the implant's main functions should not be impaired. The latter can be achieved by a) modifying the MR imaging techniques to reduce average RF power (RF pulse shape, repetition time (TR), flip angle (FA)) which may degrade image quality[104,105] or b) altering the transmission hardware of the MRI system e.g., RF coils. which reduces scattered E-fields at the implant tip without compromising the imaging.

2.3.1. Implant modifications

Engineering the implant's structure to mitigate RF-induced heating can be achieved, for example, by altering the lead conductor with a non-conductive one. A study demonstrated fiber-optic cardiac pacing leads that transform an optic pulse into an electrical stimulus at the lead tip; therefore, the effective electrical lead length is reduced, such as the RF-induced tip-heating.[40] This solution was never a commercial success, probably because fiber-optic probes are too fragile for chronic implantations.

As introduced above, the implant lead can be modeled as a transmission line; therefore, a solution to attenuate the RF-induced currents on the wire can be found by tuning their capacitance, inductance, admittance, and resistance to improve its safety index. For example, an RF-switch circuitry employing PIN diodes can be used to modify the impedance value of an interventional wire, which can be considered as a "switching off" state reducing the RF-induced heating.[106–108] Similarly, a switchable capacitive network was used to change the termination

impedance between implant case and lead and reduce RF-induced heating by 70% at 1.5T (Figure 2.6).[38] Furthermore, transformers can be utilized in the conductor wire to create opposing RF currents cancelling each other, which was demonstrated to produce a more than a 10-fold reduction in the temperature rise.[109,110] RF chokes to block specific MRI frequencies on the catheters demonstrated a substantial reduction in RF-induced heating.[31] Designing resistive passive leads by using a so called "billabong" structures showed also RF-induced heating reductions at 1.5T and 3T.[34]

It should be noted that RF frequency dependence of the electronic components of the implant, together with surrounding patient-specific tissue properties may have uncertainties that cannot be reduced by only implant modifications. Furthermore, other restrictions (size, cost, complexity, patient safety) may prevent designs to be implemented in implants.

Therefore, investigations on steering the background RF field produced by the RF coil are appealing leading to more generalizable solutions to implant safety.

2.3.2. Parallel transmission techniques to modify RF fields

In conventional birdcage-type single-channel body coils, the amplitude of the E-field can be reduced to mitigate RF-induced heating on the implants. In fact, this is the primary RF safety practice for scanning patients with implants.[26–28] However, the transmit power reduction simply sacrifices MR imaging quality as well, which is not desirable in clinical practice.

Parallel transmission systems can shape RF excitation profiles in the target region by adjusting the amplitude and phase of the independent RF transmit channels.[45–48] Therefore, as it has been shown by Equations (2.12) or (2.14), the driving incident E-fields can be shaped around the implant, where their tangential E-field components may add up to insignificant scattered E-field values at the implant tip minimizing the RF-induced heating.

The local E-fields in tissue from each pTx channel can be calculated by reformulating Equation (2.5) as follows:

$$SAR = \frac{1}{V}\int_V \frac{\sigma}{2\rho}\left|\sum_{n=1}^{N} \boldsymbol{E_n}\right|^2 dV \tag{2.20}$$

where N is the number of pTx channels and $\boldsymbol{E_n}$ denotes E-field from the pTx channel n. The general solution for the prediction of local SAR hotspots (see Figure 2.2) in different tissue segments may demand extensive electromagnetic computational power. Computations for each pTx excitation setting are therefore unfeasible by running full-wave electromagnetic simulations and simplifications are applied.

The linearity of Maxwell's equations can be employed to superimpose the N individual E-field vectors from N pTx channels at each location within a human body model. Similarly, each E-field vector $\boldsymbol{E_n}$, formed by the n^{th} pTx channel, is proportional to a complex excitation current, which is represented in the phasor form I. The amplitudes of the pTx channels can be normalized to create the same RF field at a selected location (i.e., isocenter of an unloaded RF coil). Then, the generated normalized E-field vector from the pTx channel can be represented by $\tilde{E}_n$, which can be used to represent the total E-field using the phasor notation as:

$$\boldsymbol{E} = \sum_{n=1}^{N} \boldsymbol{E_n} = \widetilde{\boldsymbol{E}} \cdot \boldsymbol{I} \tag{2.21}$$

Please note that $\widetilde{\boldsymbol{E}}$ is superimposed to $N \times 3$ matrix, which is the E-field vector composed of x, y, and z components introduced by individual pTx channels. Using Equation (2.20), the averaged SAR in a sample tissue can be reformulated in terms of the normalized E-fields and phasor form of the RF excitation currents from the pTx elements in quadratic form:

$$SAR = \frac{1}{V}\int_V \frac{\sigma}{2\rho}\left|\widetilde{\boldsymbol{E}}\cdot\boldsymbol{I}\right|^2 dV \tag{2.22}$$

$$= \boldsymbol{I}^H \cdot \frac{1}{V}\int_V \frac{\sigma}{2\rho}\cdot\widetilde{\boldsymbol{E}}^{\boldsymbol{H}}\cdot\widetilde{\boldsymbol{E}}\cdot\boldsymbol{dV}\cdot\boldsymbol{I}$$

$$= \boldsymbol{I}^H \cdot \boldsymbol{Q}\cdot\boldsymbol{I}$$

where the superscript $\boldsymbol{H}$ denotes Hermitian transpose. The dependencies of the tissue properties and normalized E-fields are compacted in the individual local $\boldsymbol{Q}$ matrices (will be mentioned as $\boldsymbol{Q}$ or Q-Matrix later in the text) averaged over the volume of the local tissue. The Q-matrix is a positive definitive matrix because the volume cannot be zero and SAR is an averaged non-negative value. The dimensionality of the Q-matrix depends on the number of pTx channels, which is $N \times N$. The application of the Q-matrices was first introduced for phased-array hyperthermia systems and later for pTx MRI.[44,46,111]

The incident E-field determines both the background E-field distribution in tissue and the induced current on the implant. Adjusting multiple, independent RF transmit channels can therefore be used to cancel implant lead currents and accordingly implant tip heating.

Parallel transmission, furthermore, has the degrees of freedom to improve the B_1-field homogeneity and amplitude for imaging purposes. Therefore, the imaging inhomogeneity and implant E-field minimization should be adjusted together for the pTx mitigations. A cost function can be constructed to find optimal RF excitation settings for pTx systems, e.g. by using a Nelder-Mead Simplex algorithm[112],: Then, the B_1^+ component of the region of interest (ROI) to minimize MR image inhomogeneity can be inserted into the cost function as follows[52]:

$$min\left(|E|_{implant} + \Lambda\left(\frac{max_{ROI}(|B_1^+|) - |B_1^+|}{max_{ROI}(|B_1^+|)}\right)\right) \tag{2.23}$$

With the B_1^+ component of the region of interest for MR imaging and $|E|_{implant}$ the RF-induced E-field around the implant tip. ROI denotes the region of interest for the imaging and Λ as a weighting factor between imaging quality and E-field at

the implant tip. The optimization parameters can be extended to multiple E-field minimization locations around the implant or for more than one implant being present in the body.[53,54] Example simulation study results are shown in Figure 2.7, where both 4 and 8-channel pTx systems are simulated among nine different patient models with a DBS implant.[54] *1g* local SAR around the implant could be reduced to 3 W kg^{-1} for the worst-solution compared to 24.5 W kg^{-1} for a single-channel birdcage coil RF excitation.[54]

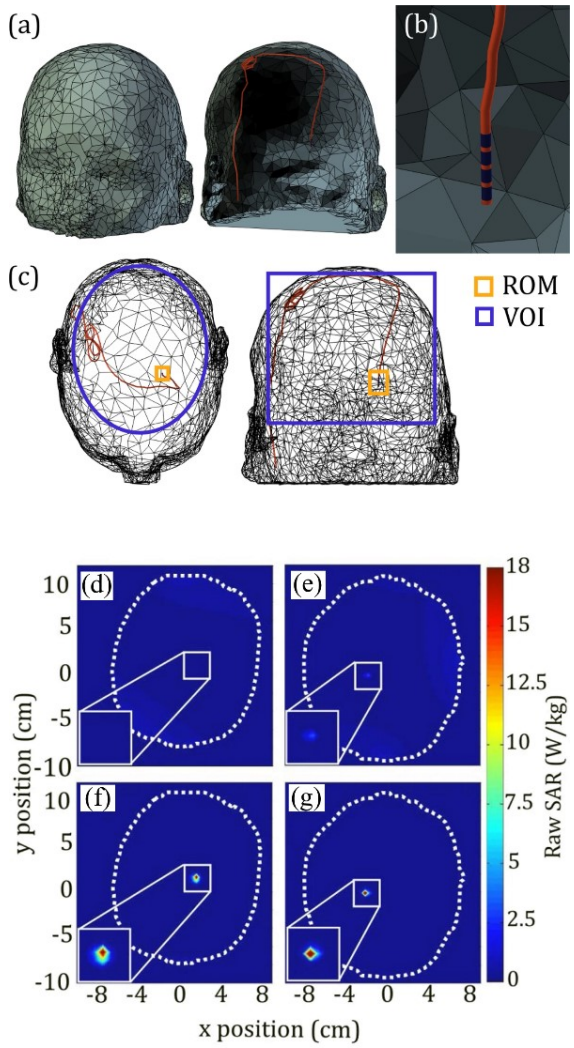

Figure 2.7 An example of E-field pTx optimization around a DBS implant using simulations. A) The head mesh model and DBS lead trajectory (in red) are shown. B) A zoomed view of the implant tip with electrodes. The circular electrodes are shown in dark blue color. C) The yellow solid line depicts the E-field minimization region and the blue line the region to minimize B_1^+ inhomogeneity. D) optimized solution for 1g SAR using an 8-channel pTx system. (E) *1g* SAR optimization in another patient model using 4-channel pTx transmission. (F) and (G) are the SAR resulted from single-channel birdcage coil excitations. (Reproduced with permission from the Reference [54] CC BY 4.0, 2019).

Nevertheless, there is a significant challenge to translate these results to safe RF excitation scenarios in clinical practice. Variability in absorbed power around a DBS electrode for five investigated body models, varied by 88% by only changing tissue properties without any implant-related parameters.[58] Adding patient movement[70,71], differences in implant position and orientation[69,113,114], tissue

properties[58] or other hardware imperfections can increase the uncertainties of applying simulation based methods for pTx based optimizations of implant safety.

Measurements to determine RF safety and imaging related parameters for implant safety to minimize Equation (2.23) would have several advantages. Directly measuring the implant RF safety related parameters such as induced current, E-field and temperature around the implant tip would have lower uncertainties than simulation based estimations.[69,113,114] If measurements could be performed on-the-fly patient movement-induced SAR changes could be assessed.[70,71] Hence, implant safety rooted in measurement-based methods would greatly improve the feasibility and accuracy of the pTx-based mitigation of RF-induced heating. In general, there are two approaches that can be utilized to determine the required RF-induced E-fields, implant currents and/or temperature hotspots: 1) MR-based and 2) sensor-based measurement techniques.

2.3.3. MR-based mitigation of RF-induced heating using pTx

As time-varying RF-induced current flows on the conductor, magnetic fields are formed around them. This relationship can be expressed by simplifying Ampère's circuital law approximating for an infinitely long conductor[80] to relate the tangential magnetic field phasor around the implant wire. However, the total magnetic field cannot be directly measured by using MR because the B_1^- component of the transmit field is not apparent due to the process of spin excitation. Still, it can be approximated using MR images.[115–119] The total tissue magnetization will contain the B_1^+ component of the magnetic field from the coil and the B_1^+ component created by the wire. The B_1^+ depends on how much signal is acquired (i.e., type of B_1^+ mapping sequence). For example, a GRE sequence can be utilized to determine absolute B_1^+ from the signal intensity ($\boldsymbol{SI}$)[115]:

$$\boldsymbol{SI} = \boldsymbol{\mathcal{C}} \frac{sin(\boldsymbol{S_T}\alpha_{nom})(1 - e^{-TR/T_1})}{1 - e^{-TR/T_1}\, cos(\boldsymbol{S_T}\alpha_{nom})} \tag{2.24}$$

where, $\boldsymbol{\mathcal{C}}$ represents local spin density, receiver coil sensitivity and T_2 effects, $\boldsymbol{S_T}$ is the dimensionless transmit sensitivity of the transmitter coil, α_{nom} is the nominal flip angle. The parameter $\boldsymbol{S_T}$ depends on the artifact caused by the implant and

can be found by applying different α_{nom} and fitting into the equations $\alpha_{nom} = \gamma B_{1,nom}^{+} \tau$ for a short RF pulse of length τ, and $B_{1,image}^{+} = S_T B_{1,nom}^{+}$.[115]

For different pTx RF excitation modes, different imaging artifacts will be visible in the images which correlate with RF induced currents on the implant. These images can be used as a relative gauge to understand which pTx mode induces stronger current on the implant. Hence, it can be a brief validation method for the sensor measurements proposed in the thesis.

In recent studies, it is also demonstrated that MR images can be utilized for the adjustment of pTx settings in the context of implant safety to minimize the total RF-induced currents by weighting individual RF-induced currents using various pTx images.[51,57,61,120,121]It should be noted that these MR-based methods utilizing $B_{1,image}^{+}$ require B_1^{+}-mapping methods to estimate the currents or MR-images to determine pTx mitigation settings, which require a certain amount of time to acquire. In one study, B_1^{+}-maps were acquired using GRE images which took 82 s.[115] Another study to estimate signal intensity around the implant spent 55 s for MR image acquisition[117] For the two-channel pTx study, 3 GRE MR images were acquired within 21 s to calculate “implant friendly” modes[57], where GRAPPA was used to accelerate image acquisition.[122] The acquisition time may challenge the feasibility of MR-based method while increasing the number of pTx channels; for example, four minutes were required for the B_1^{+} for four channel pTx mitigation.[61] Therefore, the uncertainty of the estimated implant currents could be affected from the patient motion, especially in UHF imaging regime.[70,71]

Another issue of the MR-based methods about image artifacts. Implants inherently present B_0 image artifacts due to their metallic components. For an in vivo scenario, the uncertainties may increase while locating the image B_1^{+} artifact together the with B_0 artifact around the complex tissue structures. In addition, signal voids may exist in UHF images, which would also increase the uncertainties of the methods. There is demand, therefore, for faster and more robust solutions.

2.3.4. Sensor-based mitigation of RF-induced heating using pTx

In contrast to MR-based methods, another way to rapidly assess and mitigate RF-induced heating is by utilizing sensors that are either externally positioned near the implant without being directly attached to it or embedded in the implant. For example, a custom E-field probe using optical light emitting diodes and a fiber-optic temperature probe externally attached to the implant tip demonstrated the RF-induced E-field and temperature distributions for two different 1.5T scanners as shown in Figure 2.8.[123] Please note that temperature rise and E-field profiles measured by the sensors demonstrate similarity; however, they are significantly different in absolute terms even though the scanners operate at the same RF frequency.

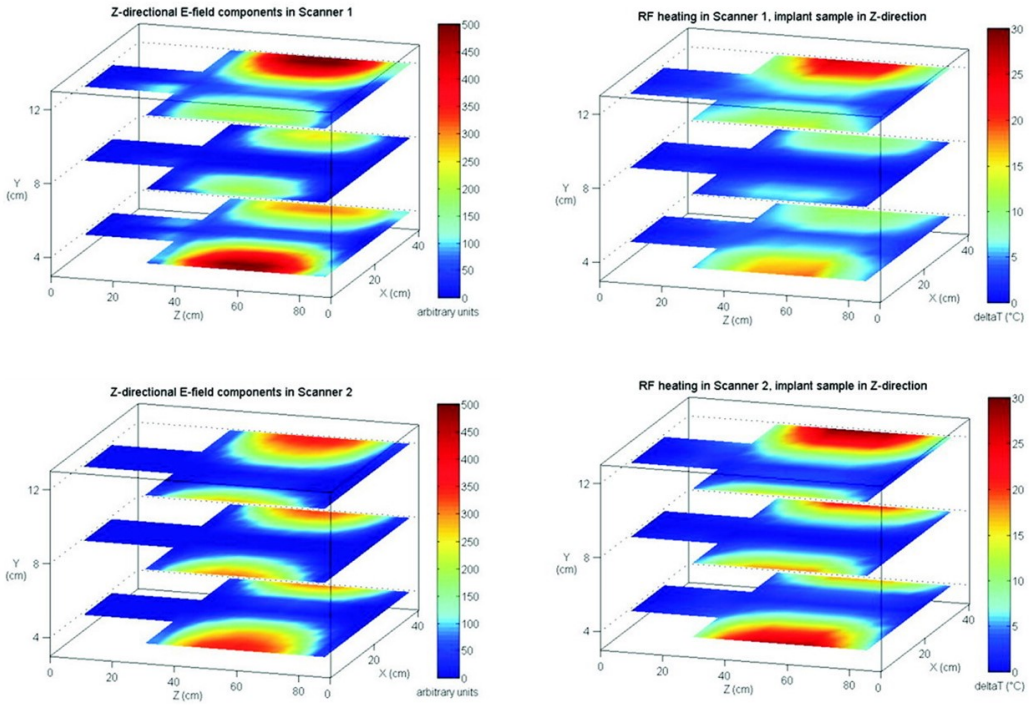

Figure 2.8 RF-induced E-field and temperature measurements at two 1.5T MR scanners for an implant with external sensors. The sensors can successfully measure the spatially varying RF-induced E-field and temperature rises at the implant tip. (Reproduced with permission from the Reference [123] © John Wiley & Sons, 2008).

A toroidal transformer as an external current sensor was also proposed to detect the RF-induced currents on conductive wires as shown in Figure 2.9.[124] The magnetic flux, Φ, coupled to the toroid due to the RF-induced current in the implant wire can be written using Faraday Law:

$$\Phi = \int_a^b \frac{\mu_0}{2\pi r} gIdr \tag{2.25}$$

where the integral boundary is defined by the radii, a and b representing the inner and outer radius of the toroid, respectively. The length of the toroid cavity is g. In that study, the outer diameter of the wire was about 7 mm and the lengths were about 20-60 mm, which were affecting the gain of the current sensor.[124] Therefore, it is critical to note that it may not be feasible to attach the sensors to a few mm thick implant wires. In addition, the readout electronics cannot reside in the body as implants are fully immersed.

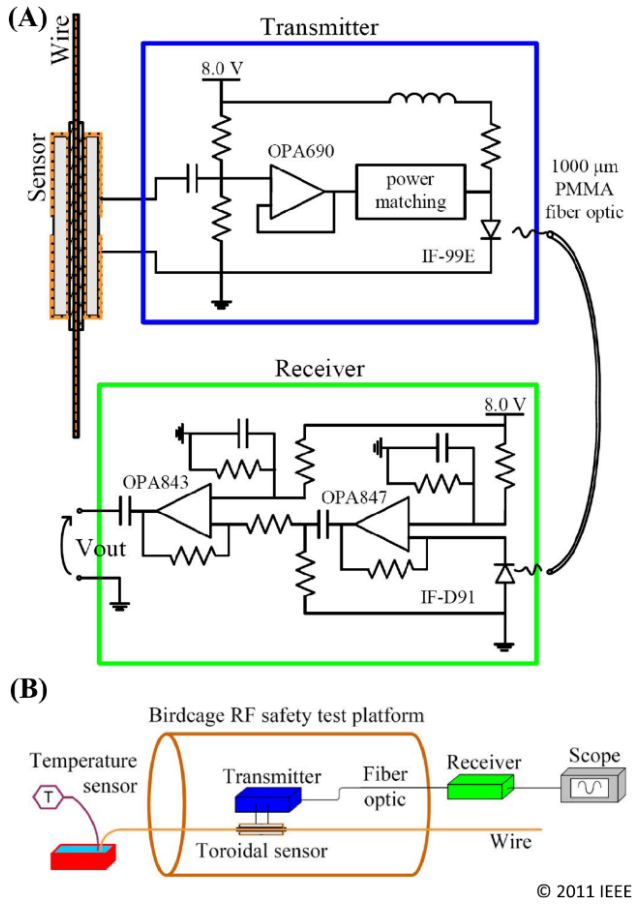

Figure 2.9 An example of an external toroidal sensor to detect RF-induced currents on the conductor. (A) Simplified schematic of a current sensor to measure RF-induced currents on the wire by using a toroidal transformer surrounding the wire structure. The measured currents are transmitted via a fiber optic cable using light emitting diodes. (B) An experimental setup using the current sensor is shown. The sensor is placed around the wire, which is several cm away from the wire tip. (Reproduced with permission from the Reference [124]).

Embedded sensors were also presented to assess the RF safety of implants.[114,120] For RF-induced current measurements, a light emitting diode was embedded a few millimeters from the tip of a pacemaker wire, with a rectifier circuit to measure the root-mean-square (RMS) value of the RF-induced currents at the tip.[114] The quadratic relationship between RMS current values successfully correlated with the temperature rise, measured by an external fiber-optic temperature probes.[114] Although an external fiber-optic cable may not be suitable to be placed in realistic implants, it has been shown that small RMS sensors might be feasible for RF-safety assessments. Silemek et al. demonstrated an embedded thermistor at the implant tip for the RF-safety assessments.[120] The temperature rise at the tip of the implant could be read out during an MRI scan by using a Bluetooth Low Energy (BLE) wireless communication protocol. Although the speed of the temperature acquisitions was 1 Hz, it was demonstrated that an RMS sensor embedded in an implant could transmit the required temperature information even if fully embedded in the body.

RMS sensors, so-far, cannot be used for the pTx mitigation as the complex valued E-field or current values need to be adjusted to suppress E-field on the tip of the implant (see Equation (2.20)), where RMS sensors have only the amplitude information. In the thesis, it will be demonstrated that RMS sensors can be utilized for pTx mitigation of the RF-induced currents. Initially, investigations into current minimization techniques on the implants were initially performed, however, based on measuring the complex valued RF induced currents, before simplifying the sensor architecture to RMS signal acquisitions.

Null modes for pTx mitigation

Previously, it is demonstrated a toroidal current sensor can be utilized to probe a phase sensitive response of all pTx channels to null the current on the guidewire structure.[61] The null modes (NM) method models pTx and RF-induced currents as an $N + M$ multiport network where an N channel pTx coil transmits and M sensors observe RF-induced currents at their placed location. Then, a complex-valued coupling coefficient ζ_{mn} can be constructed by a transmission from the n^{th} channel of the pTx system and a measurement of the RF-induced current using

the m^{th} sensor on the wire. This coefficient includes all transmit chain related gains and losses such as RF amplifier gain, coil losses, implant geometry, and size. Therefore, at the m^{th} sensor location, the RF-induced currents for any set of a complex linear combination of k different transmit vectors of N channel pTx inputs can be formulized to:

$$\boldsymbol{I} = \zeta \boldsymbol{\mathcal{W}}, \tag{2.26}$$

where ζ includes all coefficients in $M \times N$ dimensional matrix form. $\boldsymbol{\mathcal{W}}$ includes complex transmit weights in $N \times K$ dimensional matrix and finally, $\boldsymbol{I}$ is the $M \times K$ dimensional RF-induced currents on the conductor, where each element corresponds to RF-induced current at the sensor location m formed by k RF transmit weight.[61]

Finding a solution to $\boldsymbol{\mathcal{W}}$ that lies in the null space of ζ will result in minimum RF-induced current at the m^{th} sensor measurement location. In addition, any linear combinations of the null space also induce minimum currents on the conductor. One needs to obtain the coupling matrix $\boldsymbol{\zeta}$ to solve the network. Then, the transmit weights $\boldsymbol{\mathcal{W}}$ provide the minimum induced currents that can be computed either by the eigenvalue or singular value decomposition (SVD) of the sensor network. Eigenvalue decomposition can only be applied to diagnosable matrices. Therefore, it is applicable when only a single sensor is used such that $M = N$. For a more general solution, SVD of $M \times N$ dimensional $\boldsymbol{\zeta}$ can be factorized as,

$$\zeta = \boldsymbol{U}\boldsymbol{\Sigma}\boldsymbol{V}^{*}, \tag{2.27}$$

where $\boldsymbol{U}$ is a complex-valued unitary matrix ($M \times M$), $\boldsymbol{\Sigma}$ contains the singular values with a dimension of $M \times N$ and $\boldsymbol{V}$ is the complex unitary matrix with a dimension of $N \times N$. The columns of $\boldsymbol{V}$ orthogonal to $\boldsymbol{U}$ that corresponds to zero singular values give the minimum induced currents, and the columns of $\boldsymbol{V}$ with maximum singular values give the maximum induced currents and maximum coupling mode.[61] Depending on the experimental configuration, SVD can be utilized to compute NMs. The number of NMs increases with the channel count. Therefore, the degree of freedom for a pTx mitigation increases. In contrast, when

the sensor (observer) count M increases, the degree of freedom for the pTx mitigation shrinks. Imposing current null at multiple locations on the wire increases the effectiveness of the NMs. It should be emphasized that the NM method does not provide any information about the imaging metrics of the MR scanner. Therefore, linear combinations of NMs must be harmonized with B_1^+-maps to preserve imaging quality. In addition, the problem of embedding bulky current sensors on the implants has not been successful to date mostly because of their size and complexity of the readout electronics.

3. Parallel transmission implant safety testbed

In this chapter, the development, construction, and demonstration of the required hardware for extensive testing of the proposed pTx mitigation methods is presented. The work presented in this chapter is published in *Magnetic Resonance in Medicine* [63]. In addition, the resources for hardware, firmware and software are published here: www.opensourceimaging.org/ptx-implant-safety-testbed/.

3.1. Introduction

Benefits of multi-channel RF-transmission, pTx, have been experimentally demonstrated more than two decades ago.[45–48] However, the requirements of synchronized independent control of RF-transmission parameters such as amplitude and phase, as well as dedicated multi-channel RF-coil hardware, next to an increased complexity in RF safety assessment prevented for long the application of pTx in today's clinical MRI systems. Most clinical MRI systems use field strengths up to 3T, where single-channel body coils like a circularly polarized birdcage are sufficient to generate homogeneous B_1^+ fields required for clinical applications. However, as the field strength increases beyond 3T, the RF wavelength in tissue (for 3T ≅ 27 cm , 7T ≅ 13 cm) is shorter than the average imaging region (head, body and etc.), which penalizes the B_1^+ field homogeneity.[125] At these high frequencies, pTx systems have been introduced as the most promising approach to homogenize the B_1^+ and improve imaging quality. Other applications independent of the transmission frequency, such as the RF safety of implants, show promising results and should be investigated further.[2] This requires accessible and low-cost pTx hardware that can be broadly tested.

The historically first approaches at pTx systems can simply be considered as manual tuning of (e.g., mechanically adjusting cable lengths) of amplitudes and phases to shim subject-specific B_1 field inhomogeneities in UHF.[126,127] This tedious mechanical B_1-shimming method was improved by introducing digitally adjustable phase-shifters and attenuators.[128] Moreover, modular implementation of the RF components and dynamic signal modulation (RF excitation pulse

adjustment during MRI sequence) enabled higher pTx channel count and flexibility to modulate B_1 fields.[129,130]

Although these systems aid investigation of pTx applications, they are restricted to a particular MR system hardware. They receive the required base RF signal from the system to synchronize other components, which limits the application frequency range, in particular broader implant safety testing. In addition, the RF duty cycle of an MRI is usually less than 10%. High peak RF powers are desired to generate short RF pulses with sufficient B_1 to obtain the desired FA. In contrast, as shown in Equation (2.5), time averaged power is critical for RF safety. Therefore, the cost of building high peak power RF amplifier can be avoided by decreasing the peak power constraint and increasing its duty cycle, which would supply the same amount of average RF power while increasing the bandwidth and reducing the cost. Furthermore, RF safety assessment inside an MRI scanner with space limitations for the measurement equipment or measurements in high static B_0 fields leading to additional safety precautions are some limiting factors of existing systems. Scan time is scarce and expensive limiting to accessibility for extensive testing. In addition, since implant safety assessments may benefit from flexible sensor implementations to measure E-field, H-field or temperature, automated and reproducible positioning for various excitation scenarios are needed.

To address these problems, a pTx capable implant safety testbed was designed and constructed. It furnishes versatile features for RF safety testing. The constructed testbed can be adjusted for RF-heating experiments at various field strengths from $B_0 = 0.5$-7T and is scalable to 32-channel RF transmission. Furthermore, a 3D positioning robot with a submillimeter positioning sensitivity indulges electromagnetic field and temperature mapping experiments. The constructed pTx implant safety testbed can be utilized standalone or within an MRI system.

3.2. Methods

3.2.1. RF transmit and receive chain

A photograph of the constructed pTx implant safety testbed is shown in Figure 3.1. Based on the previous work at PTB,[131,132] a scalable and broadband fully digital pTx signal generation system was configured to cover a broad range of clinically employed MR frequencies between 0.5T (f_0 =21 MHz) to 7T (f_0 = 297 MHz). Therefore, a broadband 8-channel RF transmitter by using 2 × 4-channel arbitrary waveform generator cards were used as the signal generator (M4i.6622-x8, Spectrum Instrumentation GmbH, Grosshansdorf, Germany), which can be scaled to 8 × 4-channel configuration for 32-channel operation. The maximum sampling rate (f_s) of the cards is 625 MS s^{-1}. This favors RF-transmit frequencies up to f_0 =128 MHz (B_0 = 3T). At B_0 = 7T frequency 297 MHz, the sampling frequency is close to the Nyquist limit. Therefore, spurious signals at 328 MHz would be produced in the spectrum, which might be challenging to suppress using off-the-shelf filters. Therefore, for 7T experiments f_s = 400 MHz was employed, where a sideband signal of 103 MHz occurs during the 297 MHz signal generation with a 6 dB signal attenuation. The spurious signal at 103 MHz was suppressed by using a high-pass filter: insertion loss < 1.5 dB, passband 290-3000 MHz (SHP-300+, Mini-Circuits, New York, USA). The attenuation is not significant as the signal will be amplified in the next stage.

The generated pTx signals are then fed into eight modular, broadband (20 MHz – 1 GHz) RF power amplifiers (ZHL-20W-13SWX+, Mini-Circuits, New York, US). The gain of the RF amplifiers is 50 dB and the maximum output of the amplifiers was adjusted to 20 W per pTx channel, which can deliver 100% duty cycle. For the transmission, the amplifiers can be signaled to unblank with a transistor-transistor logic signal.

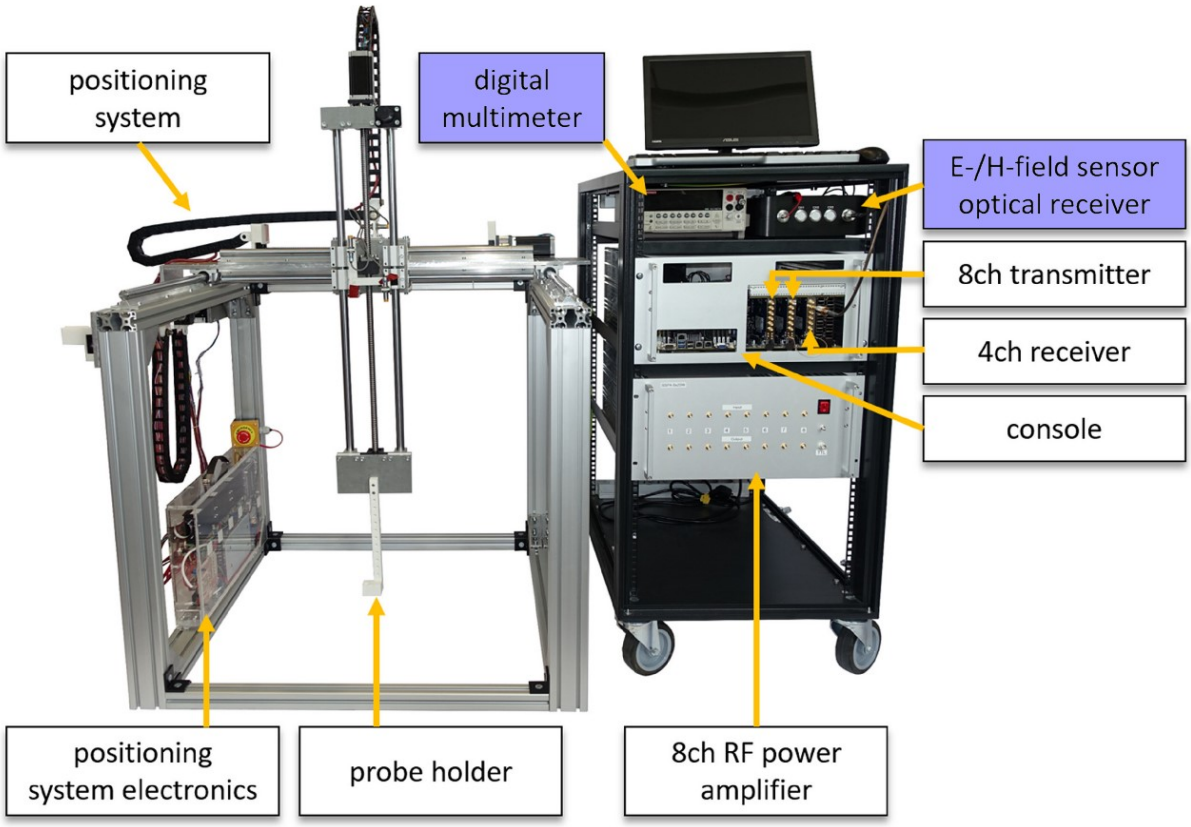

Figure 3.1 A photograph of the pTx implant safety testbed hardware. On the left, a submillimeter positioning system. On the right, the assembled pTx electronics within a 19" rack. The annotated photo indicates different system components for the implant safety measurements, including 8-channel pTx arbitrary waveform generator, broadband RF power amplifiers and 4-channel receiver. Please note that the free space was left intentionally for an additional 8-channel pTx amplifiers. (Adapted from Reference [63] CC BY 4.0, 2020).

For the receiver, a 4-channel 14-bit ADC card (M4i.4451-x8, Spectrum Instrumentation GmbH, Grosshansdorf, Germany) was utilized to measure sensor signals. The sampling rate of the receiver can go up to 500 MS s^{-1}. This allows a direct sampling up to $B_0 = 3$T frequencies ($f_0 = 128$ MHz). For $B_0 = 7$T frequency ($f_0 = 297$ MHz), the sampling rate is not enough. Therefore, another high-pass filter (SHP-300+, Mini-Circuits, New York, USA) as an anti-aliasing filter was used. Then, the received signals are decimated and filtered in the digital domain. Finally, the relative phases were computed using a selected channel.

The transmission and reception cards are connected to a Peripheral Component Interconnect Express x8 Gen2 interface which is hosted by a motherboard (X10DRX, Supermicro Computer Inc, San Jose, CA, US). Although this thesis used 8-channel pTx system, the motherboard has more (total = 8 × 10) PCI-Express

slots hosted by two central processing units. This supports additional freedom to provide 32 transmit channels + 8 receive channels. All transmit and receive modules can be synchronized by internal and external triggers. The whole RF transceiver system was placed into a modular rack (Width = 550 × Depth = 80 × Height = 1100 mm^3) for an easy transportation.

The transmit and receive console runs under a Linux-based operating system (OpenSUSE 13.2, Kernel: 3.16.6-2). The cards are programmed using C, and Fortran subroutines. A graphical user interface (GUI) was written in Python to control and parametrize the settings of the cards. All software is published open-source.[133]

An 8-channel pTx 7T head RF-coil with an embedded cylindrical RF shield is used in the transmit/receive chain.[134] The coil has eight 160 mm long rectangular loops in an elliptical arrangement where the left to right and the anterior to posterior distances are 215 mm and 250 mm, respectively. The 7T head coil also represents a, scaled, 3T body coil, allowing easier RF safety measurements in a much smaller volume.

3.2.2. Positioning system

The pTx implant safety testbed includes the open-source positioning system, COSI Measure, favoring placement of the implant or field probes in 3 dimensions.[135] The system has a GUI that provides submillimeter positioning of the object via manual commands. A previously existing system interface was extended, in this work, to allow the connectivity of the pTx implant safety testbed for automated measurements. For this purpose, the ethernet interface of positioning electronics was connected to the auxiliary ethernet port of the system console. Then, the existing source code of the positioning system was modified to allow automated measurements for implant safety. In the implemented interface, the console sends absolute positions to the positioning system, then the positioning system responds to commands when it had arrived at the position. Finally, the implant safety testbed sends the corresponding RF-excitation pulses to the coil and then, the corresponding measurements are taken.

3.2.3. Phantom

For the testbed measurements, a cylindrical phantom was used with an inner diameter of 200 mm made of a poly(methyl methacrylate) tube. The bottom of the phantom container is sealed, and the top is open for a flexible insertion of the implant and field probes using the positioning system. This container was filled with a mixture of polyvinylpyrrolidone (PVP), deionized water and NaCl resulting in relative permittivity of $\varepsilon_r = 36$ and electrical conductivity of $\sigma = 0.27$ S/m at $f = 297$ MHz. The total fill height of the PVP mixture was 188 mm. (A slightly different phantom is used and given in Chapter 5.)

A semi rigid coaxial wire with a length of 177 mm (diameter = 4 mm, 15 mm of the outer insulation is removed) was used as an implant for the experiments.

3.2.4. Auxiliary sensors for implant safety assessments

To characterize the effectiveness of the pTx mitigations, three different sensors were utilized in the pTx implant safety testbed. To measure the radial time-domain E-field around the implant, a fiber-optic E-field sensor (E1TDSxSNI, Speag, Zurich, Switzerland) was connected to the testbed via a fiber-optic converter. The probe utilized a 3 mm dipole at its tip to measure the raw E-field values. The received signals from the converter fed to one ADC channel of the testbed.

Similarly, a one axis H-field sensor (H1TDSx, Speag, Zurich, Switzerland) was connected to the system for time-varying magnetic field measurements. The sensor has a 2 mm loop at its tip and requires on axis rotation by 90° to measure B_x and B_y-field components in order to calculate B_1^+. The measured signals from the H-field probe are optically transferred to the same fiber-optic converter and then fed to a receiver channel of the testbed.

As temperature is the most direct risk indicator for RF safety of the implants, temperature sensors are also utilized in the testbed system. Fiber-optic temperature probes (Luxtron, Lumasense Technologies, Santa Clara, US) were used as external sensors. In addition, temperature was determined by embedding a thermistor at the tip of dummy implants. Thermistors allow for fast, precise, and

high-resolution temperature measurements.[120,136] This is highly advantageous since it allows to work with very low RF power, thus avoiding high increases of the background temperature and correspondingly long cool-down periods between consecutive experiments. The disadvantage is that they require extra electrical wires to measure their resistance and that they create image artefacts if the measurements are going to be repeated in the scanner.

In the testbed experiments, fiber-optic probes, and a negative temperature coefficient thermistor (NTC) (NCP 18XH103F03RB, $R_{25°C} = 10$ kΩ, Murata Manufacturing, Nagaokakyo, Japan) were simultaneously measured for comparison. The thermistor was embedded at the implant. The terminals of the thermistor are connected to the inner conductor and shield of the implant. The end other end of the implant was extended to the testbed console and connected to a multimeter (Keithley 2000, Tektronix, Beaverton, US) to read the resistance of the thermistor. The fiber-optic probes were placed as close as possible to the tip of the wire, as shown in Figure 3.2.

The settings of the digital multimeter to measure the resistance were adjusted to a 10 kΩ reference sampling setting. To increase the sampling speed averaging and liquid crystal display were turned off during the measurements. The device was interfaced with the testbed via an RS232-USB interface. The communication speed of the RS232 interface was adjusted to 19200 Bd. The testbed console sends keywords to the multimeter by sending Standard Commands for Programmable Instruments[137] to retrieve the measured resistance values. Streaming resistance values from the multimeter were converted to the temperature values in the testbed console by using the Steinhart-Hart equation.[138] All other temperature related programming and calculations were done using Python programming language.

3.2.5. System calibrations

Several calibrations were done to characterize the system and to perform pTx mitigations precisely. For the positioning system, the GUI of the positioning system was modified to calibrate axes in the desired position to get the standalone absolute Cartesian coordinates of the probe holders. The repeatability

of the positioning system was assessed together with the E-field probes. For this purpose, the E-field sensor was positioned about 65 mm away from the implant tip in the 8-channel pTx coil and phantom allowing measurements of the E-field component perpendicular to the implant as shown in Figure 3.2A. First, 10-consecutive E-field measurements were performed on the implant without changing the position of the implant. Then, another set of 10 measurements was performed by moving the probes outside of the phantom using the robot and repositioning them again in the same location.

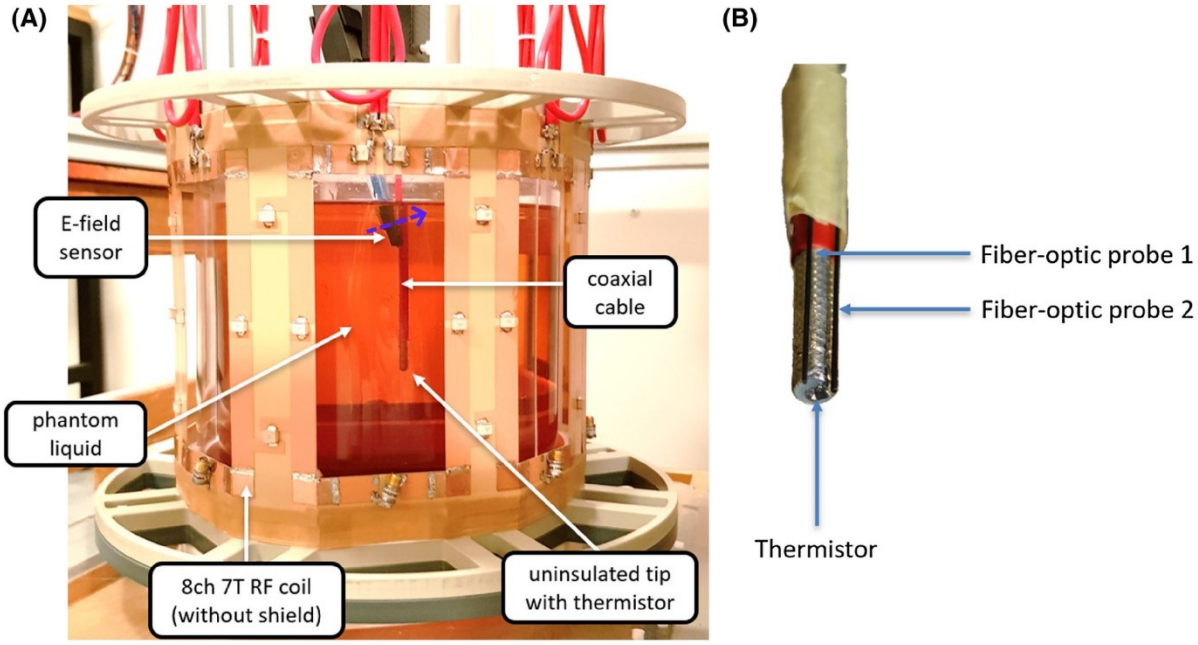

Figure 3.2 Measurement setup using external time-domain E-field sensor for system calibrations and pTx mitigation. A) Photograph of the implant wire in the phantom together with the 8-channel pTx RF coil (7T). The RF shield of the coil was removed for the photograph. The placed E-field sensor measures radial E-fields (sensor axis depicted with a dashed blue arrow) induced on the implant. This information can be used for pTx mitigation. B) A close-up photo of the implant wire with an embedded thermistor. The external fiber-optic temperature probes are taped around the implant allowing tip temperature measurements. 15 mm outer insulation of the coaxial cable was removed around the lead tip in order to mimic an implant electrode geometry (Reproduced from the Reference [63] CC BY 4.0, 2020).

The E-field and H-field probes were calibrated in air using a custom-built transverse electromagnetic (TEM) cell.[139] It should be noted that relative permeability of water ($\mu_r \cong 1$) permits a straightforward calibration of the H-field probe in air ($\mu_r \cong 1$) for B_1-field measurements in the phantom. However, the

relative permittivity of the phantom (i.e., $\varepsilon_r = 36$) is much higher than air ($\varepsilon_r \cong 1$), so a calibration of the E-field probes in phantom is more challenging. Nevertheless, the relative E-field values are critical for the proposed pTx mitigations and have been used throughout the thesis.

The amplitudes and phases of the RF chain were calibrated at 297 MHz to equalize the output amplitudes and phases between channels. In addition, 6 dB attenuators (Mini Circuits, VAT-6+, New York, NY, US) were placed at the inputs of the amplifiers to ensure that output power is not above amplifiers' 1dB compression (~41dBm). Although the maximum output power was reduced to approximately 3 W, the amplifiers are in their linear region without extra linearity corrections.

The system uncertainties in the used components in the implant safety testbed are given in Table 3-1.

Table 3-1 Component uncertainties of the pTx safety testbed. In should be noted that the TEM cell uncertainty contains the overall system with $E-$ and $H-$field probe and transmit chain uncertainties (except RF coil and receiver).

Arbitrary waveform generator (M4i.6622-x8)	
Amplitude output accuracy	±0.5 mV ± %0.1 (low power)
	±1.0 mV ± %0.2 (high power)
DAC differential non-linearity	± 0.5 LSB
DAC internal non-linearity	± 1.0 LSB
Internal clock accuracy	≤ 20 ppm
Receiver (M4i.4451-x8)	
ADC differential nonlinearity	± 0.4 LSB
ADC integral nonlinearity	± 10.0 LSB
ADC word error rate	10^{-12}
Offset error (full speed)	< 0.1% of range
Gain error (full speed)	< 1.0% of reading
Internal clock accuracy	± 20 ppm
Amplifiers (ZHL-20W-13SW+)	
Gain flatness	± 1.8 dB
TEM cell calibration*	
Field uncertainty	5%

3.2.6. RF coil validation measurements

One application of the pTx testbed is electromagnetic field measurements of an RF coil, which can be used to validate numerical simulations and understand the uncertainties generated by the RF chain. First, the 8-channel S-matrix of the RF-coil was measured with a network analyzer (ZNBT 8, Rohde & Schwarz GmbH, Munich, Germany) and included in the simulations (performed by the other authors in the Reference [63]) (Sim4Life v5.0, ZMT Zurich MedTech AG, Zurich, Switzerland) to compensate for RF-coil losses and coupling. Then, a single-axis H-field probe was immersed into the phantom 50 mm below the surface of the phantom liquid. The B-field generated by the coil in the phantom was measured in a 60 × 60 mm^2 area with a 5 mm in-plane resolution twice (the same area was mapped with the H-field probe rotated by 90°). The simulation model is shown in Figure 3.3A, B.

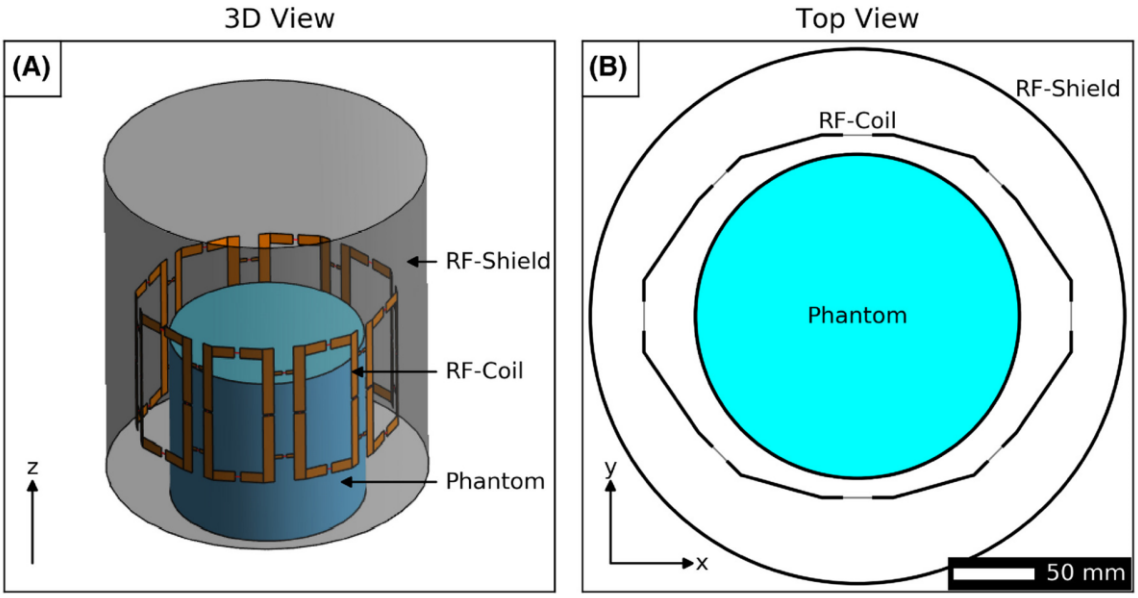

Figure 3.3 Simulation setup for RF coil validations at 297 MHz (7T). A) 3D representation and B) top view of an 8-channel pTx RF coil for 7T and a cylindrical phantom in the electromagnetic field simulation software (Reproduced from the Reference [63] CC BY 4.0, 2020).

3.3. Results

The results of the repetition experiments of the positioning system with the E-field probe is shown in Figure 3.4. The mean and standard deviation of the 10

consecutive measurements is 91.09 ± 1.00 V/m without robot movement. This result corresponds to a total of 1% uncertainty at the RF transmit and receive chain (Figure 3.4A). As can be seen in Figure 3.4B, the robot repositioning increases the uncertainty of the system to 3%, where the mean and standard deviation of the 10 consecutive measurements corresponds to 93.80 ± 2.58 V/m.

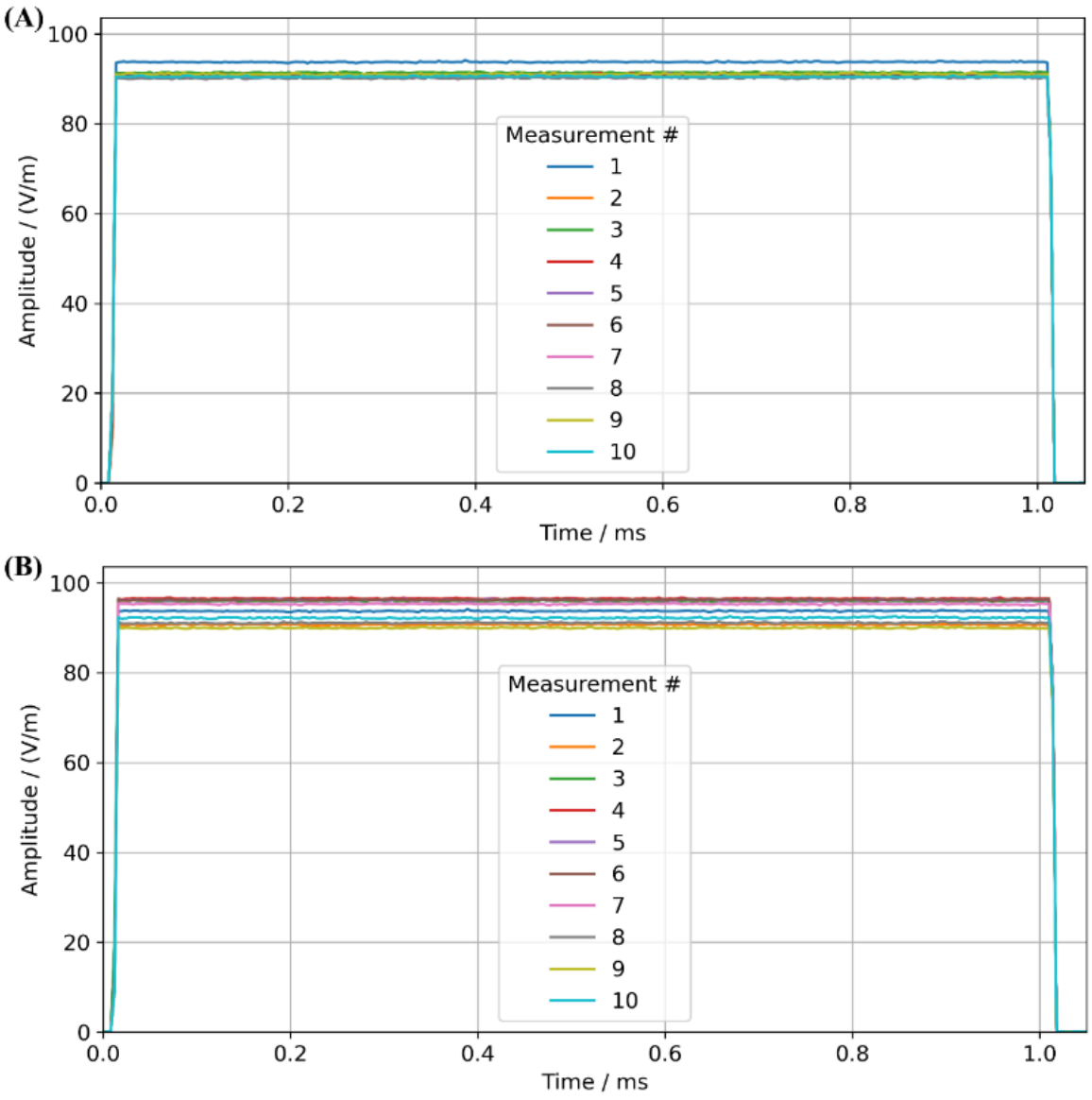

Figure 3.4 Results of the repetition experiments using the time-domain E-field probe is shown. (A) Results of 10-consecutive measurements without robot movement. The mean and standard deviation of the measurements are 91.09 ± 1.00 V/m. (B) shows the results of 10 consecutive measurements at the same location, where the robot retreats the probe and implant lead out of the phantom and repositions it again 10 times. The mean and standard deviation of the measurements are 93.80 ± 2.58 V/m.

The simulated and measured B_1^+ fields of the 8-channel RF-coil are shown in Figure 3.5 with an RMS difference of 6.3%. The maximum measured B_1^+ field shows a maximum of 27.9 μT/√kW and simulated maximum B_1^+ field shows 25.7 μT/√kW. Along the x-direction of the investigated area, the mean absolute difference between simulated and measured B_1^+ fields were 2.46 ± 1.24%. For the y-direction, it was 2.65 ± 0.89%.

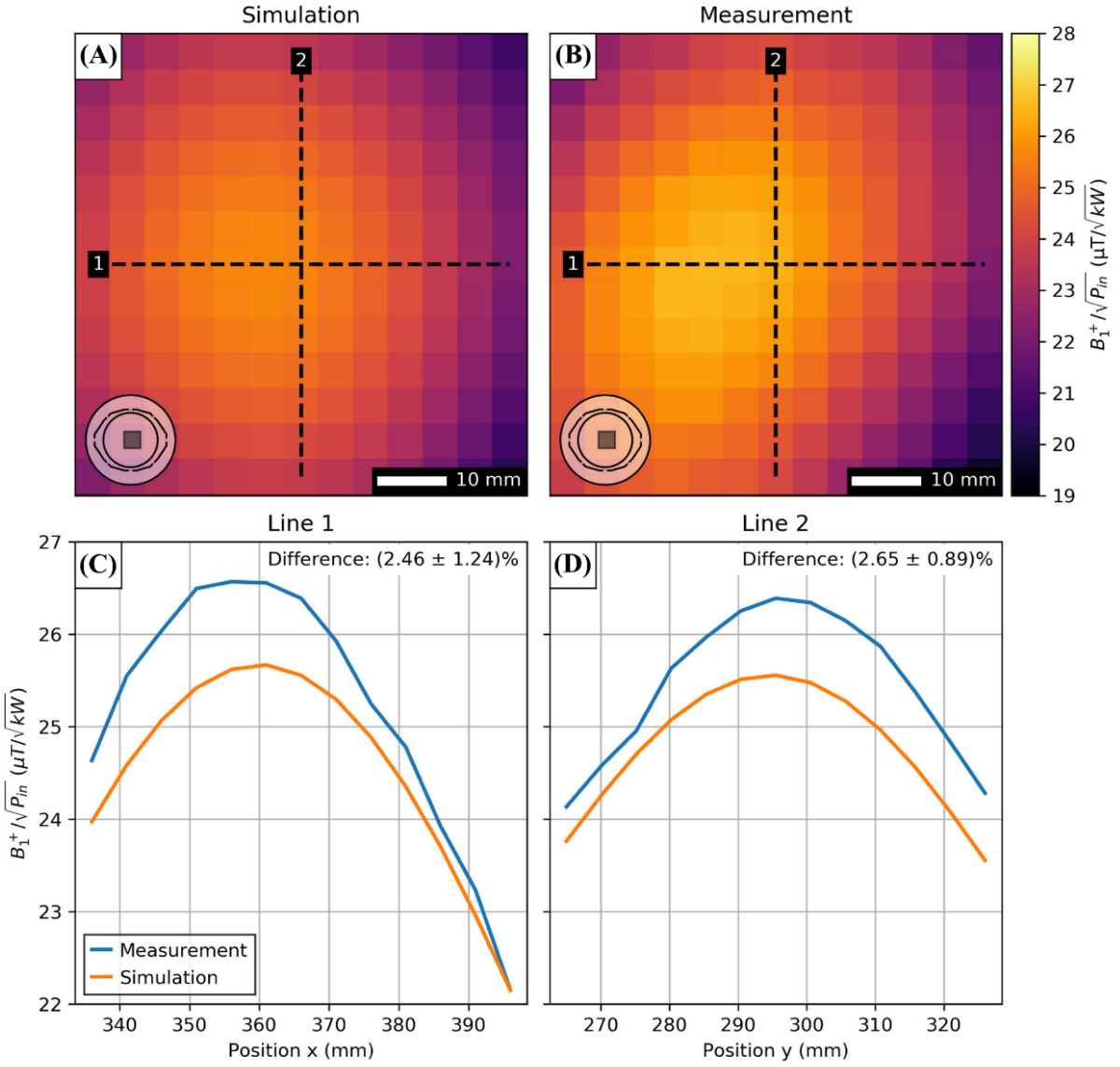

Figure 3.5 The results of the B_1^+-field validations are shown for A) simulated, and B) measured B_1^+ using the mapped time-domain H-field probe information inside the phantom (total area = 60 × 60mm², axis: x-y, spatial resolution 5 mm). Field comparisons between simulation and experiments in (A) and (B) are depicted across the horizontal line in (C) and the vertical line in (D) (Reproduced from the Reference [63] CC BY 4.0, 2020).

Temperature measurements from the thermistor embedded at the implant tip compared to fiber-optic probe readings are shown in Figure 3.6. The thermistor can detect temperature rises with high precision and resolution of about 100 µK and temporal resolution of up to 25 Hz; whereas these parameters were ~0.5 K and 5 Hz for the fiber-optic temperature probes. Consequently, the thermistor is more accurate capturing very small changes in temperature rise as it is depicted by the blue arrows in Figure 3.6, which corresponds to intentional 1-second breaks during RF transmission.

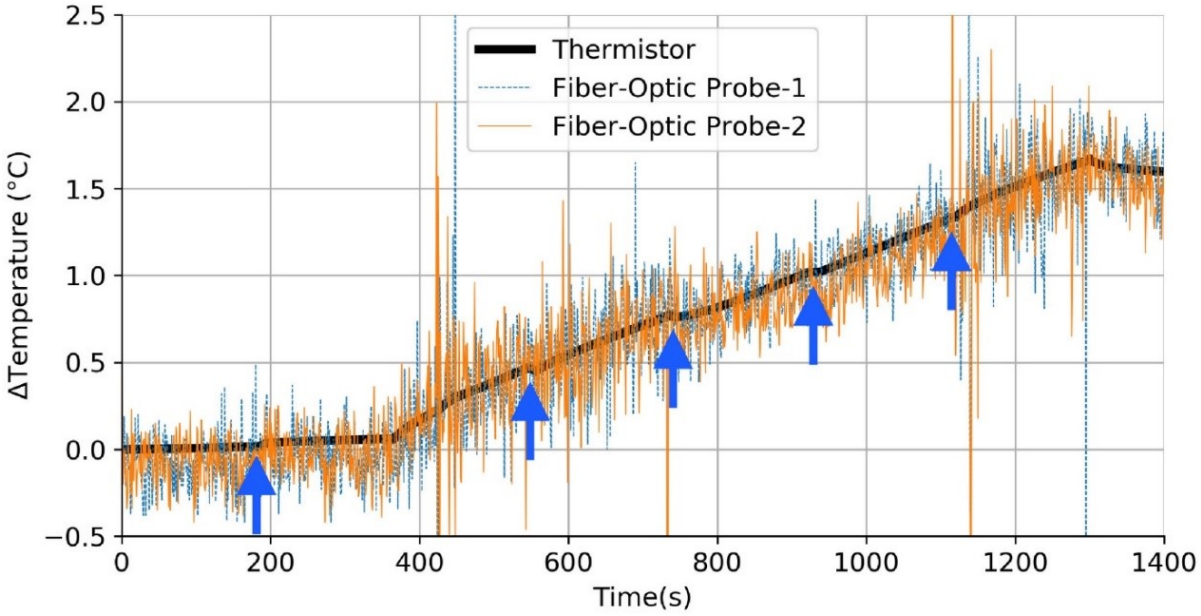

Figure 3.6 Measured temperature rise for two fiber optic temperature probes and one thermistor at the implant tip in a single RF-heating experiment. The dashed lines indicate the measurements by the fiber-optic temperature probes and the solid black line indicates the temperature measurements with the thermistor. The blue arrows point to the intended short interrupts of the RF source (Reproduced from the Reference [63] CC BY 4.0, 2020).

Further investigations and repetition experiments with the thermistor are shown in Figure 3.7. 10-consecutive temperature response curves for 64 different pTx RF-pulses are shown in Figure 3.7A. In Figure 3.7B, the temperature rise of a single 0.5 s long RF pulse is displayed, where the slopes have a mean and standard deviation of 13.9 ± 0.8 mK/s. Although the temperature rise may be affected by background temperature drifts during prolonged RF heating experiments with a multitude of pulses and implant positions, the dT/dt values are repeatable as shown in Figure 3.7C.

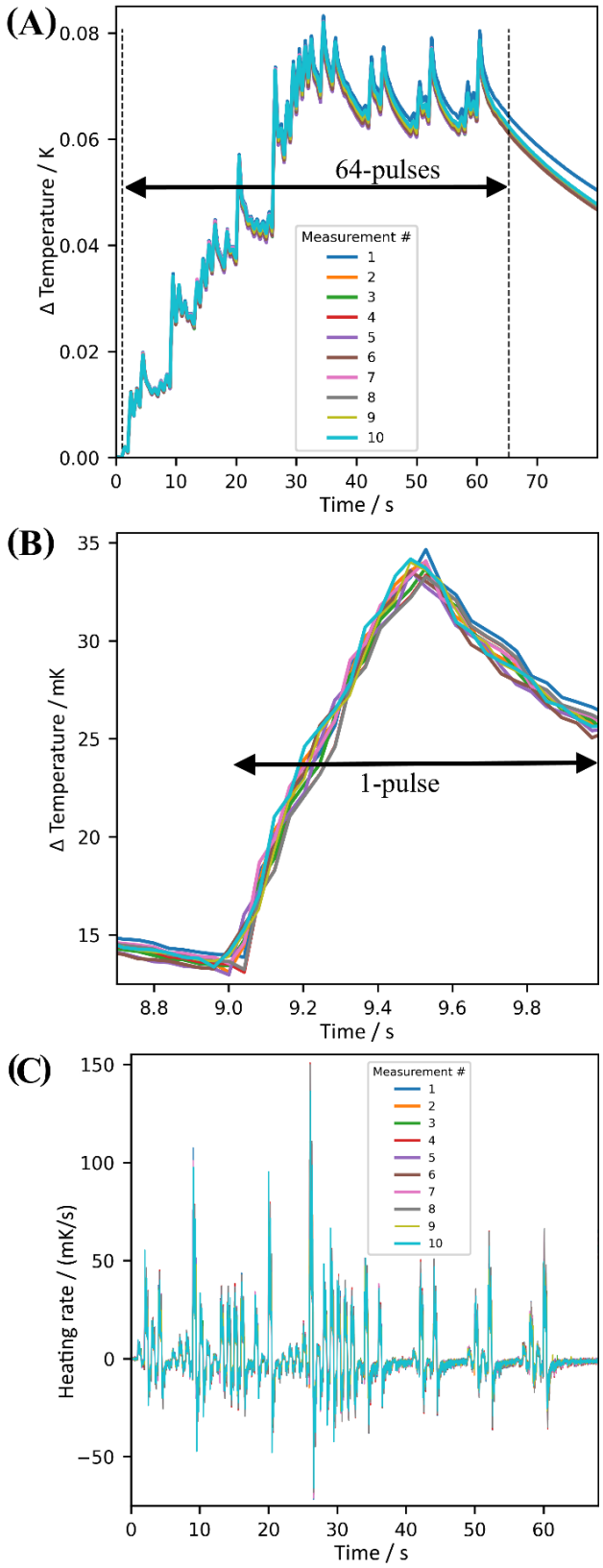

Figure 3.7 Results of RF heating experiments using the pTx implant safety testbed. A) Temperature measurements of an RF pulse train with 64 different pulses applied consecutively 10 times. The start and end of the RF excitations are shown with black dashed lines. The measurement curves are normalized to the temperature right before RF transmission. The first measurement (#1) shows different cooling rates after the RF pulse train compared to the last measurement (#10), which indicates a different cooling rate due to a larger temperature gradient B) Zoomed temperature rise from a single RF pulse repeated 10 times. C) Derivatives of the temperature increase from (A). (Reproduced from the Reference [64] CC BY 4.0, 2022)

3.4. Discussion

A versatile and flexible pTx implant safety testbed for extensive RF-safety testing of implants was presented and evaluated.

The broadband operation of the RF-chain supports a wide range of clinically relevant MRI field strengths from $B_0 = 0.5$T to $B_0 = 7$T. Although the system was demonstrated for an 8-channel transmission, it can easily be scaled up to 32-channels, thus allowing safety testing for a wide range of MRI frequencies with various pTx channel counts. In addition, various field probes and auxiliary sensors or the implant itself can be automatically positioned with the 3D robotic system, enabling extensive measurement evaluations of many RF heating scenarios.

The testbed shows good reproducibility. For E-field measurements, a standard deviation of less than 3% was found, when the implant had been consecutively repositioned to the same location between measurements. Simulated B_1^+ fields were successfully validated by measurements using an H-field probe with an RMS error = 6.3%. Some of the uncertainties present, are due to calibration uncertainties of the field sensors using the TEM cell (5%).[139]

The embedded thermistor ease the RF safety assessments compared to fiber-optic temperature probes with more than four orders of magnitude improved precision at a high temporal resolution. Temperature changes of a few mK can be easily detected at 40 ms temperature sampling rate. This allows the transmission of very short RF pulses at low amplitudes, facilitating fast acquisition of many implant positions under low background temperature changes. Repeatability of temperature measurements for different RF pulses is excellent, which can also be used for a reliable tip SAR estimation (Equation (2.6)).

The pTx implant safety testbed can be used standalone as it was demonstrated in this chapter. It can also be placed in and used together with the MRI scanner, which is demonstrated in the next chapter. In principle, the transmission stage could be used for MR imaging, if synchronized with the MR scanner hardware. However, in the current configuration, 20 W peak power may not be sufficient and additional amplifier stages or dedicated high-peak power narrow-band power

amplifiers would be needed.[129,130] However, it should be noted that this type of modification may limit the frequency range and the duty cycle of the current configuration. Another MRI related add-on could in principle be implemented, which would enable a feedback cycle for applications such as guidewire visualization using the pTx system.[73] One receiver channel of the testbed could be used to receive the trigger from the MRI system and another receiver channel to detect RF-induced currents from the guidewire and one channel for the clock synchronization[131] with external devices or MRI.

The current configuration of the pTx testbed is published as open-source hardware at www.opensourceimaging.org/ptx-implant-safety-testbed/, to allow and support additional developments by a larger community. This may enable reproducible RF-safety assessments of implants for comprehensive investigations at various implant safety scenarios, validations of simulations and experiments for implant safety assessments, investigation, and development of strategies for pTx mitigations. Finally, it fosters an increasing accessibility of pTx systems for RF safety or non-RF safety related research in MRI.

4. Sensor-based pTx mitigation of RF-induced heating

After the necessary setup of the pTx hardware for implant safety testing, sensor-based pTx mitigation methods to reduce RF-induced currents on the implant were investigated. In this chapter, techniques to mitigate RF-induced heating are presented using external and embedded sensor technology. In addition, methods to integrate MR imaging information based on only sensor measurements are applied within the mitigation schemes. The presented work has been published in the following conferences [140], [141], [142], [143] and journal articles [63], [64].

4.1. Introduction

Sensors could provide a solution for the RF safety problem of implants by providing patient and exam-specific measurements of hazardous exposures. This would also reduce uncertainties, compared to simulation or MR-measurement based assessment and mitigation methods of RF-induced implant heating. So far, however, sensors for pTx-based mitigation of RF-induced heating have only been applied with MR-interventional guidewires.[61,72,73]

The RF-induced currents on the guidewire were acquired using a time-domain current sensor, located far away from the guidewire tip and a coupling matrix based on Equation (2.26) was constructed. This matrix was then used to compute (Null Modes) NMs to reduce guidewire tip heating.[61] The NM transmission mode reduces implant currents, but does not consider any particular B_1^+ distribution, which is needed for imaging. Hence, it may lead to highly inhomogeneous B_1^+ and signal voids due to destructive interference of the B_1^+ at imaging regions. In order to generate adequate quality MR images with low RF-induced heating using this method, additional B_1^+-mapping sequences are needed to use this information in a linear combination of various NMs to optimize the imaging quality.[61]

The contribution to the RF-induced currents on the implant from each pTx-channel may vary significantly, however; not all coil elements are likely to induce significant currents on the implant. Therefore, treating some pTx channels as contributors to the implant heating and utilizing others for the imaging can

significantly improve the pTx mitigation efficacy for imaging purposes. Subsequently, it will be shown that this can be done without any lengthy and time-consuming procedures. For this purpose, we investigate and utilize the Orthogonal Projection (OP) method, which was first introduced already in 2015[62] but is the first time presented in detail in References [63,64] . It is conceptually similar to the null-mode approach[61] but aims to find a pTx transmission vector, i.e. a set of complex voltages to be applied to each transmit channel, that not only reduces RF-heating of the implant but simultaneously preserves image quality as much as possible.

This method is first explored using time-domain E-field sensors on mock implants. This includes investigations concerning the sensor location at the implant wire, which may impact results if the sensor is positioned far away from the implant tip.[144,145]

Time-domain sensors are bulky, however, while implants are small and fully immersed into the body making an in-vivo application of the sensors challenging in current clinical reality. Hence, small, and cheap RMS sensors were investigated as a much more practical approach, together with a methodology, the so-called sensor Q-Matrix ($\boldsymbol{Q_S}$), to prove the use of these sensors for OP and NM mode based pTx mitigations.

4.2. Mitigation of RF-induced heating using external time-domain E-field sensor

4.2.1. Methods

The measurement of RF-induced currents on guidewires was previously demonstrated by using time-domain sensors (TDS) which are either pick-up coils[146,147] or current sensors[61,72,73,148,149]. In the present work, a time-domain E-field sensor (E1TDSx SNI Speag, Zurich, Switzerland) was placed in proximity (~1 mm) to the implant lead at a distance 65 mm (in distal, z-direction) away from the tip to pick-up the E-fields generated by the pTx coil. The E-field sensor was placed perpendicular to the implant wire thereby measuring the radial E-field component. As this is a TDS, each RF coil channel contribution can be measured

in amplitude and phase using the E-field sensor. A complex valued steady-state pTx RF-excitation vector, $\boldsymbol{u}$ is transmitted as follows

$$\boldsymbol{u} = k \times (u_1, u_2 \dots u_N) \tag{4.1}$$

Where u_i is the amplitude of the applied sinusoidal voltage at pTx channel i, N is the number of pTx channels with the same phase reference and $k \in \mathbb{R}$ is the normalization factor for the same transmitted forward power such that

$$P_0 = \frac{\|\boldsymbol{u}\|^2}{8Z_0}, Z_0 = 50\ \Omega \tag{4.2}$$

Then, N voltage vectors are transmitted and the pTx transmission modes can be calculated. The OP method can be calculated similar to NMs. A complex-valued coupling matrix $\boldsymbol{\zeta}$ is obtained initially. For single sensor measurement (TD E-field sensor in this case), the phases that lead to coherent superposition and the amplitudes are weighted based on the measured TDS signal per channel or the eigenvector with the largest eigenvalue of $\boldsymbol{\zeta}$ yields maximum RF-induced currents, which is defined as the worst-case (WC) mode. Therefore, any pTx voltage excitation vector ($\boldsymbol{u}$) that is orthogonal to the WC vector ($\boldsymbol{u}_{WC}$) expected to dramatically reduce RF-induced currents on the tip. For example, considering conventional CP excitation vector ($\boldsymbol{u}_{CP}$) can be formalized for an N-channel pTx coil:

$$\boldsymbol{u}_{CP} = \frac{1}{\sqrt{N}} e^{-2\pi j/n}, n = 0, \dots, (N-1) \tag{4.3}$$

Then, projecting $\boldsymbol{u}_{CP}$ to the subspace that is orthogonal to the $\boldsymbol{u}_{WC}$ will yield an orthogonal projection vector:

$$\boldsymbol{u'}_{OP} = \boldsymbol{u}_{CP} - \boldsymbol{u}_{WC}\,(\boldsymbol{u}_{WC} \,.\, \boldsymbol{u}_{CP}) \tag{4.4}$$

Please note that both $\boldsymbol{u}_{CP}$ and $\boldsymbol{u}_{WC}$ are normalized vectors representing the same input power and $\boldsymbol{u}_{OP}$ is defined as a normalized vector of $\boldsymbol{u'}_{OP}$ to equalize the input power to $\boldsymbol{u}_{CP}$ and $\boldsymbol{u}_{WC}$. The OP method aims to take the implant hazard out of the CP vector (assuming $\boldsymbol{u}_{CP} \neq \boldsymbol{u}_{WC}$) but otherwise maintain as much as possible of

the (presumedly) good imaging properties of that parent vector. Unlike the NM method, the OP method has some image-quality preserving component already built in, therefore. Of course, the method works with any starting vector providing good image quality, it does not have to be the CP mode. As long as a good starting vector is known or can be guessed in advance, and for not too high field strengths (i.e., higher RF frequency), the CP mode is such a good guess, the OP vector can be computed directly from the acquired sensor signal and does not need any extra B_1^+-mapping and optimization for imaging quality.

As an example, numerical B_1^+ and temperature simulations demonstrate the effectiveness of the proposed OP method (Figure 4.1). As can be seen in the simulation results with an implant wire inside brain tissue (Figure 4.1Figure 4.1A), the RF induced currents around the implant wire create B_1^+ elevations around the implant tip in CP transmission mode as well as a corresponding temperature increase (Figure 4.1A and D). These are substantially suppressed by the OP transmission setting (Figure 4.1B, E, and F). In the central region of the brain imaging quality is significantly maintained (Figure 4.1C).

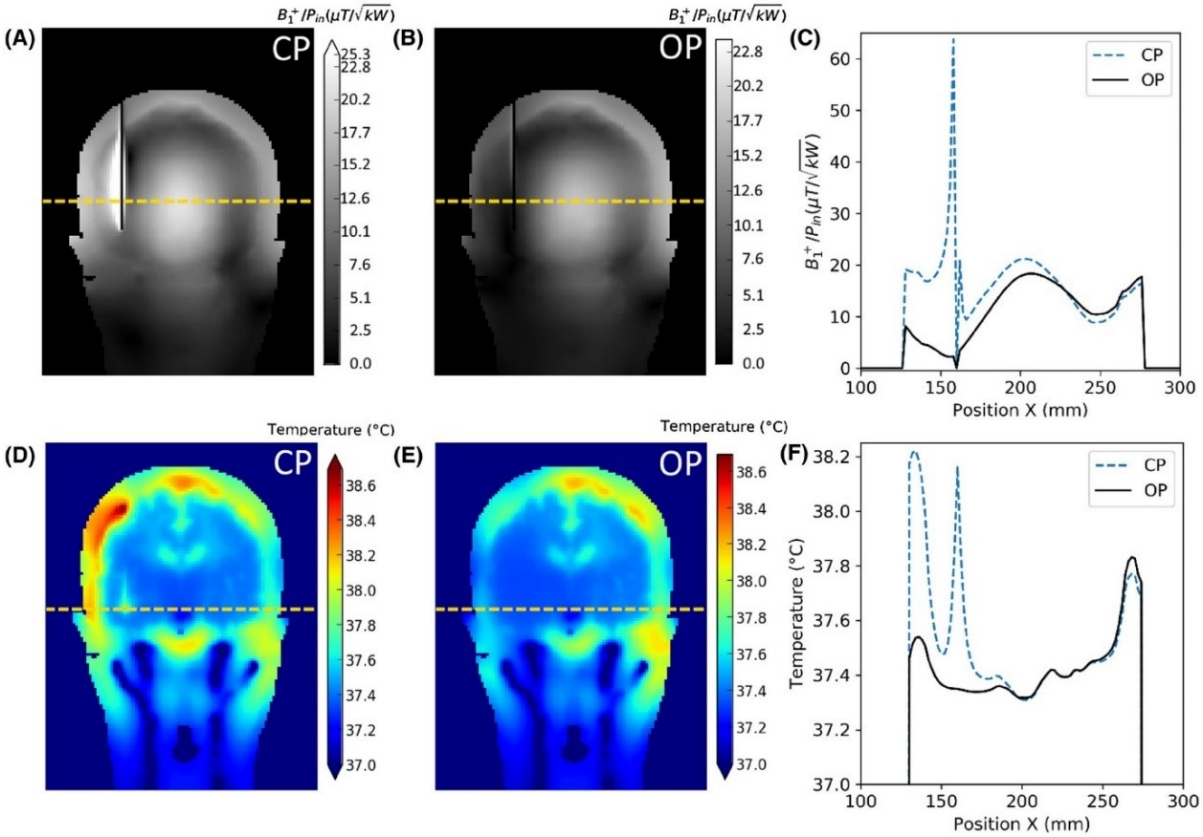

Figure 4.1 Numerical simulations to demonstrate the efficacy of the OP method that provides acceptable imaging quality while substantially reducing RF-induced implant heating. A) Calculated B_1^+ results for the reference CP mode with the implant. B) The B_1^+ results for the OP method at the same slice and equal transmit power. C) B_1^+ profile along the yellow dashed line for CP and OP transmission.D) The corresponding temperature increase for the CP mode and E) for the OP mode. F) Temperature profile coincide with the implant tip (dashed lines in (D) ad (E)) are shown where OP suppresses the RF-induced heating. (Reproduced from the References [62,63] CC BY 4.0, 2020).

Testbed experiments at 297 MHz

For 8-channel pTx experiments, the implant safety testbed was used with a calibrated average forward power of $P_{rms} = 1.4$ W and 1.28 ms long pulses at 297 MHz using the 8-channel 7T coil of the testbed system.[134] The subsequent 8 complex-valued radial E-field (E_r) on the implant (see Figure 3.2B) were measured as:

$$\boldsymbol{S}_{TDS} = (E_r(u_1), E_r(u_2), \dots, E_r(u_8)) \tag{4.5}$$

where $\boldsymbol{S}_{TDS}$ refers to the signals measured by the TDS. Then, pTx mitigation was done by computing the OP mode using the Equation (4.4). The performance of OP was assessed by comparing it to the conventional CP (Equation (4.3)) mode and the WC mode. As expected, the WC mode always produces the maximum RF-induced E-fields compared to CP and OP modes. This procedure was performed at three implant locations to verify the E-field measurements. Then, temperature experiments were performed at these three locations using the same pTx excitation vectors $\boldsymbol{u}_{WC}, \boldsymbol{u}_{CP}, \boldsymbol{u}_{OP}$ for 77 s long RF transmission.

To investigate the pTx mitigation capabilities of the proposed setup at multiple implant locations, the implant was immersed 90 mm into the phantom, and an area of 100 × 50 mm^2 plane was mapped with a 5 mm spatial resolution. The subsequent RF-induced E-fields from the pTx excitation modes ($\boldsymbol{u}_{WC}, \boldsymbol{u}_{CP}, \boldsymbol{u}_{OP}$) at each implant position were measured using the same forward power $P_{rms} = 1.4$ W.

3T MRI Experiments

To investigate the imaging quality of the OP method compared to the CP mode, MRI experiments were performed at a pTx capable 3T MR scanner (Verio, Siemens Healthineers, Erlangen, Germany). The scanner is equipped with eight channel RF amplifiers with maximum 8 kW peak-power per channel. The amplifiers' amplitude and phases can be adjusted from a GUI based program in a different computer supplied by the manufacturer. The pTx software version of the scanner is Step 1.

The setup for the MRI experiments is shown in Figure 4.2. A commercial 8-channel pTx RF head coil (RAPID Biomedical, Rimpar, Germany) was used for the transmission. The PVP mixture was placed into the coil by using a container (200 × 260 × 35 mm^3). The implant was positioned 45 mm away from the right side of the container. The E-field probe was positioned close to the implant by attaching it to a 2600 mm long rod that was controlled by the positioning system, which was placed at the end of the patient table as shown in Figure 4.2A.

In addition, the impact of the E-field probe location with respect to the implant tip was evaluated. The pTx excitation modes, $\boldsymbol{u}_{WC}, \boldsymbol{u}_{CP}, \boldsymbol{u}_{OP}$ were determined by measuring $\boldsymbol{S}_{TDS}$ at 15 different E-field sensor locations starting from the tip using

10 mm steps. The corresponding E-fields on the implant were measured for all three pTx excitation modes. Heating experiments were performed at the E-field sensor location 90 mm away from the tip. The embedded thermistor (Figure 3.2) was used to monitor the temperature at the implant tip.

Finally, imaging experiments were performed by using the MR scanner's 8-channel pTx system, where pTx RF excitation amplitude and phases transmitted via scanner's console. A gradient-echo (GRE) sequence was transmitted, which has a 1.2 ms long sinc-shaped RF pulse. Again, $\boldsymbol{S}_{TDS}$ was acquired with the E-field probe positioned 110 mm away from the tip. Then, heating experiments were performed with the GRE sequence where the total time was increased to 50 s with a 55 V peak RF amplitude and a repetition time (TR) of 4.5 ms. Finally, MRI images of CP and OP modes were acquired with the same RF power. A GRE sequence with the following parameters was used for imaging: (spatial resolution = (1.2 × 1.2 × 5.0mm^3), TR = 7.8 ms, TE = 3.06 ms, number of averages = 2).

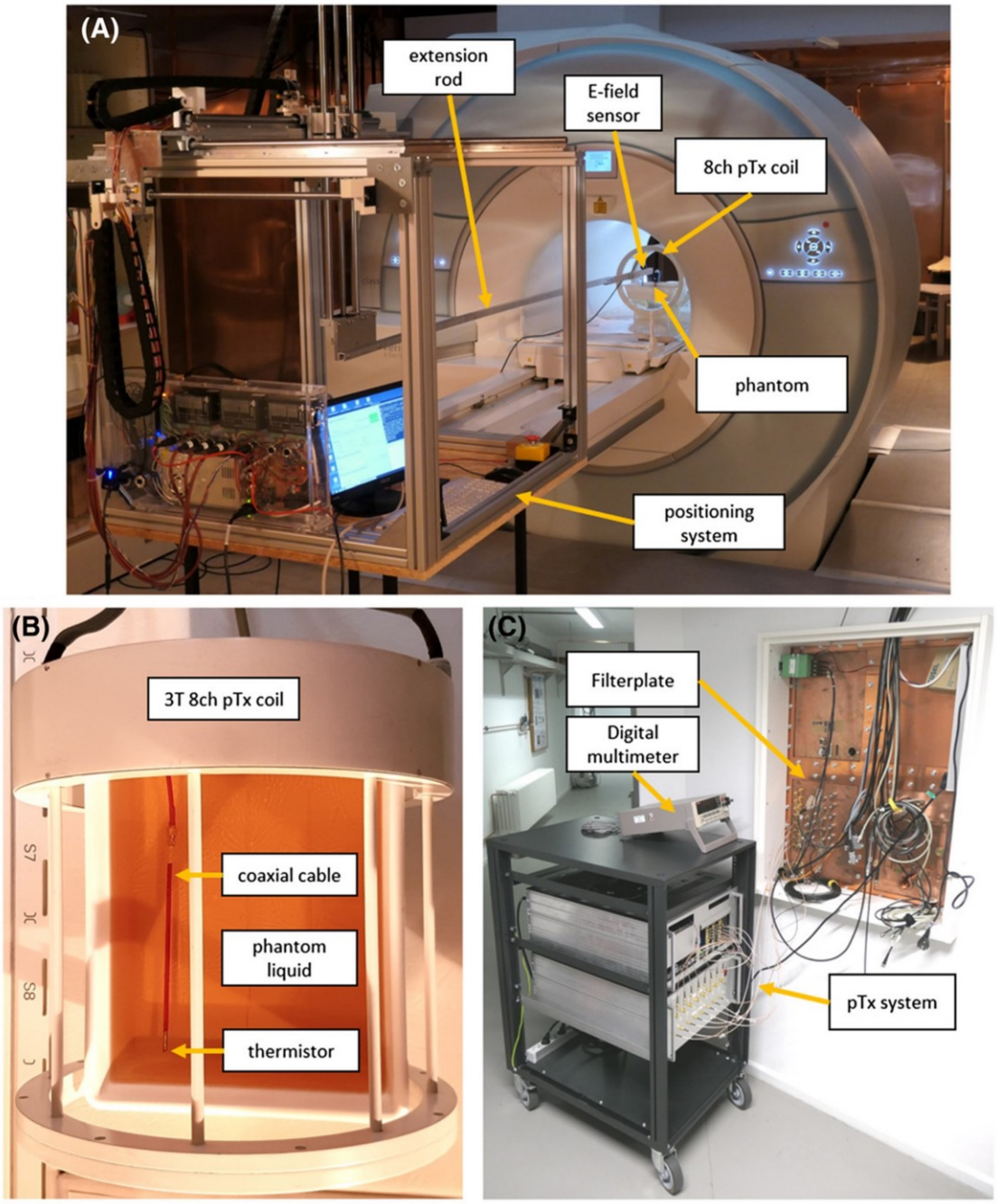

Figure 4.2 MRI experimental setup using time-domain E-field sensor-based pTx mitigations. A) Photograph of the measurement setup inside a 3T MRI using the pTx implant safety testbed. An extension rod was used to hold the E-field sensor and measure the induced radial E-field along the implant. B) Photograph of the 8-channel pTx RF coil used for excitation with the implant inside a rectangular PVP phantom liquid C) Photograph of the console, power amplifiers, and digital multimeter located outside the scanner room and connected through the filter plate to the 8-channel pTx RF coil and the implant lead for thermistor readings (Reproduced from the Reference [63] CC BY 4.0, 2020).

4.2.2. Results

Testbed experiments at 297 MHz

The experimental implant locations of the pTx mitigations and temperature experiments in the phantom are labeled as P1, P2, and P3 and shown in Figure 4.3. The measured E-field contributions from the different pTx channels to the implant are mainly affected by the proximity of the pTx channels to the implant lead and can be observed in the $\boldsymbol{S}_{TDS}$ signals. The transmission vectors $\boldsymbol{u}_{WC}, \boldsymbol{u}_{CP}, \boldsymbol{u}_{OP}$ show that WC mode always has the largest E-field on the wire followed by CP mode. Whereas OP substantially reduces the induced E-field around the wire. The E-field reduction factor for the CP versus OP was at least 2.2 times higher at all three positions. The maximum reduction factor was 3.8 times at the P2, where $\boldsymbol{E}_{r,CP}$ had already minimum at this location compared to P1 and P3.

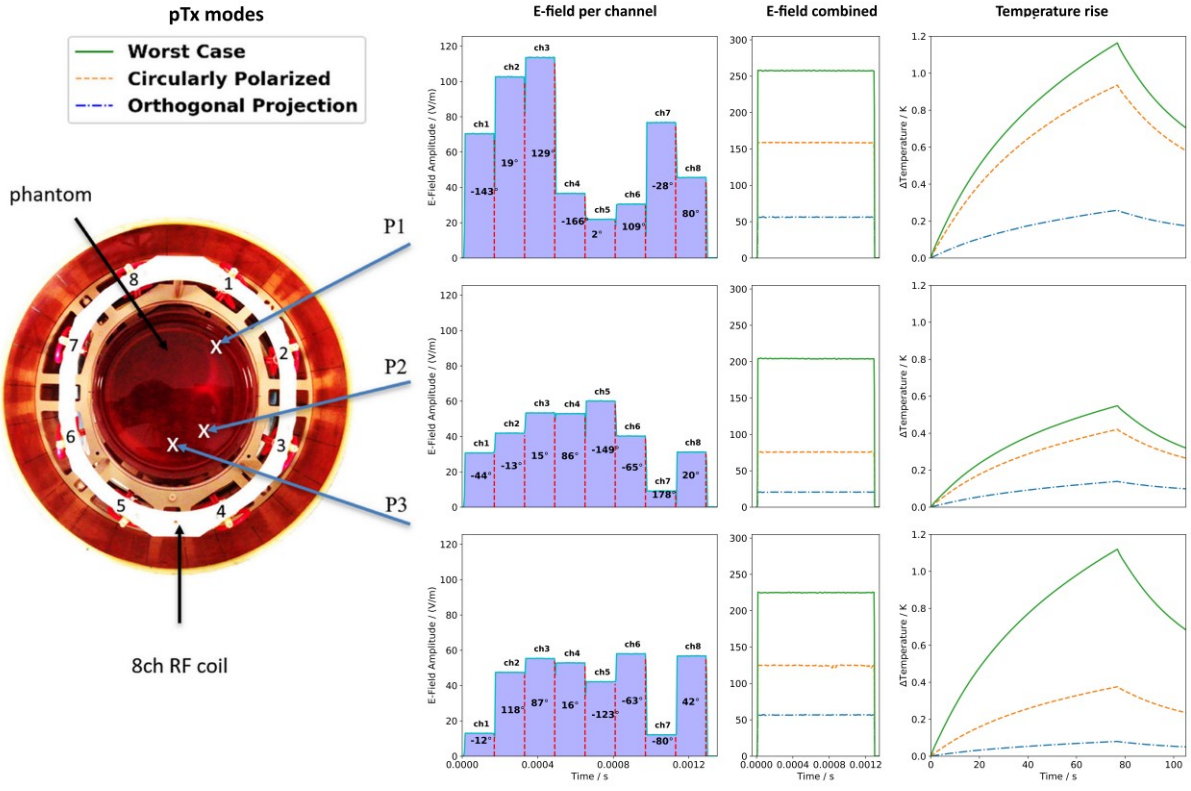

Figure 4.3 The results of the mitigation experiment at three different implant positions (P1, P2 and P3) in the phantom inside an 8-channel RF coil for 7T. RF-induced E-fields and temperatures recorded for these positions. The magnitude and phases of the E-fields are plotted for consecutive single-channel transmission of each channel of the RF coil. The magnitude and phase measurements for all channels take ~1 ms and are used to calculate WC, CP, and

OP modes. The RF-induced E-fields and temperatures are lowest for the OP method compared to WC and CP modes. (Adapted from the Reference [63] CC BY 4.0, 2020).

The results of the 77 s long temperature experiments as shown in the last column of Figure 4.3 depicts that suppression of RF-induced heating at the implant tip was successful using the E-fields at all three locations even though the E-field probe was located 65 mm away from the tip. WC-mode heating was maximum at all locations as expected. The OP mode could effectively suppress the RF-induced heating compared to CP mode at all locations with reduction factors of 3.0 to 4.8. It should be noted that the highest reduction factor in temperature rise is found at P3, not P2, where the highest E-field reduction factor was found. The summary of all measurements is given in Table 4-1.

Table 4-1 Results of E-fields and temperatures measured at three different positions and RF excitation settings (Figure 4.3).

Position	*E*-field / (V/m)			Δ Temperature rise / K		
	WC	CP	OP	WC	CP	OP
P1	257	159	56	1.16	0.94	0.26
P2	254	76	20	0.55	0.42	0.14
P3	225	125	57	1.12	0.38	0.08

The results of pTx mitigation experiments at 210 different implant lead locations spanning an area of 100 mm × 50 mm with 5 mm resolution are shown in Figure 4.4. For the CP data, it can be seen that a local minimum exists around the phantom center which is expected due to the E-field distribution of the RF coil in this transmission mode.[50] Moving closer to the RF-coil increases the E-field around the wire for all modes. The WC mode was highest compared to CP and OP for all implant locations, while OP mode reduced implant tip E-fields substantially and consistently. The maximum mitigation factor using OP mode was more than 26 and 55 times compared to CP and WC modes, respectively. In 14% of the investigated locations, the OP had more than 5 times reduced E-fields compared to the CP mode, while in 88% of the investigated locations E-fields were reduced by a factor of two or more.

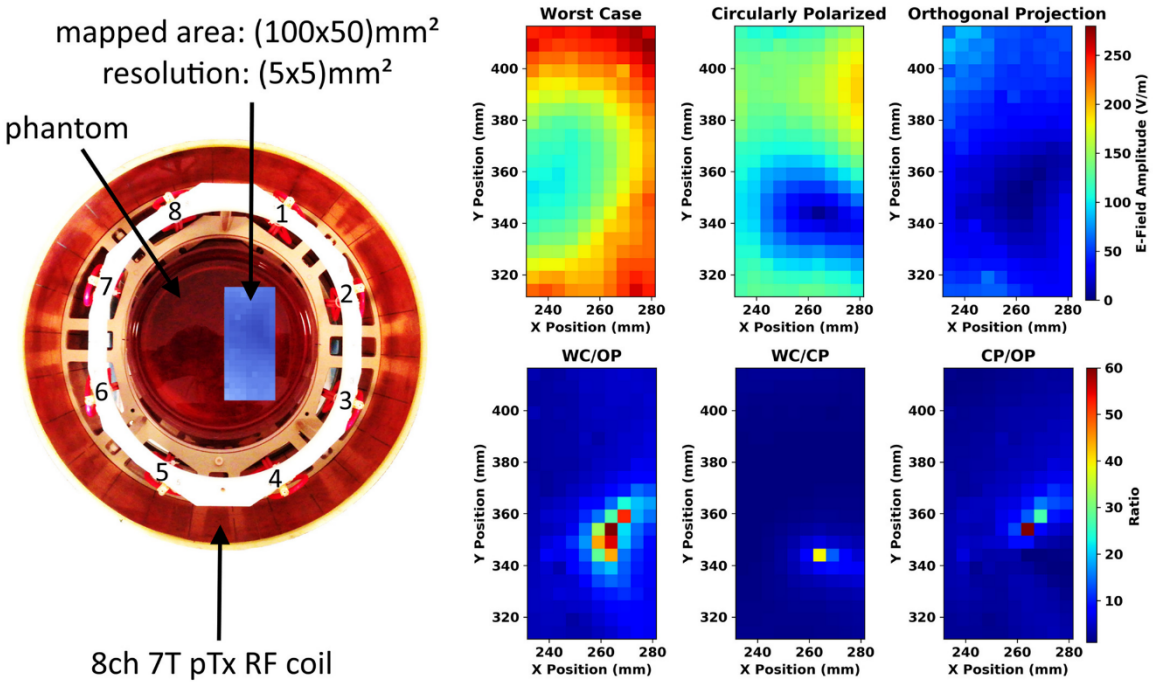

Figure 4.4 Results of 210 different implant locations inside a cylindrical phantom. An area of 50 × 105 mm² and resolution of 5 mm² was investigated and the E-fields were measured to calculate WC and OP transmission modes. The results for each mode; WC, CP and OP are shown in the top row. The bottom row shows the ratios of the modes. Please note that moving the implant wire by only a 5 mm can alter the E-field magnitude by more than a factor of 5 in CP mode. (Reproduced from the Reference [63] CC BY 4.0, 2020)

3T MRI experiments

The results of the E-field mapping along the implant and corresponding temperature measurements are shown in Figure 4.5. The absolute value of the E-field along the wire varies depending on the sensor location, which may indicate sensor positioning error deviating from its perpendicular orientation to the wire. Nevertheless, the OP method reduces E-field on the implant at all sensor positions Figure 4.5A. The reduction factor of the OP ranges between 6 to 45 times compared to WC mode, and 3 to 22 times compared to CP mode as shown in Figure 4.5B.

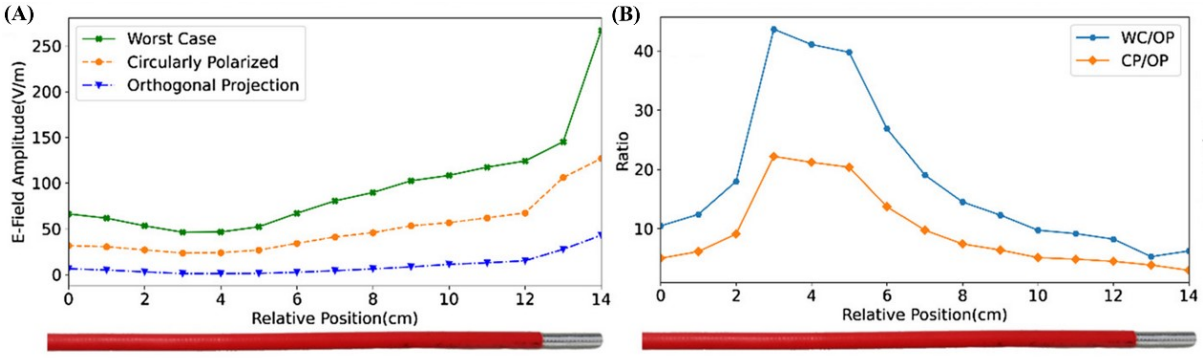

Figure 4.5 The results of the sensor positioning experiments by altering the E-field sensor position in 10 mm steps. A) Measured radial E-field along the implant lead at 15 positions and WC, CP, and OP pTx excitation vectors demonstrating OP mode is successful at all sensor positions. B) Position-dependent ratios (WC/OP) and (CP/OP) of the measured E-fields. (Reproduced from Reference [63] CC BY 4.0, 2020).

Heating experiments based-on the $\boldsymbol{S}_{TDS}$ measurements at a distance 90 mm away from the tip of the implant are shown in Figure 4.6. The temperature rises after 8 seconds of RF heating were 24 mK and 6 mK for WC and CP mode, respectively. There was no detectable RF-induced heating for the OP mode.

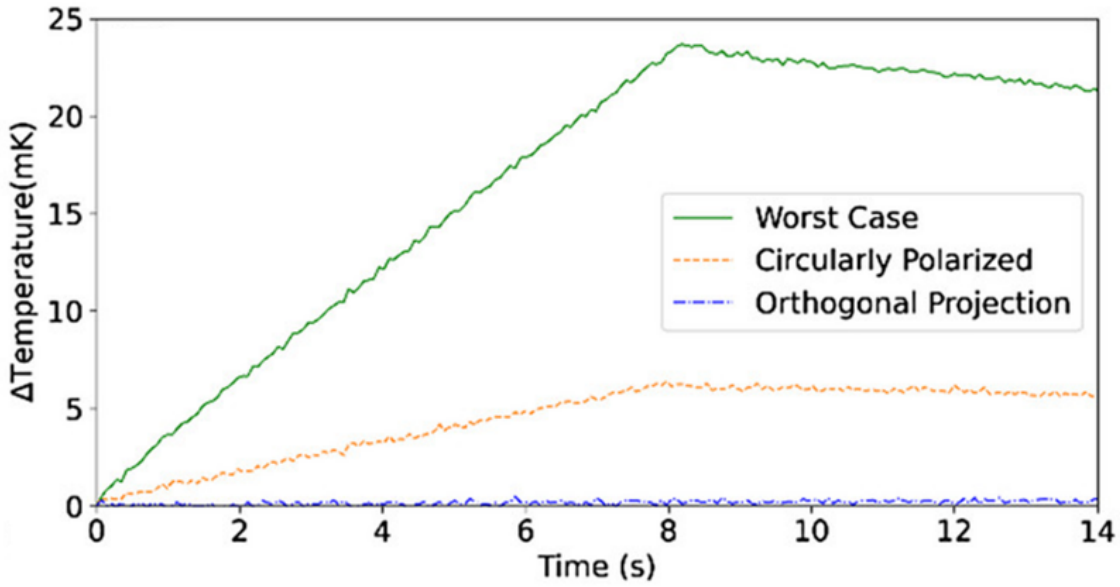

Figure 4.6 RF-heating experiments utilizing the E-field sensor measurements to determine WC and OP transmission vectors in MR. OP substantially reduces tip heating compared to CP and WC modes. (Reproduced from the Reference [63] CC BY 4.0, 2020).

The imaging results acquired within the 3T MRI system are illustrated in Figure 4.7A and Figure 4.7B. Using the same $\boldsymbol{S}_{TDS}$ pulses and the calculated OP transmission mode the resulting MR images are shown in Figure 4.7B and the conventional CP mode MR images are shown in Figure 4.7A. The preliminary imaging results show that OP reduces RF-induced heating while maintaining imaging quality. Furthermore, the induced E-fields on the implant are shown for three pTx excitation modes in Figure 4.7C. During phase coherence mode (the same phases as WC but, the amplitude of the channels has the same magnitude) the maximum E-field was detected, the OP mode successfully suppressed the E-field, which was again cross-validated by temperature measurements at the implant tip as shown in Figure 4.7D.

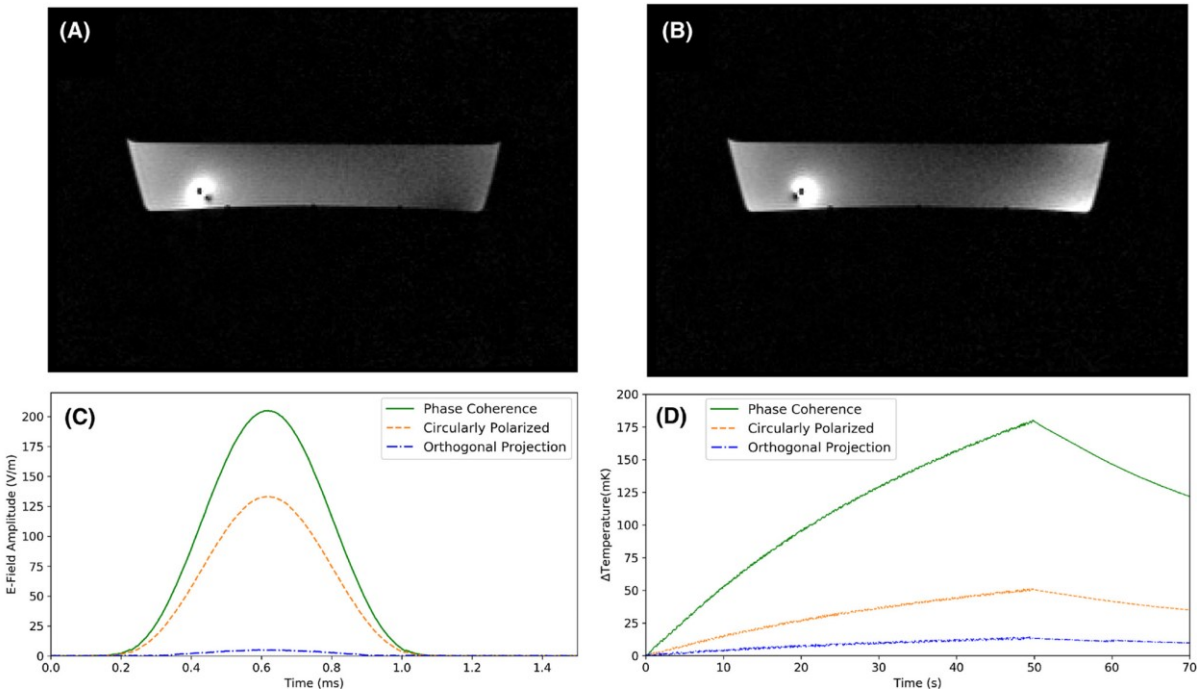

Figure 4.7 Axial GRE images at 3T utilizing an 8-channel pTx system A) CP mode and B) OP mode images. The B_1^+ imaging artifact indicates the location of the implant wire. C) RF-induced E-fields measured at the implant wire for a phase coherent (WC-based phases but equal amplitudes per channel), the CP and OP mode transmission with the sequence. All three modes were transmitting with the same forward power. D) corresponding temperature curves for RF-induced tip heating performed with all pTx transmission modes. The TDS was widhdrawn and its electronics together with the electronics of the positioning system were switched off to suppress the electromagnetic interference from these devices. (Reproduced from the Reference [63] CC BY 4.0, 2020).

4.3. Mitigation of RF-induced heating using embedded RMS sensors

In this following section, the introduced methods for the pTx mitigations are further improved as time-domain E-field sensors are currently too bulky and expensive to be embedded in implants for an application of RF safety assessment and pTx mitigations. An alternative method was developed that can be implemented using small footprint (<1.5 mm^3) and cheap (<1 €) RMS sensors. Compared to TD sensors, RMS sensors convert the averaged dissipated power to rectified electrical signals, which can be found in terms of temperature or E-fields. RMS sensors do not contain phase information, which could be used to apply the presented TDS methodology to calculate complex-valued pTx excitation vectors. However, this information can be extracted by using the introduced method, the so-called sensor Q-Matrix ($\boldsymbol{Q_S}$).

4.3.1. Methods

Sensor Q-Matrix

The quadratic form of the Q-Matrix to compute SAR for a local voxel is given in Equation (2.22). The Q-matrix formalism can be extended for implant safety. Considering the elongated implant wire in the pTx scenario, a local SAR voxel is located at the implant tip where typically the stimulation electrodes are located and the heating is the highest.[2,150] The measurands can be used to construct a matrix, which is a full analogy to Q-matrix in Equation (2.22):

$$X = \boldsymbol{u^H Q_s u}, \tag{4.6}$$

where X refers to the RMS sensor measurements. As RMS sensors do not have phase information, N^2 measurements are required to construct the sensor Q-matrix ($\boldsymbol{Q_S}$) for an N-channel pTx system as follows:

$$Q^X_{S,kl} = \begin{cases} (X_{kl} - X_k - X_l) + j\left(X^{\dagger}_{kl} - X_k - X_l\right) & \text{for } k \neq l \text{ and } k < l \\ (X_{kl} - X_k - X_l) - j\left(X^{\dagger}_{kl} - X_k - X_l\right) & \text{for } k \neq l \text{ and } k > l \\ 2X_k & \text{for } k = l \end{cases} \tag{4.7}$$

where X_{kl} is measured when pTx channel k and l transmit with the same amplitude without phase difference between them. $X_{kl}^{\dagger}$ is measured such that pTx channel k and l transmits with the same amplitude and $90°$ phase difference to each other. The diagonal of $\boldsymbol{Q_S}$ is filled when only a single k channel transmits and X_k is measured. The RMS measurement can be E-fields probed by a Schottky diode or temperatures probed by a thermistor. The measured voltages, as they can be referred to induced tip E-field, are quadratically scaled, which can then be used to estimate tip SAR. Tip temperature rise (dT/dt) measurements are proportional to SAR when performed over a short period of time (see Equation (2.6) and Figure 2.3).[151,152] In the following context, $\boldsymbol{Q_S}$ will be denoted as $\boldsymbol{Q_S^E}$ if it is calculated based on RF-induced E-fields, and $\boldsymbol{Q_S^T}$ for dT/dt measurements. In order to determine the modes of pTx excitations, an eigenvalue decomposition of $\boldsymbol{Q_S}$ can be performed:

$$\boldsymbol{Q_S}\,\boldsymbol{v} = \lambda \boldsymbol{v} \tag{4.8}$$

where λ denotes eigenvalues and $\boldsymbol{v}$ the corresponding eigenvectors. With this information, the OP mode using Equation (4.4) can be computed for the pTx mitigation. Similarly, NM modes can be obtained by using either singular value decomposition as shown in Equation (2.27), or eigenvalue decomposition in Equation (4.8). For experimental simplicity, only a single NM vector with the lowest eigenvalue was used for the experiments.

Implant configurations for the $\boldsymbol{Q_S}$ experiments

For the experimental demonstration two mock implants were used for the $\boldsymbol{Q_S}$ experiments as shown in Figure 4.8.

1- A category (CAT)-8 (Figure 4.8A and B) cable was modified such that 25 mm insulation was removed at the implant tip. Then, one of its shielded twisted pair wires was connected to a thermistor (NCP 18XH103F03RB, $R_{25°C} = 10$ kΩ, Murata Manufacturing, Nagaokakyo, Japan). A wire from another twisted pair was connected to the cathode of a Schottky diode (MMDL101T1G, ON Semiconductor, Phoenix, AZ, US) and the anode was

soldered to a 2.5 mm copper wire, serving as an antenna to enhance the sensitivity to E-fields. The latter step was necessary because the peak power in the testbed setting is limited to 20 W in contrast to the high peak powers (>1 kW) provided by MR system amplifiers. For the ground reference, the outer shield of the cable was used. The Schottky diode rectifies RF-induced voltages at the tip of the implant and can be used to measure E-fields[153–155]. It should be also mentioned that CAT-8 cable shields each twisted pair and the outer most layer before the insulation, which significantly reduces spurious RF interferences coupling along the cable. In addition, these independent twisted pairs can be utilized for simultaneous E-field and temperature measurements to compare $\boldsymbol{Q_S^T}$ and $\boldsymbol{Q_S^E}$.

2- A thermistor (NCP 18XH103F03RB, $R_{25°C} = 10$ kΩ, Murata Manufacturing, Nagaokakyo, Japan) was embedded at the tip of a semirigid coaxial cable as shown in Figure 4.8C and D. The terminals of the thermistor were connected to the inner and outer conductors of the wire. 15 mm insulation was removed from the tip of the wire.

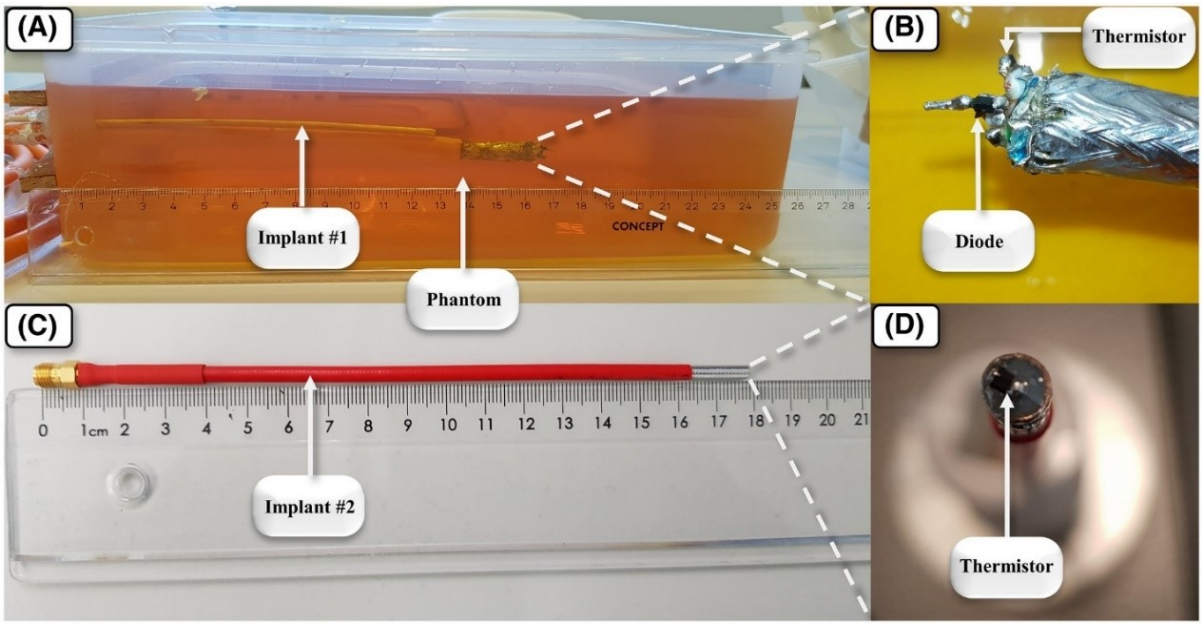

Figure 4.8 The photographs depict the implants with RMS sensors (diode and thermistor) embedded at the tip for $\boldsymbol{Q_S}$ assessment, pTx mitigation of RF-induced heating. In panel (A), a CAT-8 cable placed into a PVP phantom with embedded diode (1.70 × 1.25 mm^2) and thermistors (1.6 × 0.8 mm^2) as shown in Panel (B). A small extension wire is utilized to increase E-field sensitivity in regions of low E-fields due to the low peak power of the pTx safety testbed experiments. In higher transmitted RF magnitudes in the MR system, the extension can be detached. A

low-pass filter was employed for both thermistor and diode measurements. C) A 180 mm long coaxial cable as an implant with embedded thermistor at the tip (Figure 3.2). D) Photograph of the coaxial cable with thermistor shown in (C). (Reproduced from the Reference [64] CC BY 4.0, 2022).

Implant safety testbed experiments at 297 MHz

In the testbed experiments, the implant safety testbed was configured to 297 MHz (7T) and the same phantom introduced in the Section 3.2.3. and 8-channel pTx RF coil described in section 3.2. was used. Mock implant #1 was used in the testbed experiments.

$\boldsymbol{Q_S^E}$ acquisition and characterization

The transmitted forward power for the RF pulsetrain to obtain $\boldsymbol{Q_S^E}$ was 2.86 W per channel. A single element, $\boldsymbol{Q_{S,kl}^E}$,was obtained with a 200 µs pulse that is followed by a 100 µs idle time. In total $N^2 = 64$ measurements were acquired to construct a single $\boldsymbol{Q_S^E}$. All $\boldsymbol{Q_S^E}$ measurements have been quantized by the testbed ADC. The total acquisition time for an 8-channel $\boldsymbol{Q_S^E}$ is 19.2 ms with this experimental setup.

$\boldsymbol{Q_S^T}$ acquisition and characterization

Temperature measurements for the $\boldsymbol{Q_S^T}$ were performed using the same instrumentation described in section 3.2.4. The temporal resolution of the temperature measurements was adjusted to 40 ms. Then, RF pulses with a rectangular envelope were transmitted (2.86 W) for 0.5 s. After each RF-pulse, a 0.5 s cooling period was applied. For this 8-channel setup, a single $\boldsymbol{Q_S^T}$ took 64 s. As $\boldsymbol{Q_S^T}$ captures response of the implant using temperature information, background temperature fluctuations may affect the $\boldsymbol{Q_S^T}$ measurements as the acquisition time increases. This effect was minimized by subtracting the baseline drift and temperature gradient for each $\boldsymbol{Q_{S,kl}^T}$. Overall, ten $\boldsymbol{Q_S^T}$ acquisitions with 120 s time intervals in between in order to assess the repeatability of the results under different background temperature conditions.

pTx mitigation experiments at multiple implant locations

All pTx mitigation methods WC, OP, and NM were investigated using RMS sensors and the $\boldsymbol{Q_S}$ acquisition method and compared to CP mode excitation. As mock implant #1 was equipped with both sensors, $\boldsymbol{Q_S^E}$ and $\boldsymbol{Q_S^T}$ were independently investigated for each implant position. The feasibility of the $\boldsymbol{Q_S}$ method was rigorously investigated by changing the implant location to alter the incident E-field. Due to lengthier $\boldsymbol{Q_S^T}$ acquisitions (64 s per location), seven implant positions in the phantom were tested using both methods for a brief comparison. Then, $\boldsymbol{Q_S^E}$ was acquired at 154 different implant locations in an axial plane (140 × 100 mm^2) of the phantom with 10 mm^2 spatial resolution. At each location, 64 distinct RF pulses to acquire $\boldsymbol{Q_S^E}$ were transmitted via the pTx console.

For all pTx excitation methods, the total average forward power was 2.86 W, and the implant was immersed 120 mm into the phantom. For all pTx excitations at each implant position, 2 s long RF-heating experiments with an average total power of 2.86 W were performed to assess the effectiveness of the $\boldsymbol{Q_S}$ method.

MRI experiments at 3T

MRI experiments were performed to assess the $\boldsymbol{Q_S^T}$ and $\boldsymbol{Q_S^E}$ in different pTx coils and imaging performance of pTx excitations. The same 3T MR scanner described in 4.2.1. ,pg. 70 was used for the experiments.

3T MRI experiments using $\boldsymbol{Q_S^T}$ and two-channel body birdcage coil

The experimental setup for the two-channel body coil experiments is displayed in Figure 4.9A. The cylindrical phantom (see 3.2.3.) was placed into the body coil and mock implant #2 was immersed 95 mm deep into the phantom. The implant was connected to the filter plate of the scanner's Faraday cage with a long coaxial extension cable. From the outer side of the filter plate, the cable was connected to the digital multimeter via a low-pass filter (SLP-1.9+, Mini-Circuits, NY, US) to read thermistor's resistance.

In the first set of experiments, the scanner used normal operation mode or the CP transmission. In this mode, the thermistor-based temperature measurements

were acquired with the nominal flip angles that range from 10° to 90° with 10° increments. A GRE sequence with TR of 15 ms which includes 2 ms long RF pulses was applied. The transmitted RF-pulses were measured with a pick-up coil and an ADC card (M3i.4142, Spectrum Instruments, Grosshansdorf, Germany). The relative powers of the transmitted pulses were calculated by integrating the received sinc-envelope pulses with a pick-up coil.

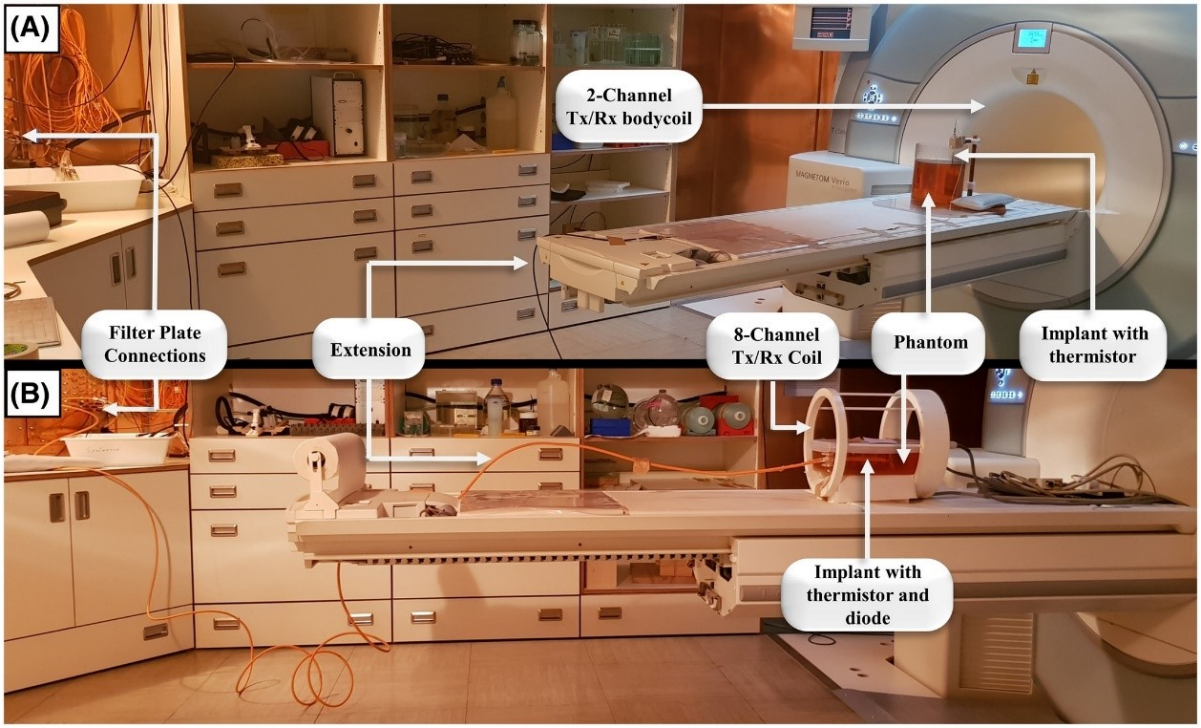

Figure 4.9 Experimental setup within a commercial 3T MRI system with pTx capabilities. Two different experimental settings were performed: A) using the two-channel body birdcage coil from the MR system for transmission into a cylindrical phantom and implant#2 with an embedded thermistor and B) using an 8-channel Tx/Rx RF coil for transmission into a rectangular phantom, and implant#1 with embedded thermistor and diode. (Reproduced from the Reference [64] CC BY 4.0, 2022).

In the second set of experiments, the scanner was run in pTx mode. The two channels of the body coil were driven by the pTx system. Two channel body coil can be considered as the most basic pTx scheme. The accessibility to the two channel body coil could be easier as it requires the least hardware modification to a “single channel” commercial system. For the $\boldsymbol{Q}_S^T$ acquisition in the two-channel body birdcage coil, $N^2 = 4$ measurements were acquired. For each pulse, 4 to 5 s

RF pulses were applied that are followed by 2 s cooling cycle. For the $\boldsymbol{Q}_S^T$-based predictions, two different implant locations were investigated.

Imaging experiments using $\boldsymbol{Q}_S^E$ and eight-channel pTx

The 8-channel pTx experimental setup is shown in Figure 4.9B. The commercial 8-channel pTx head coil introduced in the section 4.2.1. was used for RF-transmission and signal reception. A phantom container (275 × 220 × 70 mm^3) was filled (h=65 mm) with the PVP phantom having the same electrical properties and was placed into the coil. 9 tubes (4 air and 5 PVP filled) were embedded into the phantom to generate contrast in the phantom for imaging purposes. The mock implant#1 was 177 mm immersed 30 mm under the phantom surface. The wire carrying the rectified tip diode signals was connected to the ADC of the pTx safety testbed system using a long coaxial wire and the filter plate.

The system's free induction decay (FID) sequence (RF pulses without gradients) was used to obtain $\boldsymbol{Q}_S^E$ pulses. $N^2 = 64$ pulses were transmitted using the MRI system's GUI. The rectangular envelope RF-pulses had 15 V peak voltage and 200 µs duration.

After $\boldsymbol{Q}_S^E$ acquisition using the MRI hardware, pTx excitation modes were calculated and transmitted to compare the imaging performance of four pTx excitations: WC, B_1-shim, OP, and NM modes. The purpose of the imaging experiment is to demonstrate a scenario where diagnostic information is desired near the implant. Therefore, a B_1^+-mapping sequence was utilized to acquire individual B_1^+ maps of the pTx channels. For B_1^+ mapping a 2D GRE (TR = 30 ms, TE = 3 ms, FOV 256 × 256 mm^2, in-plane resolution = 1 ×1 mm^{2}and slice thickness = 10 mm) was used. Using the acquired B_1^+ maps, the channel phases can be set for constructive interference of all B_1^+ fields at the center tube. This mode is henceforth referred to as the B_1-shim mode and is used as the reference transmission mode for imaging. Then, the OP mode is calculated from this reference transmission mode, this time, instead from the previously used CP mode. For all pTx imaging modes, a 2D GRE sequence (TR = 11 ms, TE = 4 ms, FOV = 300× 300 mm^2, in-plane resolution = 0.6 × 0.6 mm^2, slice thickness = 10 mm,

number of averages = 2) was acquired in coronal and axial directions. A total of 8 images were acquired and the scanner reported: $P_{forward}$ =24 ± 0.5 W. Finally, the E-field at the implant tip was measured for all pTx excitation modes using the same FID pulse and the Schottky diode.

4.3.2. Results

Implant safety testbed experiments at 297 MHz

$\boldsymbol{Q_S^E}$ acquisitions

The temporal resolution of the diode measurement is $4\ \mu s$ with a dynamic range of 1 V. The measurement precision is 126 µV for the $\boldsymbol{Q_S^E}$ experiments. The acquired $N^2 = 64$ measurements for $\boldsymbol{Q_S^E}$ and $\boldsymbol{Q_S^T}$ are shown in Figure 4.10A. For $\boldsymbol{Q_S^E}$ acquisition 20 out of 64 measurements were undetectable for this implant location due to low RF coupling for these particular transmission settings. The amplitude and phases of the calculated $\boldsymbol{Q_S^E}$ is shown in Figure 4.10B. RF coil channels #2 and #8 generate the maximum E-fields, which are spatially closer to the implant lead, while the channels #4 to #6 that are further away, generate neglectable induced E-fields at the implant tip.

$\boldsymbol{Q_S^T}$ acquisitions

The temperature increases and the induced sensor signal for individual pTx channel combinations is shown in Figure 4.10A. The thermistor's sensitivity is slightly better than the diode's in detecting small contributions from pTx channel combinations resulting in low RF-induced heating. The resulting $\boldsymbol{Q_S^T}$ based on the raw data from Figure 4.10A is shown in Figure 4.10C. As expected, the amplitudes and phases of $\boldsymbol{Q_S^T}$ are similar to $\boldsymbol{Q_S^E}$ (Figure 4.10B) with channel #2 and channel #8 having the largest contributions to RF induced tip heating. In $\boldsymbol{Q_S^T}$ acquisitions, 55 temperature rises were detectable out of 64 RF pulse transmissions. Hence, this may have created the small deviation when comparing $\boldsymbol{Q_S^E}$ and $\boldsymbol{Q_S^T}$ acquisitions.

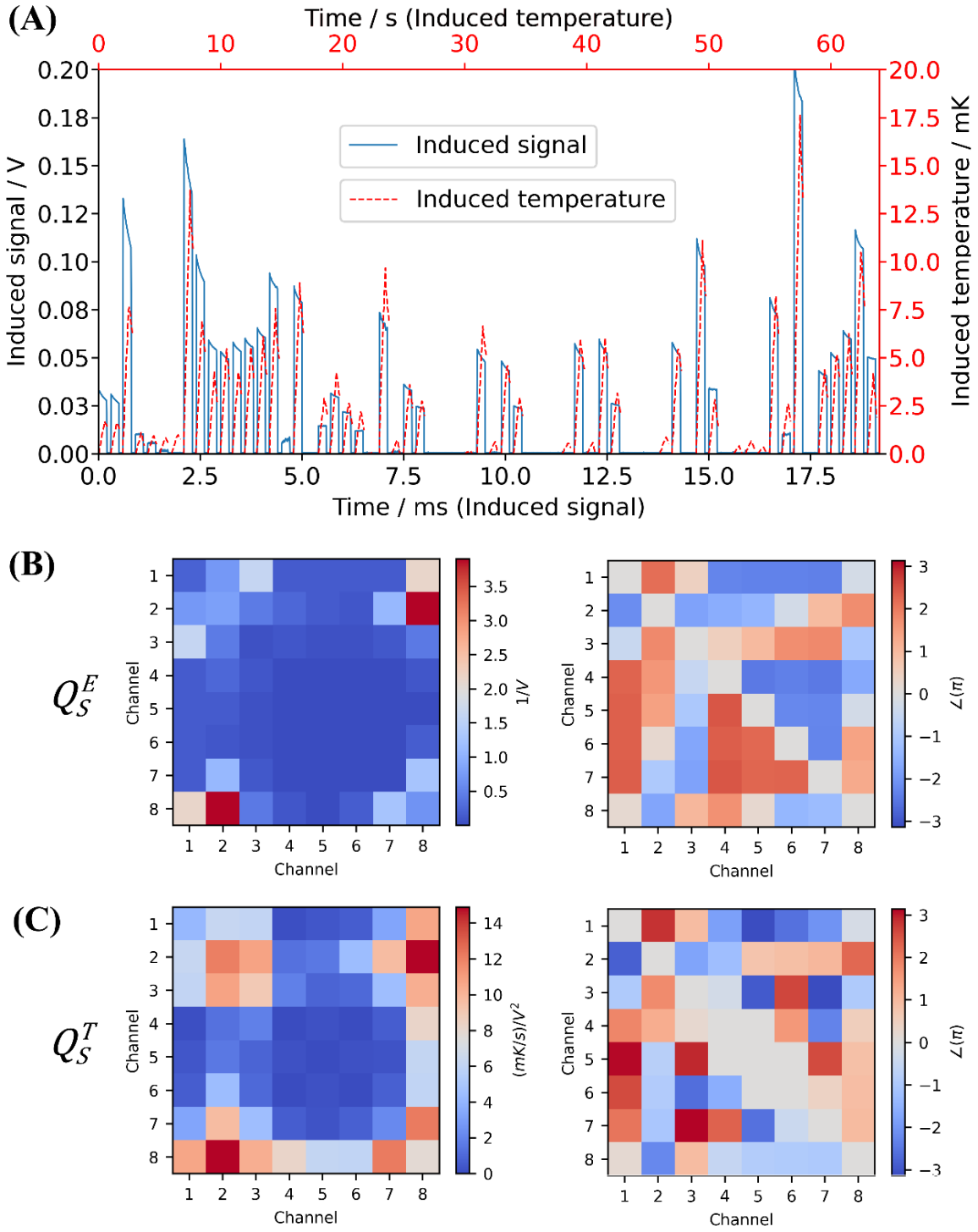

Figure 4.10 Results from a $\boldsymbol{Q_S}$ acquisition (64 RF pulses using an 8-channel RF coil) on implant #1 within the testbed at 297 MHz. A) Time courses of the diode-based measurements ($\boldsymbol{Q_S^E}$, solid blue line) and thermistor readings ($\boldsymbol{Q_S^T}$, dashed red line) for 0.5 s long pulses. Calculated amplitude and phase of (B) $\boldsymbol{Q_S^E}$ and (C) $\boldsymbol{Q_S^T}$. (Adapted from the Reference [64] CC BY 4.0, 2022, The linecolor and the axis of the temperature plot are changed to red).

The results of the repeatability experiments are shown in Figure 4.11. Maximum temperature rise was 82 ± 0.8 mK during $\boldsymbol{Q}_S^T$ acquisitions, which demonstrates that even for an 8-channel pTx setup, $\boldsymbol{Q}_S^T$ can be acquired using low powers that deliver neglectable RF-induced heating to the implant. Based on $\boldsymbol{Q}_S^T$ the calculated eigenvalues that are eventually used to determine the pTx excitation vector are shown in Figure 4.11A. The dominant eigenvalue has 73% weight for this $\boldsymbol{Q}_S^T$ acquisition with a standard deviation of only 2% over 10 repetitions. For the less dominant eigenvalues, which have a lower effect on RF-induced heating, the standard deviation increases slightly. The magnitudes and their standard deviations of the $\boldsymbol{Q}_S^T$ repetition experiments are shown in Figure 4.11B. The standard deviation is lower for the channels with higher magnitudes.

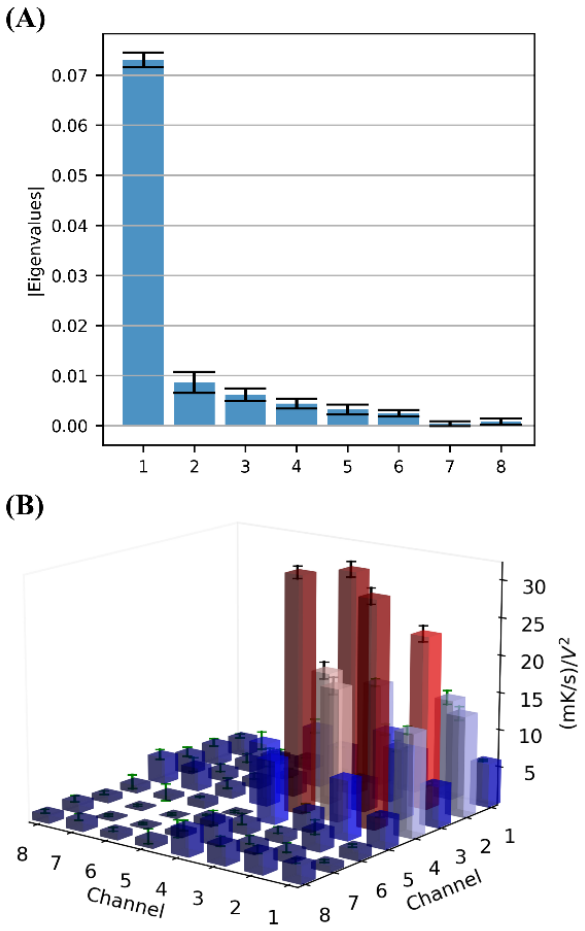

Figure 4.11 The repeatability analysis of $\boldsymbol{Q}_S^T$ using the embedded thermistor readings in the pTx safety testbed at 297 MHz A) Normalized eigenvalues including standard deviation of the 10 measured $\boldsymbol{Q}_S^T$ matrices. There is 2% deviation in the dominant eigenvalue #1 B) Magnitudes of the calculated $\boldsymbol{Q}_S^T$. including error bars for all $\boldsymbol{Q}_S^T$ elements indicating the standard deviations. (Reproduced from the Reference [64] CC BY 4.0, 2022).

RF-induced heating mitigation using $\boldsymbol{Q_S^E}$ and pTx

The results of the automated experiment using the pTx implant safety testbed and RMS sensor based $\boldsymbol{Q_S^E}$ method at 154 implant lead locations using mock implant #1 are shown in Figure 4.12. As expected, the CP mode has lower induced E-field values on the implant close to the phantom center and higher values in the periphery. Both OP and NM mitigation methods reduced the RF-induced signals on the implant at 99% of the investigated implant positions. As expected, the NM mode reduced RF-induced heating better than the OP mode at 62% of the investigated regions. The RF-induced sensor signals of the NM mode have 14% and 17% higher values, respectively, than the CP mode at two positions. The reduction factors are more than 12 times for OP and 32 times for the NM mode compared to the CP mode at x = 0, y = 0 position, where the CP mode has the maximum RF-induced signal. The OP maxima at the location x = 4, and y = 13 has four times lower RF-induced signal compared to the CP mode.

The simultaneous heating experiments demonstrate the correlation between heating rate (Figure 4.12B) and RF-induced signals (Figure 4.12A) at the tip. The induced peak voltage measured over the diode linearly correlates (Pearson coefficient: $r > 0.94$, $p < 0.001$) with the square root of the heating rate measured with the thermistor. For all three modes, the positions on the right area along the y-axis (between positions at 5.0-10.0 cm) demonstrate higher heating rates compared to RF-induced signals. This is probably due to non-homogeneous baseline temperature increases on the phantom during the time course of the RF-heating experiments. This baseline drift is also visible in the results of the individual time courses corresponding to Figure 4.12B, which are shown in Figure 4.13. The baseline temperature variations in the phantom add or subtract to the local temperature rises during RF-heating experiments. The maximum temperature rise of 20.5 mK in the location (x0, y0) is found in the CP mode. The proposed $\boldsymbol{Q_S}$ method to mitigate RF-induced heating reduced the temperature rise to 1.9 mK for the OP mode and 0.9 mK for the NM at this location.

Statistical analysis of the data is shown in Figure 4.14B demonstrating the CP mode has a median at 27.7 mV for the RF-induced voltages. The medians are

reduced to 0.63 mV and 0.56 mV for the OP and NM modes, respectively. The standard deviation for the OP method was 1.57 mV and it was 3.76 mV for the NM mode. The higher standard deviation in the NM can be attributed to the outliers, demonstrating that the OP mode is more robust against uncertainties in the measurements. It should be noted that only single NM with lowest eigenvalue was tested for this study. Other six NM vectors were not investigated.

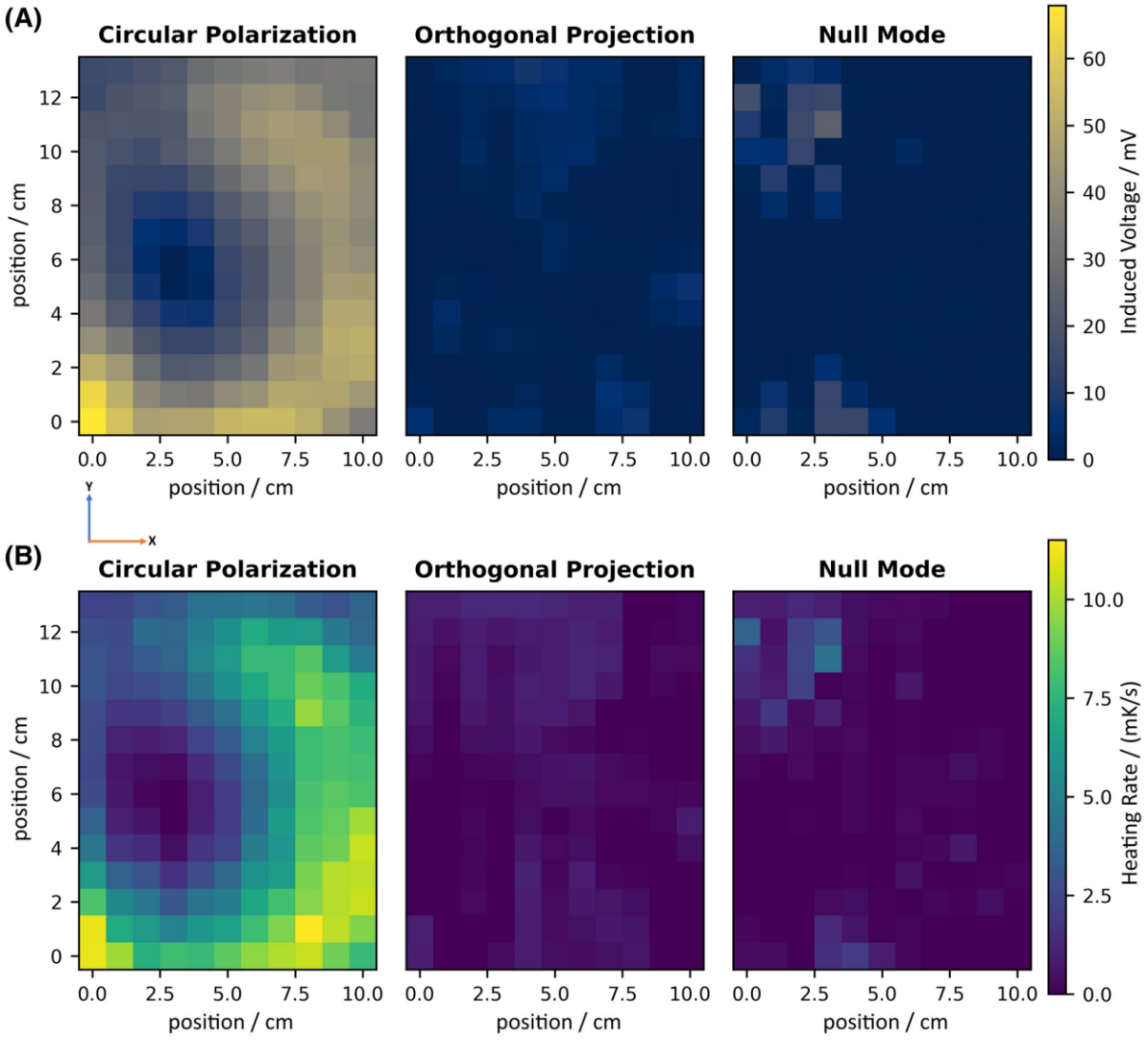

Figure 4.12 The results of the automated Q_S^E experiments in the pTx implant safety testbed at 297 MHz measuring at 154 implant locations within the phantom. A) The RF-induced voltage measurements by the RMS sensor from CP, OP and NM mode. B) Heating rate after applying 2 s long RF pulses for CP, OP and NM. OP and NM were calculated based on Q_S^E acquisitions. (Reproduced from the Reference [64] CC BY 4.0, 2022)

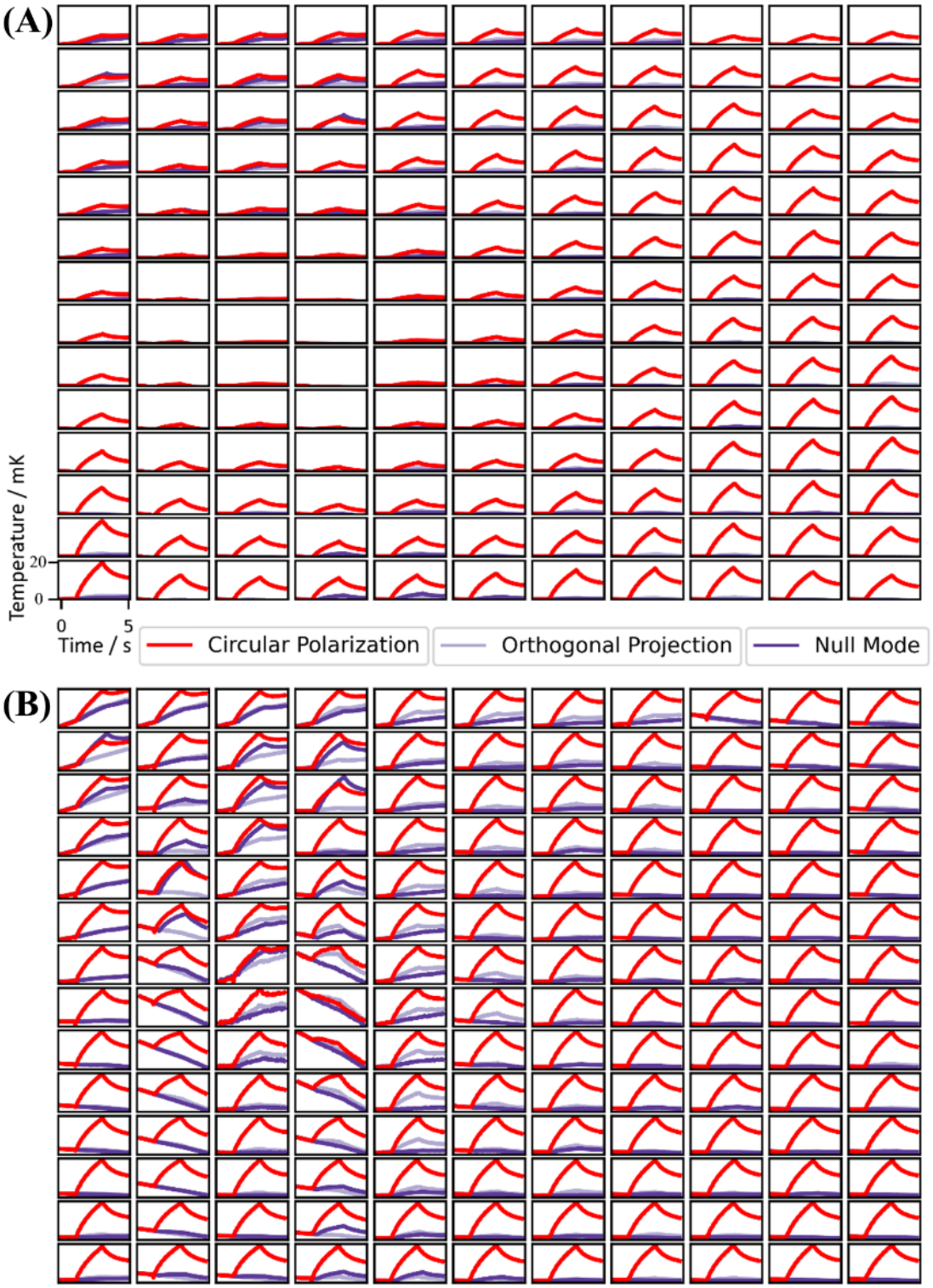

Figure 4.13 The raw data of the temperature profiles of CP, OP, and NM for pTx excitations from Figure 4.12B. Panel A) shows the temperature rises, where temperature axis is fixed to 0-20 mK for all measurement locations. B) The measured temperature rises displayed for the temperature axis normalized to its local maximum temperature value.

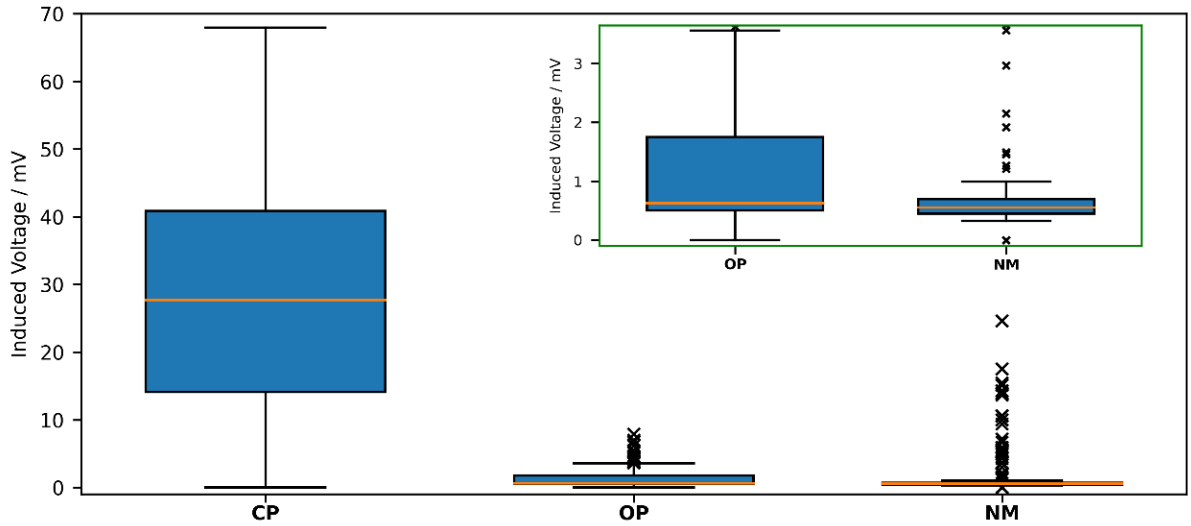

Figure 4.14 A) shows the RF-induced voltage ratios on the implant wire for different transmission modes. The induced voltage ratio is clamped to 2. Both methods (OP and NM) to reduce RF-induced signals on the implant wire were successful at 99% of the locations. (B) RF-induced voltages on the implant wire for the pTx excitation modes using box plots from Tukey's original definition.[161] The smaller plot depicts the median of the pTx mitigation methods OP and NM is close to zero. (Reproduced from the Reference [64] CC BY 4.0, 2022).

RF-induced heating mitigation using $\boldsymbol{Q}_S^T$ and pTx

The results comparing $\boldsymbol{Q}_S^T$-based mitigation to the $\boldsymbol{Q}_S^E$-based mitigation using the mock implant#1, where both diode and thermistor are embedded at the implant tip, are shown in Figure 4.15. The amplitudes of the $\boldsymbol{Q}_S^T$ and $\boldsymbol{Q}_S^E$ matrices are shown in Figure 4.15B and Figure 4.15E, respectively. Both methods indicate similar dominant channel contributions, but slightly differ in resolution. Fewer signals were detected using $\boldsymbol{Q}_S^E$ compared to measured temperatures with thermistor (cf. Figure 4.10A) for $\boldsymbol{Q}_S^T$. However, both methods highlight the dominant RF coil channels in terms of RF-induced heating on the implant. The role of the dominant channel sensitively depends on the implant location and can change even for small implant movements of only 20 mm (Figure 4.15).

The measured RF induced signals for the pTx modes calculated by $\boldsymbol{Q}_S^T$ acquisitions using the thermistor are shown in Figure 4.15C. Figure 4.15F shows the signals calculated based on $\boldsymbol{Q}_S^E$ using the diode. Both $\boldsymbol{Q}_S^T$ and $\boldsymbol{Q}_S^E$ methods can successfully predict the local maximum (WC) RF-induced signals. There are slight differences

in local absolute values comparing WC signals based on $\boldsymbol{Q_S^T}$ and $\boldsymbol{Q_S^E}$ calculations. Except for the bottom measurements, $\boldsymbol{Q_S^T}$ could calculate "better" WC RF-induced signals, which could be attributed to the more detectable $\boldsymbol{Q_S}$ elements during their acquisitions. Both pTx mitigation modes (OP and NM) based on the $\boldsymbol{Q_S^E}$ and $\boldsymbol{Q_S^T}$ methods are successful (compared to reference CP mode) in terms of the measured diode signals at all locations. For the OP method, there were no detectable RF-induced signals for $\boldsymbol{Q_S^T}$ and $\boldsymbol{Q_S^E}$ -based pTx mitigations, except for the top row of the $\boldsymbol{Q_S^E}$-based OP. For the NM, there were also no detectable diode signals while using $\boldsymbol{Q_S^E}$; and only small detectable signals while using $\boldsymbol{Q_S^T}$, especially at the second location from the top row.

The results of the temperature experiments are shown in Figure 4.15D and Figure 4.15G for the $\boldsymbol{Q_S^T}$ and $\boldsymbol{Q_S^E}$, respectively. For all measurements, the temperature rise correlates to the RF-induced signals (see Equation (2.6)), indicating that both RMS sensors can be used as RF safety detectors. The temperature rises for the WC and CP mode were significantly higher than OP and NM, except for $\boldsymbol{Q_S^T}$ based NM mode at the second location from the top. There were slight temperature increases for the $\boldsymbol{Q_S^E}$ -based OP mode (second, fourth, sixth locations from the top) even though there was no detected RF-induced signal by the diode. This might be occurred due to thresholding behavior of the diode or temperature increase related to the incident E-field at the tissue not due to the scattered E-fields at the implant tip.

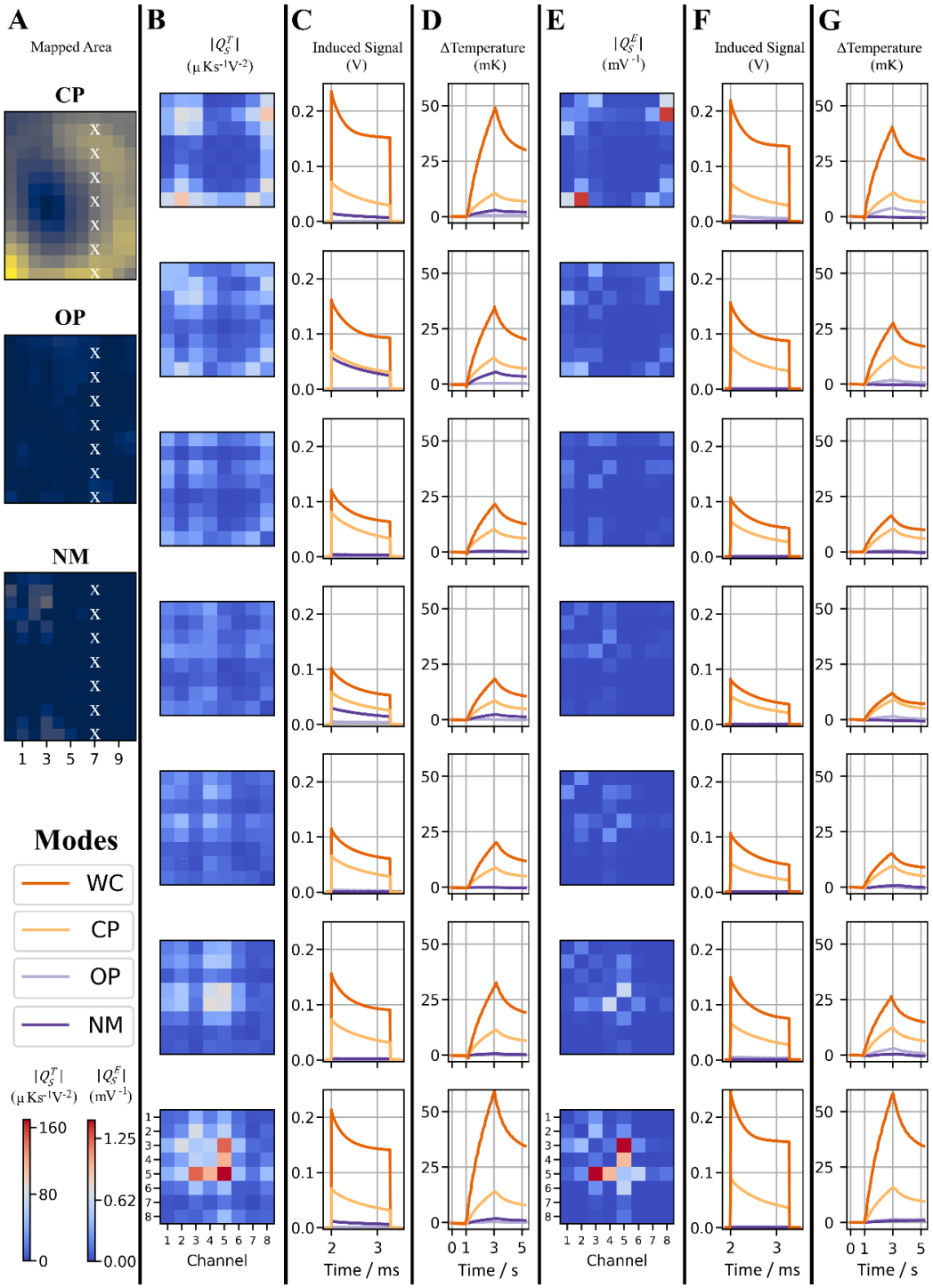

Figure 4.15 $\boldsymbol{Q_S}$ experiments performed at seven locations in the pTx implant safety testbed at 297 MHz using the mock implant #1 with both thermistor and diode at the implant tip. $\boldsymbol{Q_S^T}$ and $\boldsymbol{Q_S^E}$ -based pTx mitigations are compared. A) The selected implant locations are illustrated using white crosses. B) $\boldsymbol{Q_S^T}$-acquisition amplitudes and corresponding C) RF-induced signals and D) temperature measurements for WC, CP, OP and NM modes. E) $\boldsymbol{Q_S^E}$ acquisition amplitudes and F) corresponding RF-induced signals and G) temperatures for all transmission modes. (Reproduced from the Reference [64] CC BY 4.0, 2022).

MR Experiments at 3T

In the following sections, the results to assess and demonstrate $\boldsymbol{Q_S^T}$ and $\boldsymbol{Q_S^E}$ methods in the 3T MRI environment are presented.

$\boldsymbol{Q_S^T}$ and two-channel body birdcage coil

The temperature rises under nine different flip-angles (10-90°) using the GRE sequence are depicted in Figure 4.16A. The thermistor can precisely measure the RF-induced currents under MRI conditions. There are small fluctuations on the temperature measurements during the RF transmission. It is assumed that these fluctuations can be due to RF coupling to the wire or the repetition time of the RF pulses, which is hard to distinguish for this very low temperature increases. Nevertheless, the transmit RF power correlates with the temperature rise (Figure 4.16B) indicating that SAR can be extracted from the slope of the temperature rise using Equation (2.6).

Running the scanner's body coil in two channel mode as a dual-drive birdcage implies a 2 × 2 $\boldsymbol{Q_S^T}$ matrix. The corresponding temperature measurements for each matrix element are shown in Figure 4.16C. Using the acquired $\boldsymbol{Q_S^T}$, different heating rates for arbitrary pTx excitation modes can be predicted (Figure 4.16D). For another implant location, the 2-channel $\boldsymbol{Q_S^T}$ acquisition and the resulting predictions of the RF-induced implant heating are depicted in Figure 4.16E and F, respectively. The predicted temperature increases after 5 s of heating for these two modes were 2.4 mK and 0.8 mK whilst, the actual temperature rises were 2.9 mK and 1.0 mK, respectively.

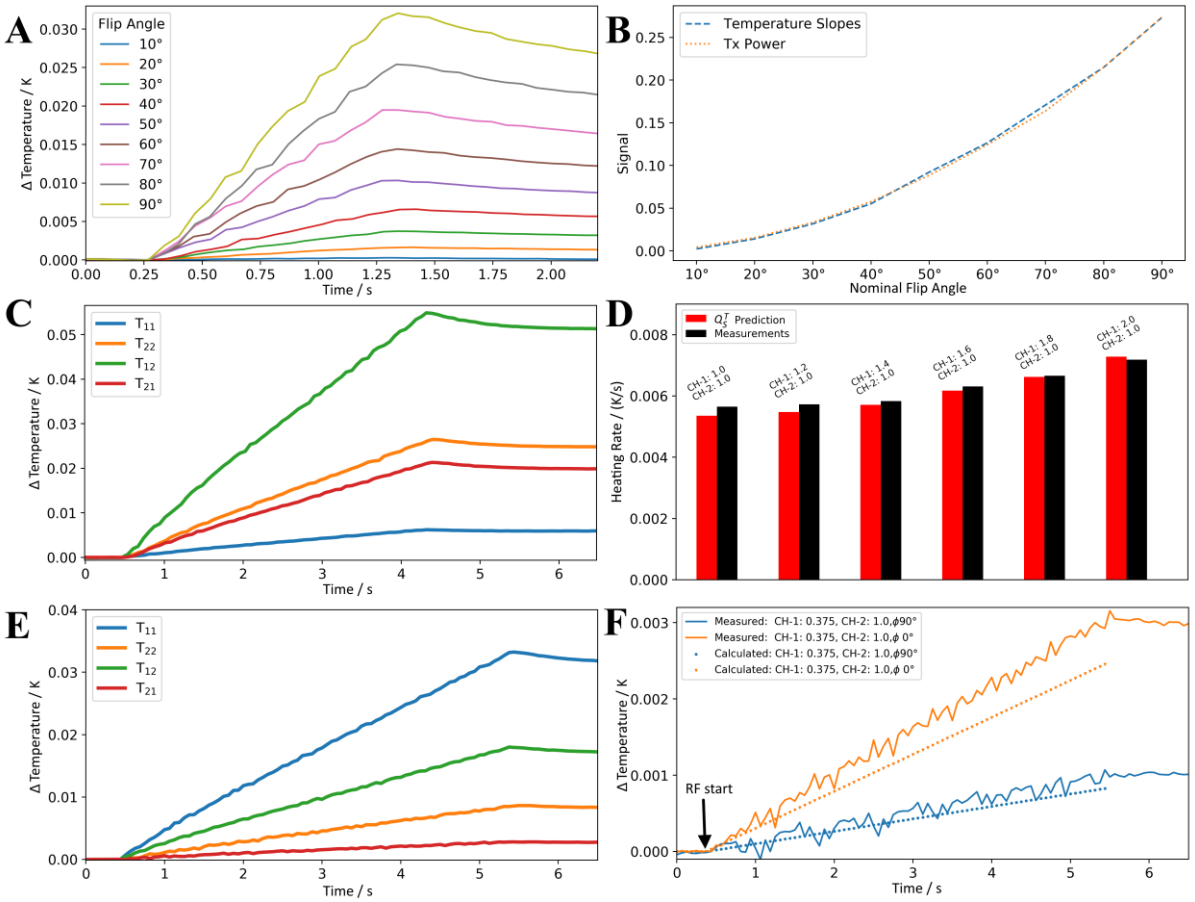

Figure 4.16 $\boldsymbol{Q_S^T}$ measurements inside a pTx capable 3T MRI using the system's 2-channel body birdcage RF coil for the prediction of RF-induced heating. A) Temperature rise calculated from the thermistor measurements versus nominal flip angle set by the scanner console. B) Measured transmitted power with the pick-up coil versus corresponding temperature slopes. C) $\boldsymbol{Q_S^T}$ raw data is displayed ($N^2 = 4$ temperature measurements; $N = 2$ for two-channel body birdcage coil). D) Various temperature rates acquired during MRI for arbitrary RF excitation voltages versus $\boldsymbol{Q_S^T}$-based temperature slopes. E) Another location's $\boldsymbol{Q_S^T}$ raw data and F) the respective temperature increases for two different complex-valued pTx RF excitation vectors in comparison to $\boldsymbol{Q_S^T}$-based predictions. $\boldsymbol{Q_S^T}$ acquisition can be performed at very low powers heating the implant tip by less than 0.1 K. (Reproduced from the Reference [64] CC BY 4.0, 2022).

Mitigation of RF-induced heating and imaging using $\boldsymbol{Q_S^E}$ and eight-channel pTx

The results for the $\boldsymbol{Q_S^E}$-based mitigation of RF-induced heating using an 8-channel pTx head coil in MRI are demonstrated in Figure 4.17. The coronal and axial images using different pTx excitation modes for the WC, B_1-shim, OP and NM are shown in panels Figure 4.17A to D and Figure 4.17E to H, respectively. The B_1-shim mode

is based on the acquired relative B_1^+-maps, which maximizes B_1^+ at the position indicated by the red cursor by setting the channel phases to constructively interfere. This mimics applications like single-voxel spectroscopy, where B_1^+ is optimized only for a small target volume.

SNR plots along the red dotted lines in Figure 4.17A and Figure 4.17E allow for a more quantitative assessment. The OP mode indicates similar imaging quality compared to the B_1-shim in the target region around the red cross (Figure 4.17B-C and F-G). In the vicinity of the implant lead, the B_1^+ imaging artifact is reduced as are the RF-induced currents on the wire for the OP mode. The NM mode also shows reduced B_1^+ imaging artifact around the wire; however, overall imaging quality is severely degraded.

For the RF heating part, the diode signals are plotted in Figure 4.17L. The WC mode generates substantial RF-induced signals on the wire with a value of 142.2 mV. The B_1-shim method indicates RF-induced signals with a value of 15.6 mV. The measured signals from the sensors embedded at the implant are substantially reduced at 5.9 mV and 0.9 mV, for NM and OP respectively. The dark spot at the tip of the implant (see coronal images) is a B_0 artifact created by ferromagnetic materials in the utilized RMS sensors. For real-life applications, completely non-magnetic sensors would be mandatory.

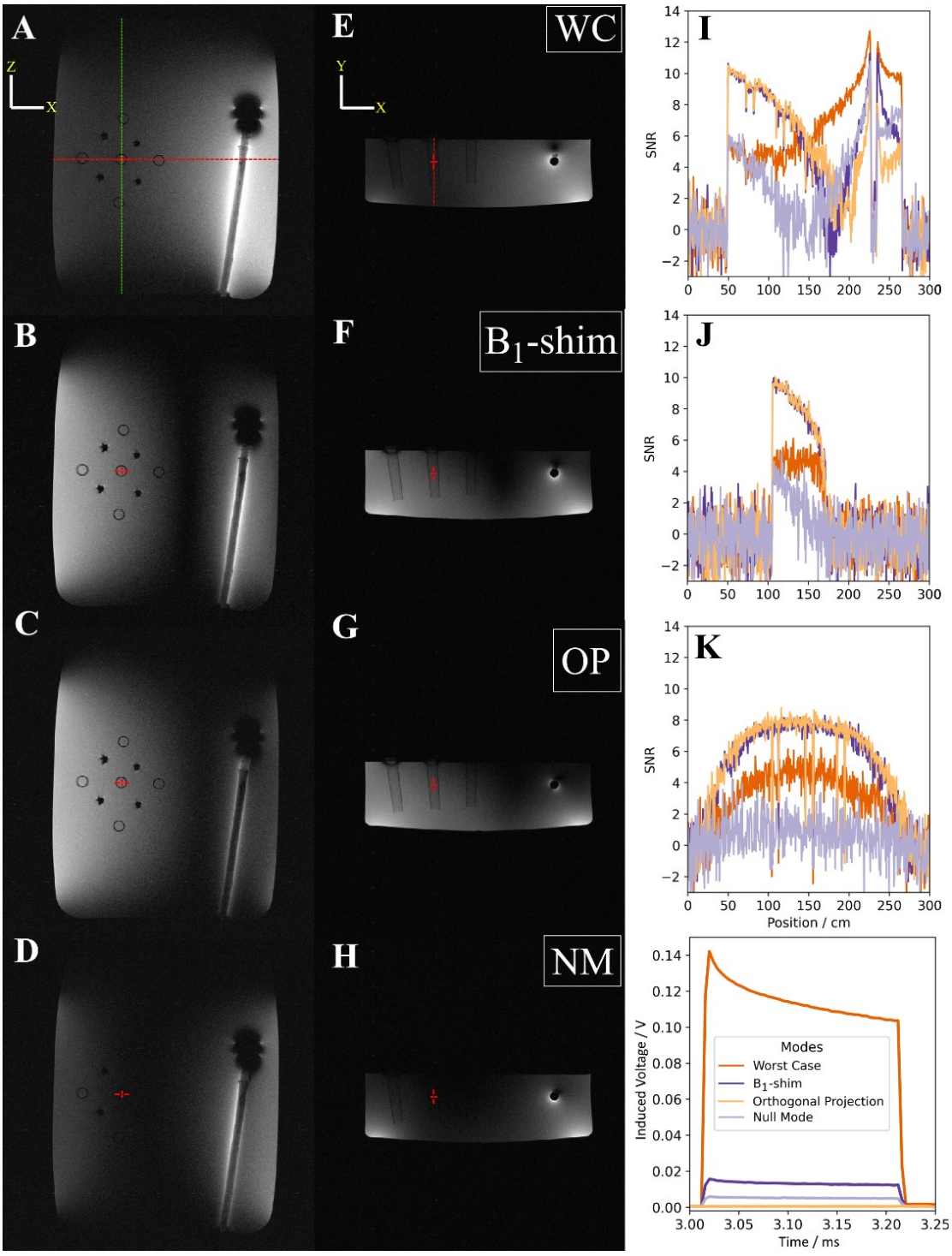

Figure 4.17 8-channel pTx MRI experiments at 3T for $\boldsymbol{Q_S^E}$ based pTx mitigation and imaging using WC, B_1-shim, OP and NM. The red cross indicates the target imaging location for the B_1-shim. Images are shown in (A-D) coronal and (E-H) axial view. SNR for all pTx excitations along (I) the x-axis (along red-dotted line in A) (J) y-axis (along red-dotted line in E) and (K) z-axis (along green dotted line in A). (L) Induced implant tip signals for all pTx modes. (Reproduced from the Reference [64] CC BY 4.0, 2022).

4.4. Discussion

The feasibility of using sensors together with a pTx system to mitigate RF-induced heating on implants was successfully demonstrated using both TD and RMS sensors. In addition, the orthogonal projection method was introduced as an easy means to find a pTx excitation vector for preserving B_1^+ in the pTx excitation vector that reduces implant heating.

4.4.1. The Orthogonal Projection method

The RF-induced signals can be effectively reduced by using the introduced OP method compared to an established reference excitation, typically the CP mode. This was demonstrated at a total of 364 implant locations by using both external TD E-field (Figure 4.4) and embedded RMS (Figure 4.12) sensors using the pTx implant safety testbed hardware at 297 megahertz. The implant imaging experiments at the 3T MR scanner also demonstrates that OP method can preserve the imaging information while reducing the RF-induced signals (Figure 4.7 and Figure 4.17).

The alternative NM method[61] was also successfully applied in all the aforementioned scenarios. The strength of the reduction was higher at 62% of the locations for the NM compared to the OP mode. Interestingly though, while the OP mode reduced heating for all locations compared to CP (Figure 4.12), for NM transmission two implant locations exhibited slightly (14% and 17%) higher RF-induced signals compared to CP mode. In their construction, the NM method is all about reducing the implant hazard, ignoring image quality, while the OP method aims at a certain compromise. The naive expectation would therefore be that NM excitation is always safer and the experiments show that this is mostly but not everywhere the case. It should be noted that only a single NM was used and a linear combination of several NMs might improve the pTx mitigation results.[61]

It was furthermore shown that, as naively expected, OP is more advantageous in preserving the imaging quality compared to NM (Figure 4.17). The OP method does not require any extra MR imaging such as B_1^+-mapping, which would increase the clinical examination times. Since only preliminary imaging results are presented,

further assessments on the imaging performance in a more realistic setting using complex implant lead trajectories is needed. This is demonstrated in the next chapter.

4.4.2. External time domain sensor-based mitigation of RF-induced heating

The feasibility of the real-time mitigation of RF-induced heating using time domain E-field sensors and the OP method was demonstrated at both 3T (Figure 4.7) and 7T frequencies (Figure 4.3 and Figure 4.4) using different RF coils and sensor locations (Figure 4.5).

TDS based E-field measurements and pTx mitigations can be acquired within approximately 10 ms for an 8-channel system allowing real-time capability (Figure 4.3). The real-time capability of the TDS is also practical for interventional applications, where instead of an E-field sensor, a current sensor can be used[61,72,73]. It should be also noted that safe low-power (1.4 W) acquisitions are sufficient to determine all relevant information for the mitigation scheme, e.g., using the OP method. Therefore, constant monitoring of the implant or guidewire status is feasible, as well as repetitive acquisitions to compensate different RF field alterations during patient breathing[70,71] or guidewire movements.[73]

A feedback mechanism can be established between the pTx system and the sensor for monitoring and mitigating RF-induced currents on the implants. This mechanism proved to be extremely useful to investigate a variety of different RF heating scenarios (i.e. RF safety watchdog[39]), which otherwise is only feasible in simulations. The reproducibility and positioning accuracies were essential in the experiments, as the measurement data shows moving the implant by only 5 mm results in more than 5 times higher measured E-fields (CP Figure 4.4). These results further highlight the importance of measurement-based methods over simulation-based safety assessment of implants, since small parameter changes might lead to drastic effects with respect to implant currents. For example, it has been also shown that the absorbed power around the same DBS electrode varied by 88% between five different simulated patient models.[58]

The time-domain E-field sensor's location on the implant can be critical to determine the absolute value of RF-induced E-field on the wire as shown in Figure 4.5. It should be added, that the E-field sensor orientation with respect to the implant wire was not perfectly perpendicular at various locations leading to deviations in the absolute measured results between two locations. This reason would also explain the discrepancy between the measured E-field magnitudes and the temperature rises for different implant locations (Figure 4.3). This problem can be improved by implementing probe holders that can precisely rotate or using smaller probes that can be directly embedded at the implant. The relative contributions between the different pTx transmission modes are, however, comparable.

For the AIMDs that are fully immersed into the body, implementing fast-switching readout circuitry with TDS probes might be challenging if not impossible. At least for the time being, smaller sensors and low-power solutions are the direction to go.

4.4.3. Embedded RMS sensor-based mitigation and Q_S

The embedded small footprint and cheap RMS sensors (e.g., a diode and/or a thermistor) offer a large spatial flexibility. Compared to a TD E-field probe having 4 × 4 mm^2 tip, the thermistor has a size of 1.6 × 0.8 mm^2. This allowed configuring various and multiple sensors that can be embedded at the implant tip. Implementation of such sensors should be feasible in commercial designs. For example, six temperature sensors were embedded at an RF ablation electrodes tip (2.5 mm diameter).[156,157]

The E-field based approach using $\boldsymbol{Q_S^E}$ and temperature-based approach $\boldsymbol{Q_S^T}$ were both successfully applied to significantly reduce RF-induced heating. $\boldsymbol{Q_S^E}$ has an advantage in terms of acquisition speed, which took about 20 ms for an 8-channel coil. The acquisition performance is comparable to the TD E-field probe as presented in the previous Section 4.4.3. The temperature-based $\boldsymbol{Q_S^T}$ acquisition needs around 1 minute for an eight-channel RF coil and 4 seconds for a two-channel body birdcage coil. The temperature detection speed was limited by the

sampling speed (40 ms) of the multimeter, which surely can be improved. However, its precision for resistance measurements and the thermal time constant of the NTC thermistor must be considered as well. In the end, $\boldsymbol{Q_S^T}$ acquisitions will remain to be orders of magnitude slower than $\boldsymbol{Q_S^E}$ acquisitions.[158]

For the $\boldsymbol{Q_S^E}$ method, the main limiting factor for the $\boldsymbol{Q_S^E}$ acquisition timing was the overshoot at the switching of the Schottky diode, which was not corrected at the testbed's ADC module for this study. In the presented $\boldsymbol{Q_S^E}$ experiments, the modulation frequency was 5 kHz (i.e., 200 µs long RF pulses). They were compared to dT/dt measurements, which agreed with the RF-induced signals (Figure 4.10). The ADC's impedance was adjusted to high-impedance mode and there was no matching circuit between receiver and Schottky diode. This caused an impedance mismatch and overshoots in the measured RF-induced signals. Further increments in the modulation frequency could have caused measurement hazards for this study. The modulation frequency can be increased by including the circuit model and a matching filter.[159,160] This issue is addressed in the next chapter.

Eventually, one acquired $\boldsymbol{Q_S}$ per exam and/or position for a patient can suffice to ensure RF safety of the implant as described in this chapter. In an event of a patient motion or interventional procedures, which change the RF field distribution, repeated $\boldsymbol{Q_S}$ acquisitions must be performed to reassure safety. The $\boldsymbol{Q_S^E}$ is best suited for these types of measurements because it is real-time capable. Even $\boldsymbol{Q_S^T}$ at 1-minute speed for 8-channel coil or a four seconds for 2-channel body birdcage coil can be faster than existing MR-based pTx mitigation methods.[51,57] Furthermore, it should also be considered that MR-based methods require additional pre-processing tasks such as determining the B_1^+ imaging artifact location that can be affected by image SNR, B_0 artifacts of metal or signal voids due to B_1^+ inhomogeneities. In contrast, sensors deliver direct information needed for RF safety assessment of AIMDs without MR related uncertainties.

The $\boldsymbol{Q_S^E}$ based information can be directly included within currently existing "native" pTx RF safety calculations without implants, e.g., Q matrices[111] and virtual observation points[161], and by using virtual human models.[66,67] An advantage of the $\boldsymbol{Q_S^T}$ method can be the direct measurement of the temperature at the implant tip,

which can be used for thermal dose calculations.[83–85] This would be a more direct method to prevent tissue damage from elevated temperatures and allow for less conservative RF limits than the current safety model based on SAR.[26,28]. A more practical approach can be a combination of fast $\boldsymbol{Q}_S^E$ acquisitions and resulting temperature monitoring to assess the thermal dose. It would be also advantageous using two independent sensors for more robust and failsafe safety mechanisms.

It should be stressed that the $\boldsymbol{Q}_S$ method directly measures and mitigates the RF-induced currents or temperatures on the implant in situ. The subject and exam-specific parameters including implant trajectory, and tissue properties around the implant are included in the acquired $\boldsymbol{Q}_S$. As shown in Figure 4.4, an error of 5 mm in implant location can drastically change the RF-induced E-fields. Existing simulation-based safety models need to account for these uncertainties in determining safe power limits, which ultimately, however, limits MR imaging performance.

Simulation-based safety models can be incorporated for further investigations of the $\boldsymbol{Q}_S$ accuracy as well because sensor signals measure the superposition of the background and scattered E-fields at their measurement location. The background E-field from the tissue (native) is expected to be significantly lower than the scattered E-field. Therefore, the sensors could be utilized for pTx mitigation as extensively demonstrated in this chapter. An example of the background E-field effect can be illustrated from the measured eigenvalue distribution in Figure 4.11. The embedded sensor measurements demonstrate the dominance of the scattered field; the other eigenvalues can be considered as the systematic imperfections (e.g., hardware) and the background E-field. Therefore, a more comprehensive safety concept including simulated native Q-matrices with $\boldsymbol{Q}_S$[162] could reveal more accurate results and can be investigated in the next steps.

The methodology for the implant model was simplified to mock implants, which is common practice for implant safety in MRI and provides realistic electromagnetic properties to test the methodologies developed in this work.[20,29,50,52,61,98,163,164] For realistic implants the question arises if the sensors presented here can be

embedded within the implant. In interventional devices, it is a common-practice to use integrated sensors.[156,165,166] For fully internal implants this is not yet the case but well imaginable for the future.

The B_0 artifact due to ferromagnetic materials in the RMS sensor's composition or implant manufacturing (e.g., solder metal) can easily be spotted in Figure 4.17A-D. The visualization of the implant tip was not considered an objective of the study. Other NTC types that create less severe B_0 artifacts can also be utilized in future studies.[120] It would be also possible that non-magnetic sensors similar to ceramic capacitors with non-magnetic components for RF coils may become available.

The sampling of the diode and thermistor signals was done in the pTx safety testbed by directly connecting the lead to its receiver channels. In a realistic scenario, wireless solutions[38,39,120] and a communication scheme are needed for more practical scenarios. This issue is addressed in the next chapter.

5. Wirelessly interfacing MRI with sensor-embedded implants

This part of the thesis demonstrates the translation of the presented sensor-based mitigation methods towards clinically more realistic settings for patients with a DBS implant in an MR scanner. Wireless reference implant hardware embedded with an RMS sensor and a communication workflow between the implant and an MRI scanner is presented. Material from this chapter was presented at several conferences and workshops [167], [168], [169], [170], and a manuscript for a journal publication was submitted to *Magnetic Resonance in Medicine*. The resources for hardware, firmware and software are published here: https://www.opensourceimaging.org/project/wireless-reference-implant/.

5.1. Introduction

So far, the $\boldsymbol{Q_S}$ method using small and cheap RMS sensors for pTx mitigation showed promising results. The proof of concept experiments were performed on long and mostly straight implant wires connected to external bulky receiver modules (see Figure 3.1, Figure 4.2 and Figure 4.9). In a realistic AIMD, the implant leads typically follow complex trajectories (Figure 5.1) and sensors and electronics are embedded in the AIMD casing, which is fully immersed in the body preventing a wired signal transfer. Therefore, a small sized receiver and a wireless module is required to convey the acquired sensor data outside of the body and to the MR scanner. A wireless communication between implant and scanner would also bring the possibility of improving the workflow of scanning patients with AIMDs.

Currently, an MRI examination of a patient with an *MR conditional* AIMD is possible by following lengthy guidelines by the manufacturers to fulfill the conditions under which the implant can be scanned.[30] These conditions are often associated with limitations in image quality, e.g. by imposing restrictive limits for the permissible whole-body SAR and/or $B_{1,RMS}^{+}$, while the MRI technologist or radiologist still have the sole responsibility in case of an accident.[171] This

procedure does always have the potential for errors that result in documented injuries.[17,18,23,172]

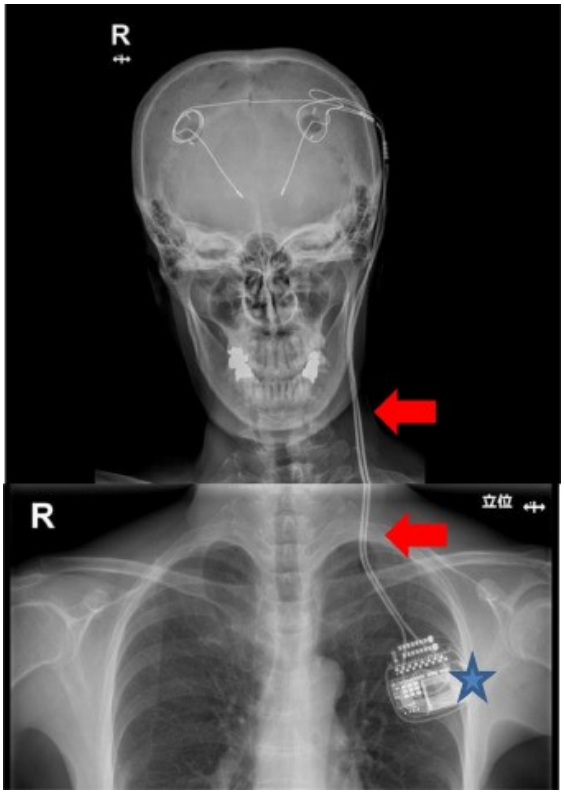

Figure 5.1 A radiograph of a patient with a DBS implant. The star annotates the metallic case containing the electronics and the battery. Arrows indicate the extension wire. The leads with uninsulated tip electrodes are implanted in the brain. (Reproduced from the Reference [173] CC BY-NC-ND 4.0, 2020)

A communication between AIMD and MR scanners and adjustments of safety related parameters, would greatly facilitate the clinical workflow, improve patient safety and imaging quality.

The communication can be realized by using wireless body area networks.[174,175] The 2.4 GHz network using Bluetooth Low Energy (BLE) protocol is already being implemented in newer implant generations.[176–178] Some studies also utilized BLE protocols to transfer real-time RF-induced heating from implants[38,120] and interventional devices.[39] Eventually, the presented RMS sensor and $\boldsymbol{Q}_S^E$ method for the pTx mitigation can be utilized for this purpose because:

1- The necessary information regarding RF-safety can be obtained by using kHz sampling rates instead of megahertz. This would relax the specifications for the ADC as well as processing power, memory, and telemetry.

2- As demonstrated in the chapter 4.3. RMS sensors are small footprint and cheap. Therefore, they can be placed at various locations in the implants, e.g., electrode tip or implant casing. For example, temperature sensors can be embedded in the electrode.[120,136,156,157,179]

To demonstrate feasibility of such methodology, a wireless reference implant with embedded sensors was developed. The implant has the capability of measuring RF-induced RMS E-fields from the tip by utilizing an internal E-field sensing circuitry built-in its electronic casing. Finally, the feasibility of the communication between implant and pTx testbed or MR scanner using $\boldsymbol{Q_S^E}$-based methods was demonstrated at both 297 MHz (7T) and 128 MHz (3T). The setup was tested in and outside the MR system in ASTM phantom experiments on realistic DBS lead trajectories.

5.2. Methods

5.2.1. Implant design

The absolute electromagnetic scattering from an AIMD depends on its materials, geometry, and surrounding medium. Design details of current AIMDs are proprietary and not normally openly available. Although the exact details of the sub-components of AIMDs vary depending on the application and manufacturer, AIMDs have a common structure. They have two main components:

1) A hermetically sealed metallic enclosure, implant casing, containing electrical components and a battery
2) A lead consisting of an electrode at its tip that delivers an electromagnetic pulse to the tissue or measures tissue specific parameters or local field potentials. Insulated electrical cables are utilized to carry the electromagnetic signals between electrode and implant casing with the lead.

The most commonly used AIMDs are cardiac pacemakers and neurostimulators. This chapter focuses on neurostimulators in particular on deep brain stimulator (DBS), since these represent the highest possible risk due their immediate contact

with brain tissue. Here, a DBS type of implant for RF safety testing of the sensor-embedded techniques is presented. The implant consists of an implant case that holds custom electronics circuit board connected to an antenna for wireless transmission, an extension wire, and a realistic lead trajectory with an uninsulated electrode at its tip.

Hardware

The electrical schematic and 3D model of the wireless reference implant are given in Figure 5.2 and Figure 5.3, respectively. The values of the electronic components are listed in Table 5-1. A battery (CP 1654A3, VARTA Microbattery, GmbH, Ellwangen, Germany) powered BLE v5.2 system on chip (SoC) (cc2652RB, Texas Instruments, Dallas, US) was used as the main processing unit. The chip was selected for its low power consumption enabling long battery life. In addition, most of the current DBS devices in the market already offer BLE wireless communication protocol for device programming.[180–183]

A battery protection module (AP9211SA, Diodes Incorporated, Plano, Texas, US) was connected to the battery. A module to sample RMS signals was constructed by using one channel of the 12-bit ADC of the SoC together with an RLC filter (L3, C4, R2) and a Schottky diode (D2) (MMDL101T1G, ON Semiconductor Corporation, Phoenix, US). The ADC allows a maximum 200 kHz sampling rate. For the experiments, 7.8 µs sampling rate with a 5.3 µs averaging time was employed.

Several components were utilized to protect the implant electronics from the high peak-power electromagnetic pulses transmitted from the MR system. First, a switch module was constructed to protect the implant when the device is not measuring, but the scanner is actively transmitting. For this module, a PIN (Positive-Intrinsic-Negative) diode (D1)-based (BA595, Infineon Technologies, Neubiberg, Germany) RF-switch module was constructed. The RF-switch is biased and supervised by the SoC for opening and closing the receiver line for measurements. A digitally controllable resistance, R1, and L1 serve as an RF-choke to reduce RF-induced voltages at the digital port. The bias of the D1 is shut-down except for the E-field measurements to protect the ADC during high-power MRI operations. L2 is the DC return path for the PIN diode bias. C1 and C3 serve as

DC-blocking capacitors for the tissue and the ADC measurements. An additional protection was employed by a Zener diode (D3) during transmission to prevent excessive peak voltages at the ADC. Finally, a microstrip high-pass filter[120] was used between the Bluetooth antenna port of the SoC and the connected external antenna (1003893FT-AA10L0025, AVX Corporation, South Carolina, US). This protection filter blocks the MRI frequencies in MHz regime and passes the signals in the GHz regime for Bluetooth transmission.

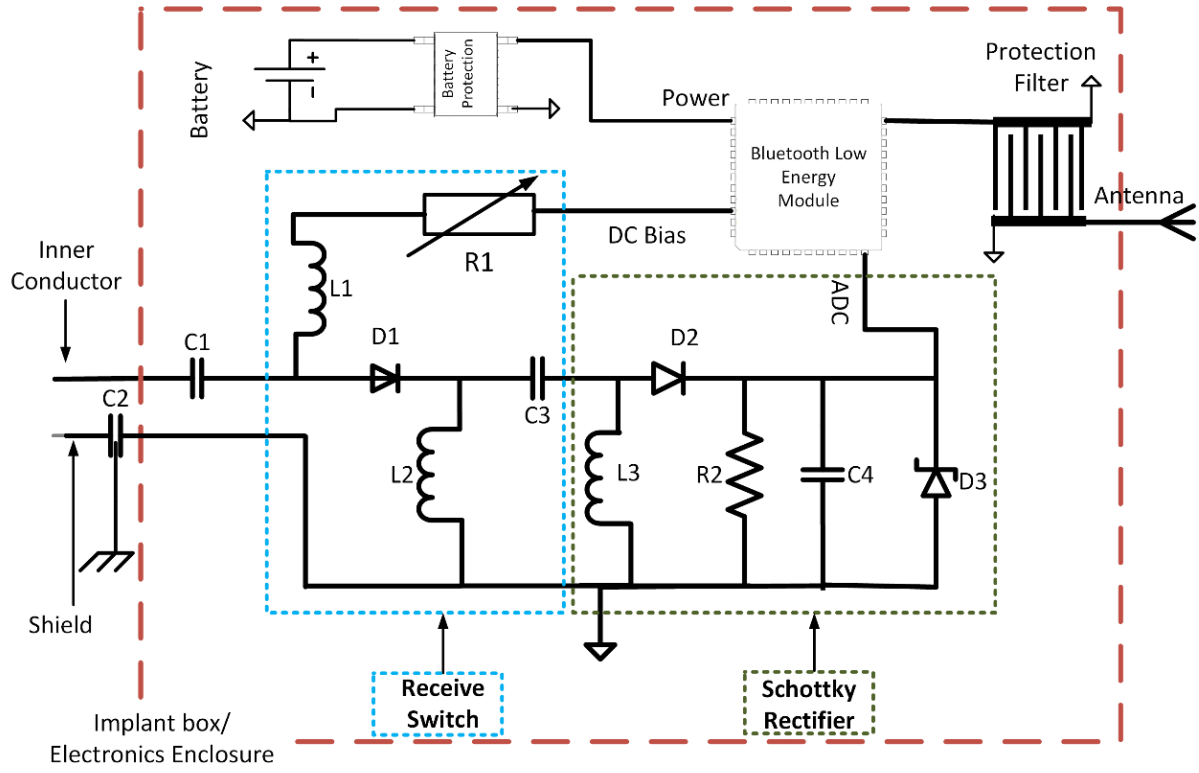

Figure 5.2 The electrical block diagram of the developed and constructed wireless reference implant. The values of the lumped components are given in Table 5-1.

The electronic circuit was enclosed in a metallic box (1455D601RD, Hammond Manufacturing, Guelph, Canada) as illustrated in Figure 5.3. A coaxial cable was used as an extension cable (see Figure 5.1) between the lead and implant case. The outer shield of the extension cable was interfaced with the case over the feedthrough capacitor, C2 (4300-013LF, CTS Corporation, Elkhart, IN, US), to eliminate coupled RF signals from the MRI to the outer shield that could corrupt measured RMS E-field signals from the AIMD lead tip. The 2.4 GHz Bluetooth antenna is connected to the SoC and elongated to the outside of the electronics

enclosure. Copper tape was used to increase the protection from electromagnetic interference from the RF-coil. Finally, the lids of the electronic enclosure are hermetically sealed by using glue.

Table 5-1 The values of the lumped electrical elements in the reference implant (Figure 5.2).

	C1	C2	C3	C4	L1	L2	L3	R1	R2
Value	15	27	220	1	4.7	330	330	var.	4.3
Unit	pF	nF	nF	nF	µH	µH	µH	Ω	kΩ
Type	-	-	-	-	-	-	-	-	-

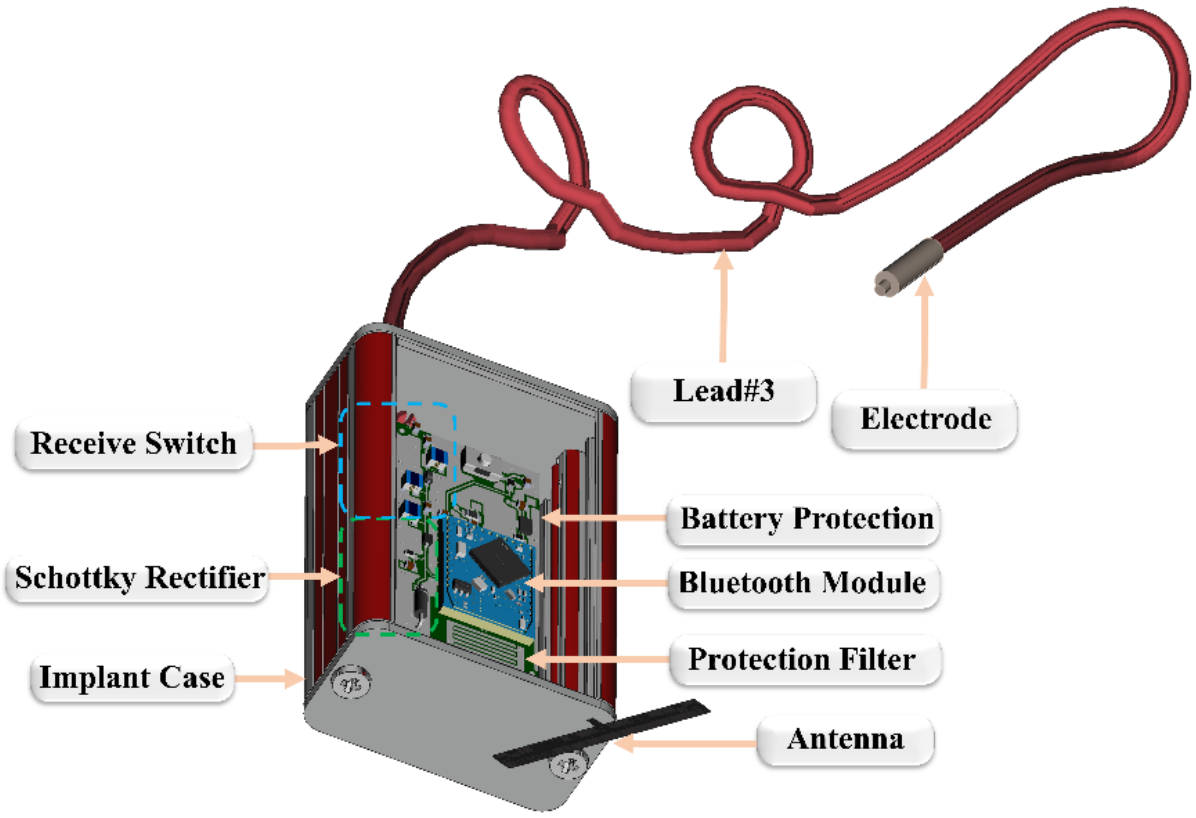

Figure 5.3 Annotated 3D illustration of the implant casing, the developed electronics PCB, and an example implant lead with an uninsulated tip.

Firmware

The firmware of the implant is customized for the experiments by modifying the stock program using its integrated development environment in C++ programming language.[184,185] The firmware has all BLE core requirements[186]. To be able to transfer the wireless $\boldsymbol{Q_S^E}$ data, the maximum transmission unit size is set to 251 packets and the physical link layer is adjusted to 2 Mbps. In addition, the connection interval is set to 7.5 ms without any slave latency between master and slave. These settings provide the maximum throughput to send the measured $\boldsymbol{Q_S}$ data.

Software

A software with a GUI was implemented in Phyton. This software allows communication with the reference implant. The software sends and receives commands from another BLE v5 capable transceiver (cc2640R2 Launchpad, Texas Instruments, Texas, US) via USB/UART interface, which is connected to a computer. The received raw $\boldsymbol{Q_S^E}$ data are processed in the software. RF-induced pulses are detected with a thresholding algorithm. Then, the pulses are extracted and sorted by using a comparator. Finally, the software outputs $\boldsymbol{Q_S^E}$ and pTx pulses for the RF mitigation settings.

Non-linearity correction

A Schottky diode has a non-linear response, which needs to be corrected to improve accuracy of the $\boldsymbol{Q_S^E}$ acquisitions and pTx mitigation schemes. For this purpose, the acquisition circuit was simulated using LtSpice (Analog Devices, Norwood, Massachusetts, US) with a sinusoidal signal at 128 MHz at the input. The amplitude was swept from 1 µV to 2.2 V in 1 µV steps and the voltage at the cathode of the Schottky diode was recorded as a response. The generated calibration curve was saved and used to correct measured signals with expected induced input signals. To validate the model, experimental data were acquired with the MR system by sweeping RF pulse amplitudes and recording induced sensor signals (not shown here).

Implant leads with realistic DBS lead trajectories

Six open-source lead trajectory models extracted from patient data[68,187] were converted to a 3D printable CAD model and printed with a 3D printer (S5, Ultimaker BV, Utrecht, Netherlands). Afterwards, these printed models were used to shape an uninsulated semi-rigid coaxial wire (diameter = 2 mm, El Spec group, 14940, Munich, Germany) into the trajectory shape. The wires were insulated by using heat-shrink tubing. 15 mm of the insulation was removed from the tip of the cables. In addition, the inner conductor extends 3 mm further than the outer conductor at the implant tip to increase the sensitivity of the E-field measurements for lower peak power transmissions (Figure 5.4). The other end of the cable was soldered to a SMA connector, which facilitates connection to the implant casing. The 3D printed models and the implemented lead trajectories are shown in Figure 5.5.

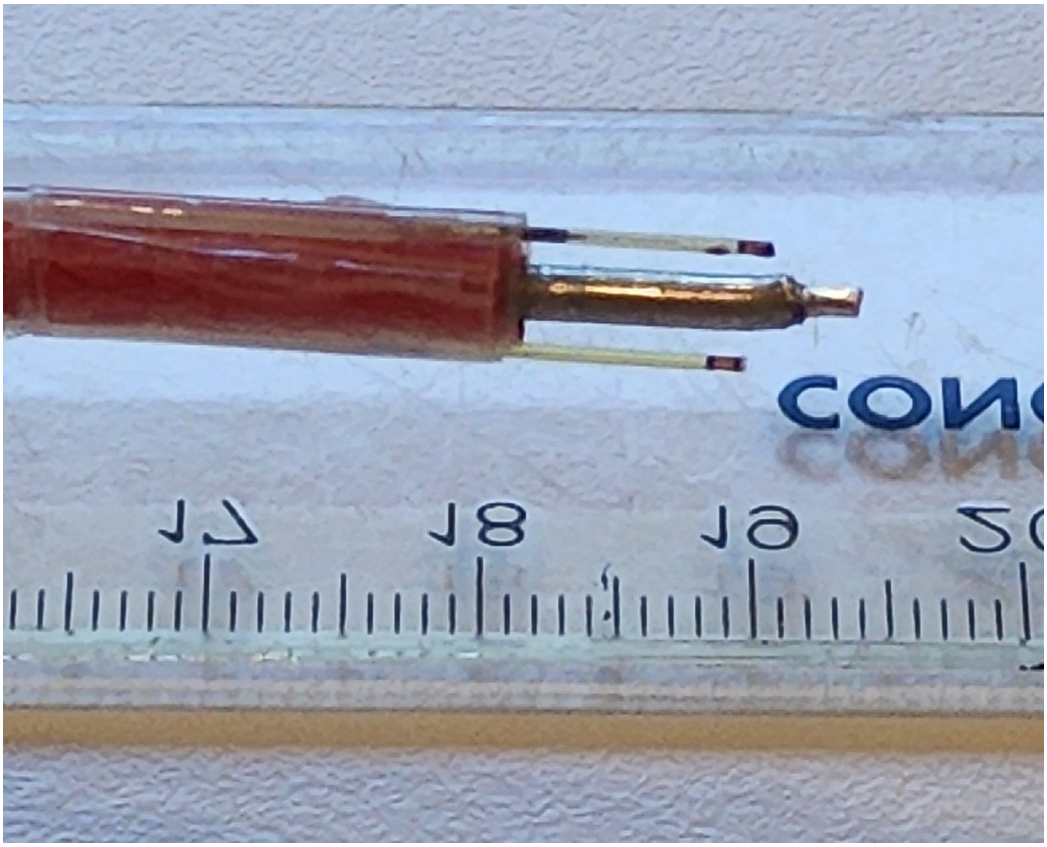

Figure 5.4 Photograph of the uninsulated implant tip with two fiber-optic temperature probes (~1 mm apart along the lead direction) attached to the lead.

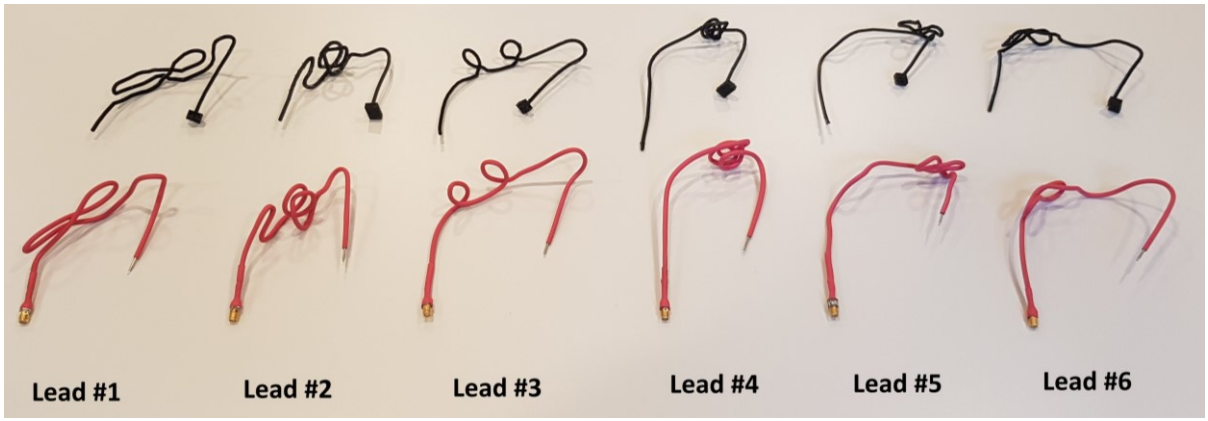

Figure 5.5 Constructed implant leads mimicking realistic implant lead trajectories from patients with DBS implants.[68] On top, the 3D printed models are shown in black. The bottom series is constructed by using a red semi-flexible coaxial wire with a 2 mm thickness that is shaped around the models.

Wireless communication workflow

A wireless communication workflow has been developed enabling the communication between implant and an MRI system (Figure 5.6). The reference implant and the BLE server establish a connection before any RF transmission. The connection parameters and the implant power settings are initially set before getting any RF trigger from the transmitter. Afterwards, the BLE server waits for the RF trigger from the pTx console, which is a software trigger in the testbed experiments and a standard wired trigger during the MRI experiments. When the subsequent RF pulsetrain is sent by the pTx console and the detected RF-induced power is measured by the sensors embedded in the implant, the data are wirelessly transmitted to the pTx console. The pTx console either computes pTx mitigation settings by using the $\boldsymbol{Q_S^E}$ method or reports the amount of the RF-induced signal on the implant tip.

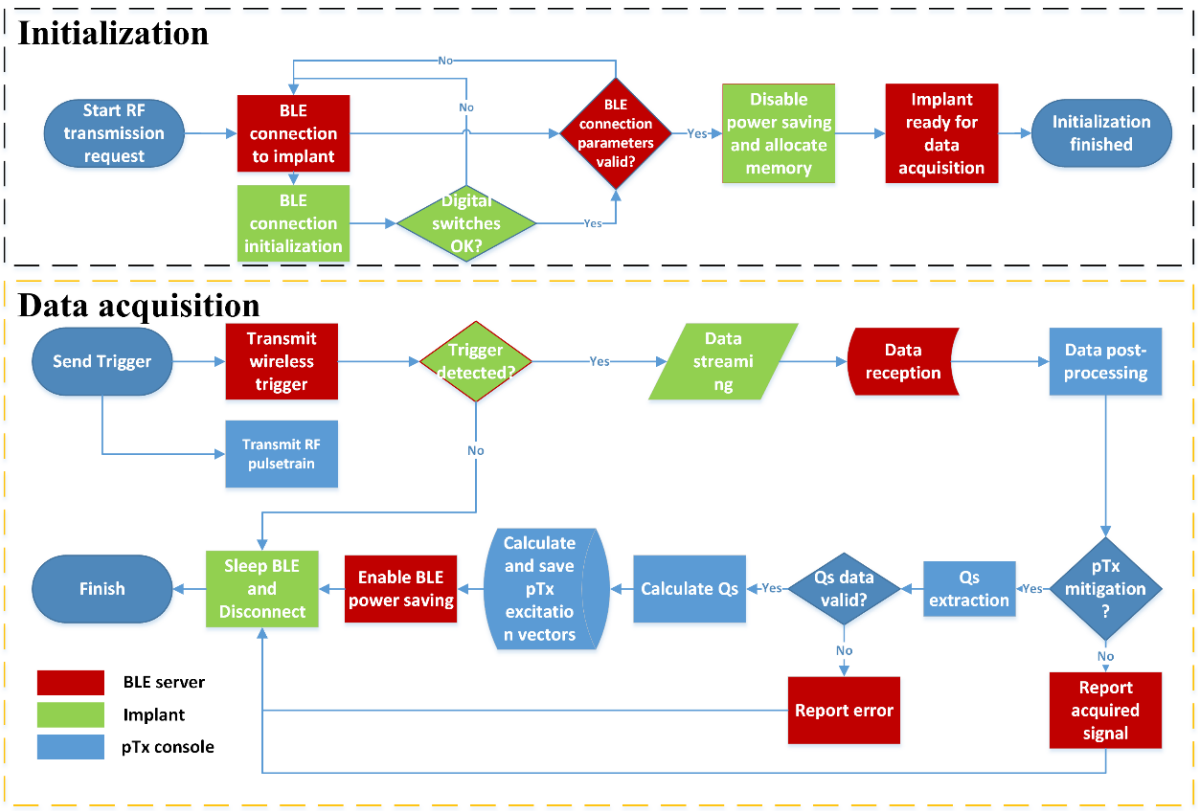

Figure 5.6 The wireless communication workflow for the AIMD interface with the pTx console is shown. In the initialization phase (black dashed line), the communication parameters are set and in the acquisition phase, (green dashed line) the data is acquired, transmitted, and processed.

5.2.2. Testbed experiments

The demonstrated 8-channel pTx implant safety testbed with a 297 MHz transmission frequency used for the initial experiments.[63,134] All constructed implant firmware, software and communication workflow was first implemented using the testbed system without tedious MRI experiments. Most importantly, testbed experiments were performed to show that the RMS sensor measurements by using the constructed wireless reference implant can pick-up the relevant E-field component from the implant tip. The constructed implant used for the experiments is shown in Figure 5.7.

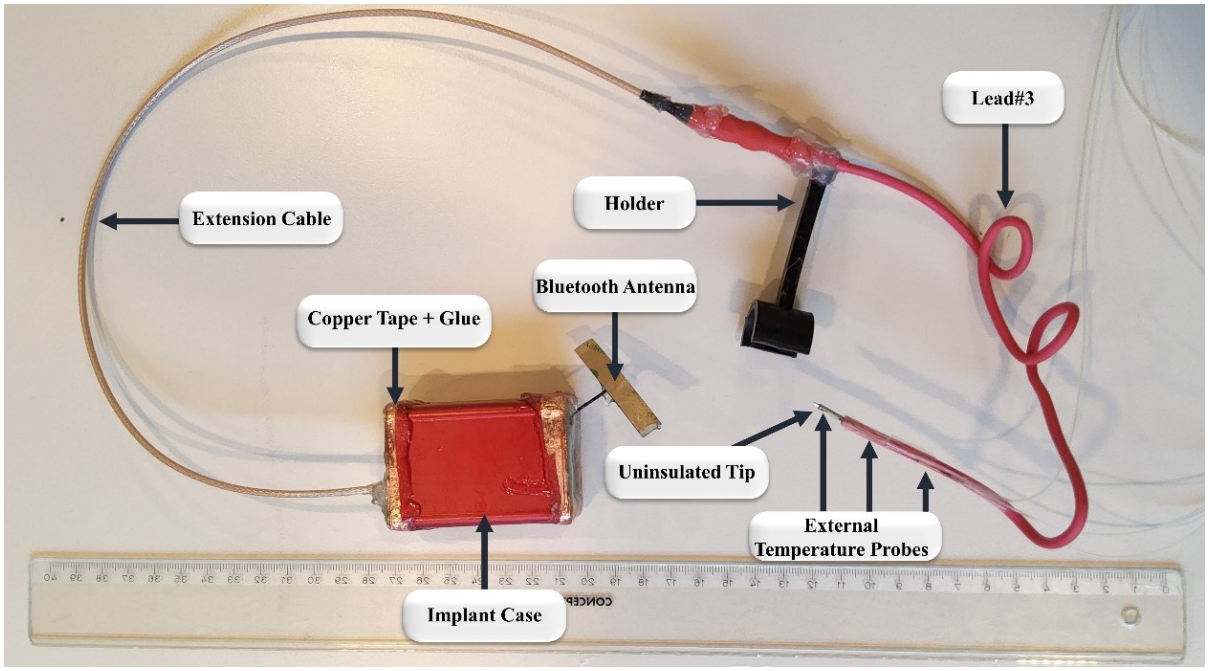

Figure 5.7 The constructed implant connected to the implant Lead#3 with an extension wire is shown. The extension wire and the lead are interfaced with an SMA connector, which is insulated. The holder glued to the implant lead is for the placement inside the ASTM phantom. The temperature rise at the uninsulated tip of the lead is measured with external fiber Bragg grating temperature probes.

The implant together with the testbed experimental setup is shown in Figure 5.8A. The implant lead was fully immersed into the phantom. The immersion depth of the uninsulated part of the lead was 15 mm below the liquid's surface. A time domain (TD) E-field probe (E1TDSz SNI Speag, Zurich, Switzerland) was placed at the uninsulated part of the implant lead tip to measure the radial E-field components (Figure 5.8B). Temperature rises were measured by using an external fiber-optic temperature probe (CANSAS FBG-T8, Imc Test Measurement GmbH, Berlin, Germany). Compared to previously available fiber optic sensor used in the chapter 3.2.4. fiber Bragg grating (FBG) temperature sensors utilizes the temperature dependent relative shift in the Bragg wavelength instead of fluorescence decay time used in the previous temperature sensor. Currently, FBG sensors provide higher temperature resolution and precision.

A total of 1000 random pTx excitation vectors (100 µs duration per each pTx excitation vector, 100% duty cycle) were sent in 4 segments (250 excitation vectors per pulse sequence). The implant and the E-field probe simultaneously recorded RF-induced signals. Then, twenty-four pTx excitation vectors, covering

the available range of RF-induced voltages, were selected for subsequent RF heating experiments to demonstrate that the sensor measurements placed in the implant electronic box are correlated to the tip temperature rise. Each RF heating experiment took one-minute per selected pTx excitation vector.

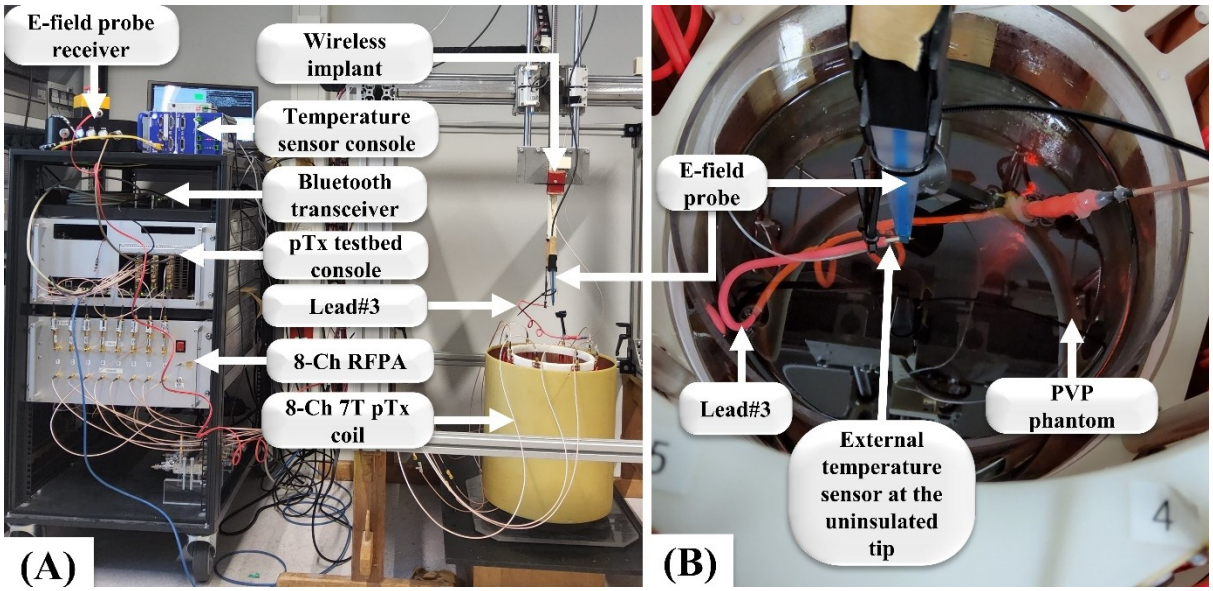

Figure 5.8 Experimental setup to compare the induced RMS signal with measured E-fields at the implant tip. A) pTx safety testbed experiments at 297 MHz using an 8-channel pTx RF coil. The implant case is mechanically fixed to the probe holder of the testbed. The extension wire connected to Lead#3 elongated through the probe holder and the tip of the lead fixed to the radial time-domain E-field probe for the reference measurements. External temperature probes are also attached to the tip of the implant lead. B) A close-up photo with the reference probes before Lead#3 is completely immersed into the phantom.

Finally, the correlations of the measured data (implant sensor versus TD E-field sensor, implant sensor versus temperature rise, TD E-field sensor versus temperature rise) were analyzed by using the squared value of the Pearson correlation coefficient (R^2) to the linear model without intercept value.

5.2.3. MRI experiments

Experimental setup

MRI experiments have been performed at the same 3T 8-channel pTx capable scanner (4.2.1. ,pg. 70). A phantom container based on the ASTM standard was used for the experiments.[26] The container was filled with a PVP solution ($\varepsilon_r = 50, \sigma = 0.33$ S/m). The electronic box of the implant was fixed by a 3D printed

holder and the prepared 6 realistic lead trajectories were fixed to the head part with another holder. A 50 cm coaxial wire as an extension was used to connect the implant leads and the implant casing. The photograph of the experimental setup with Lead#3 is shown in Figure 5.9.

The head section of the phantom is inserted into the 3T 8-channel pTx RF coil. The RF coil was connected to the RF amplifiers of the scanner. Then, the trigger cable of the MRI system was extended into the scanner room by penetrating the Faraday cage and connected to the BLE server. Finally, the BLE server's USB/UART interface was connected to an external laptop computer.

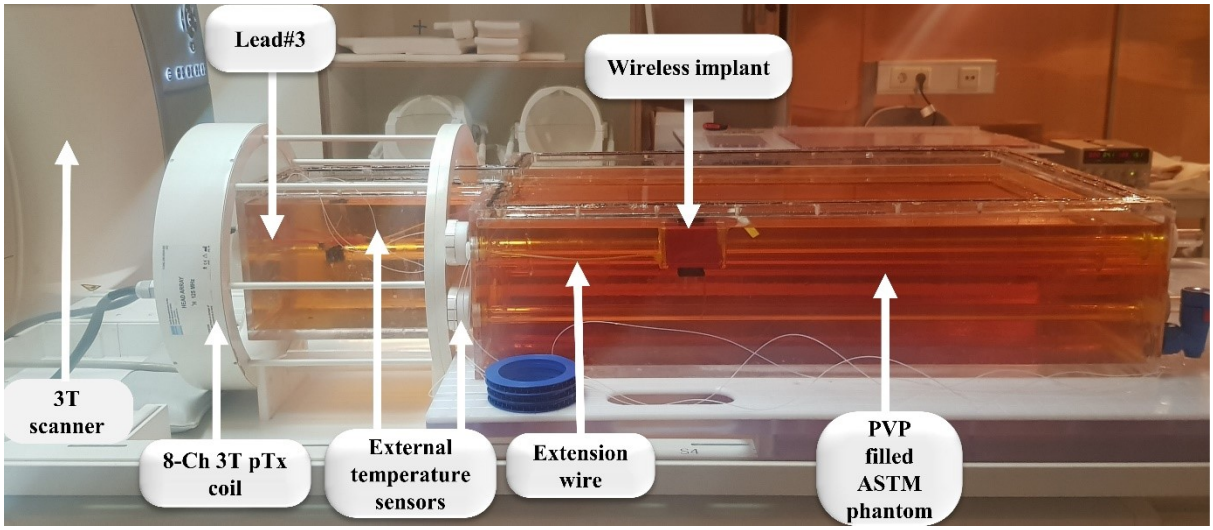

Figure 5.9 The MRI experimental setup is shown. Wireless reference implant inside the ASTM phantom in a 3T pTx capable MRI using an 8-channel 3T pTx RF coil. The sensor measurements in the implant were wirelessly triggered by the MRI system and transferred to an external laptop computer.

An RF-only FID pulse sequence was modified such that the latency between the RF-pulse and the trigger signal is 100 ms. This latency was needed for the internal processing time of the SoC of the implant. The amplitude and phase of the RF pulses for $\boldsymbol{Q_S^E}$ were adjusted from the text files that are stored in the pTx computer of the MRI scanner (i.e., Step 1 software). The possible step size of the pulses is 10 µs and the maximum RF-pulse length is 7.8 ms long for this particular MRI scanner. Consequently, the duration of the RF pulses to measure $\boldsymbol{Q_S^E}$ was adjusted to 60 µs followed by 50 µs idle time, which sums up to a total of approximately 7.5 ms for an 8-channel RF coil (8 × 8 acquisitions, 50 $V_{effective}$). The same sequence

was used for the assessment of the RF-induced signal on the implant for different pTx excitations (i.e., WC, CP, OP and NM). The amplitudes and phases of the pTx pulses were directly adjusted using the MRI pTx console's GUI.

BLE timing uncertainty and repeatability

As BLE is a discrete communication scheme, master and slave devices maintain the connection within a limited time. Then, they reestablish the connection after a pre-determined time, which is called a connection time interval.[186] The minimum connection time interval is 7.5 ms, which was used in all experiments. However, this creates a 7.5 ms deadtime between two devices meaning that an RF-trigger may fall within this timeframe. In addition, there is a probability of having undetectable RF-induced signals on the implant for some channel combinations during a $\boldsymbol{Q_S^E}$ acquisition, e.g., if one or two RF channels of the coil show only small coupling with the implant. Therefore, four additional RF pulses (forward and reverse circularly polarized) were inserted at the start and the end of the $\boldsymbol{Q_S^E}$ pulsetrain. These pulses were used to detect the start of the RF pulse to mitigate the timing uncertainty of the BLE communication. This method was investigated in an MRI setting using 10-consecutive $\boldsymbol{Q_S^E}$ acquisitions.

RF Heating experiments

RF-heating experiments were performed for all implant lead trajectories by using the same external fiber optic temperature probes as a reference measure of RF-induced heating for the different pTx excitation scenarios. The same FID sequence (TR = 200 ms) was adjusted to a total time of 67 s. The total 10 s averaged forward transmit power reported by the scanner was 22 ± 0.5 W and was the same for all pTx excitation settings (WC, CP, OP, and NM). Please note that RF coil losses are substantial and were not considered here. For a single implant lead (Lead#3) trajectory, RF-heating was performed additionally for 400 s to investigate temperature increase and mitigation performance after a longer period of time.

Imaging evaluation of wireless sensor-based pTx modes for mitigation

To evaluate the imaging performance of the different excitation vectors using the complex implant lead geometries, a GRE imaging technique was used for the imaging (TR = 221 ms, TE = 2.41 ms, Resolution = 1.0 × 1.0 × 5.0 mm^3, Phase resolution 512 and 100%, interleaved slice acquisition, gradient bandwidth = 980 Hz/Px, 2 averages). The total transmitted forward power for the GRE sequence reported by the scanner was 3.75 ± 0.5 W for all pTx excitation vectors.

5.3. Results

5.3.1. Testbed experiments

Wirelessly transmitted RMS sensor measurements from the implant compared to TD E-field sensor is shown in Figure 5.10. Please note that the designed circuit at the receiver of the implant box (Figure 5.2) demonstrates no overshoots observed during the $\boldsymbol{Q_S^E}$ acquisitions in the previous chapter (Figure 4.10). Furthermore, the implant sensor signal shows a good correlation with both the TD E-field probe (R^2 = 0.929) and temperature measurements (R^2 = 0.954). In the regime of lower induced E-fields (<100 V/m) for induced voltages of less than 0.08 V, the implant's sensor shows higher measured signal variations compared to the TD E-field probe. On the other hand, the TD E-field probe starts to saturate after 300 V/m whereas, the implant sensor is still accurate and sensitive at that region. This can be observed from the temperature experiments with deviations of the fiber optic temperature readings and the TD E-field probe above ~300 V/m (Figure 5.11B).

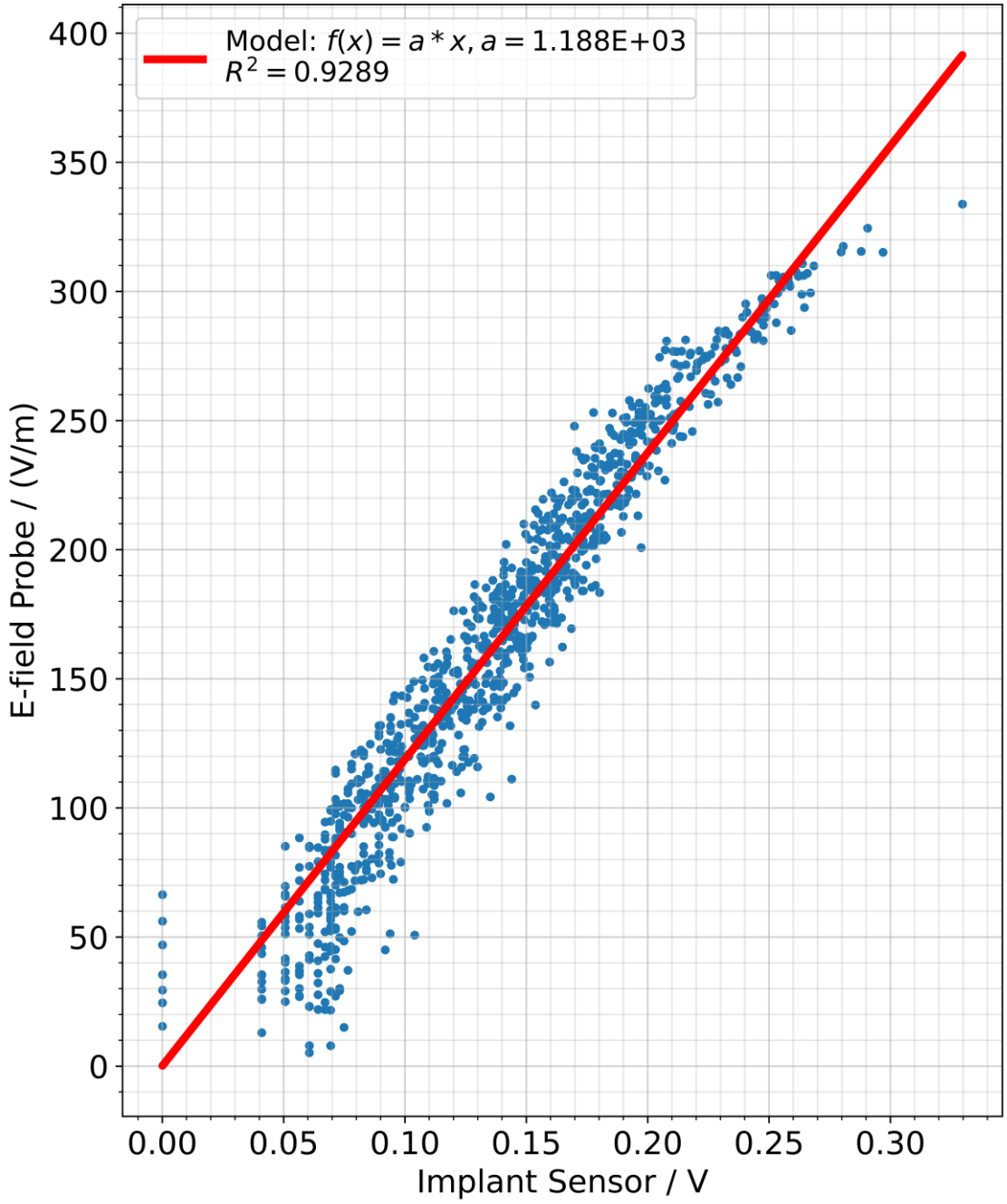

Figure 5.10 The comparison of TDS E-field probe readings at the implant tip and the wireless reference implant readings using the RMS sensor in the casing. Implant's sensitivity is lower for RF-induced voltages less than 0.08 V. TD E-field probe measurements saturate above 300 V/m

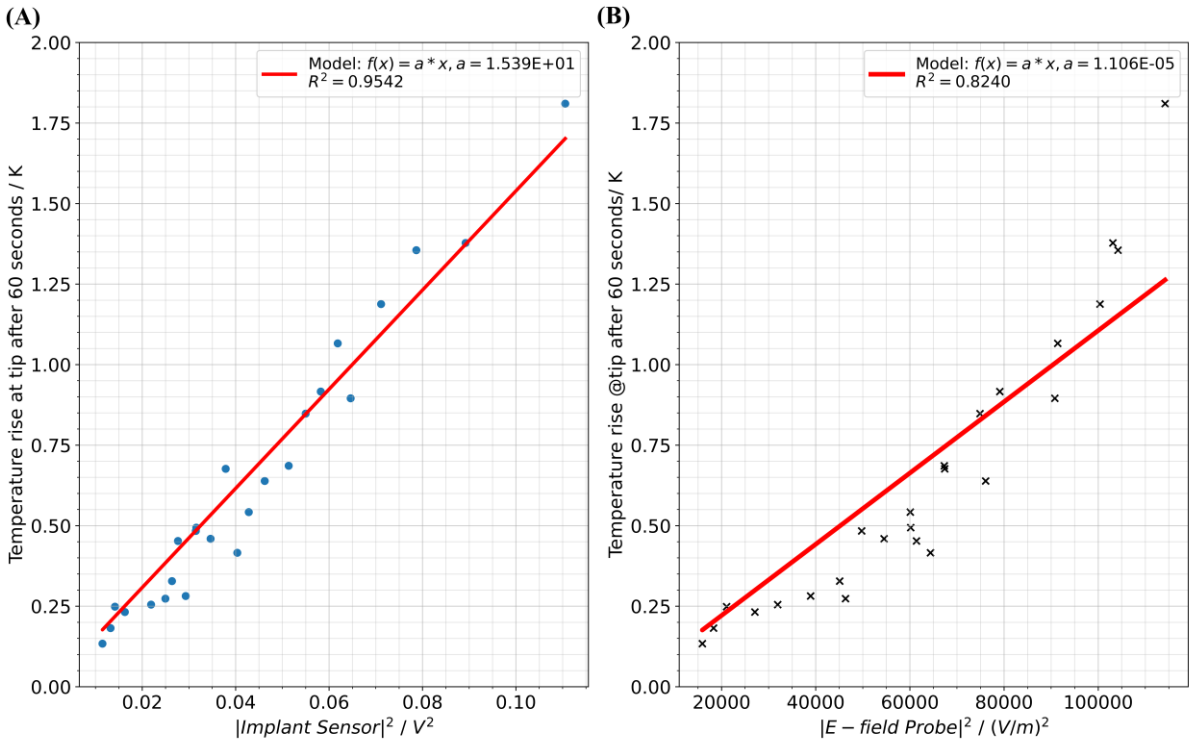

Figure 5.11 RF heating experiments for 24 selected pulses from Figure 5.10. A) Implant sensor readings and B) TD E-field probe readings versus fiber-optic temperature probe measurements.

5.3.2. Wireless Q_S acquisition

In Figure 5.12A the wirelessly transmit $\boldsymbol{Q_S^E}$ acquisition from within the MRI scanner is displayed for ten repeated measurements. The received raw $\boldsymbol{Q_S^E}$ data falls within a time interval of 15 ms with 7.5 ms being the total lengths of the RF pulse train used for the $\boldsymbol{Q_S^E}$ acquisition. An additional 7.5 ms occurred due to the dead time between connection intervals of the wireless acquisitions. The same ten consecutive $\boldsymbol{Q_S^E}$ acquisitions are shown in Figure 5.12B, where the timing of the pulses is synchronized using the first and last two RF pulses from the pulse train. With the synchronization applied, the calculated amplitudes (Figure 5.12C) and phases (Figure 5.12D) for all ten acquisition show standard deviations of less than 1%, which corresponds to precisions of mV in normalized amplitudes and milliradian in phases.

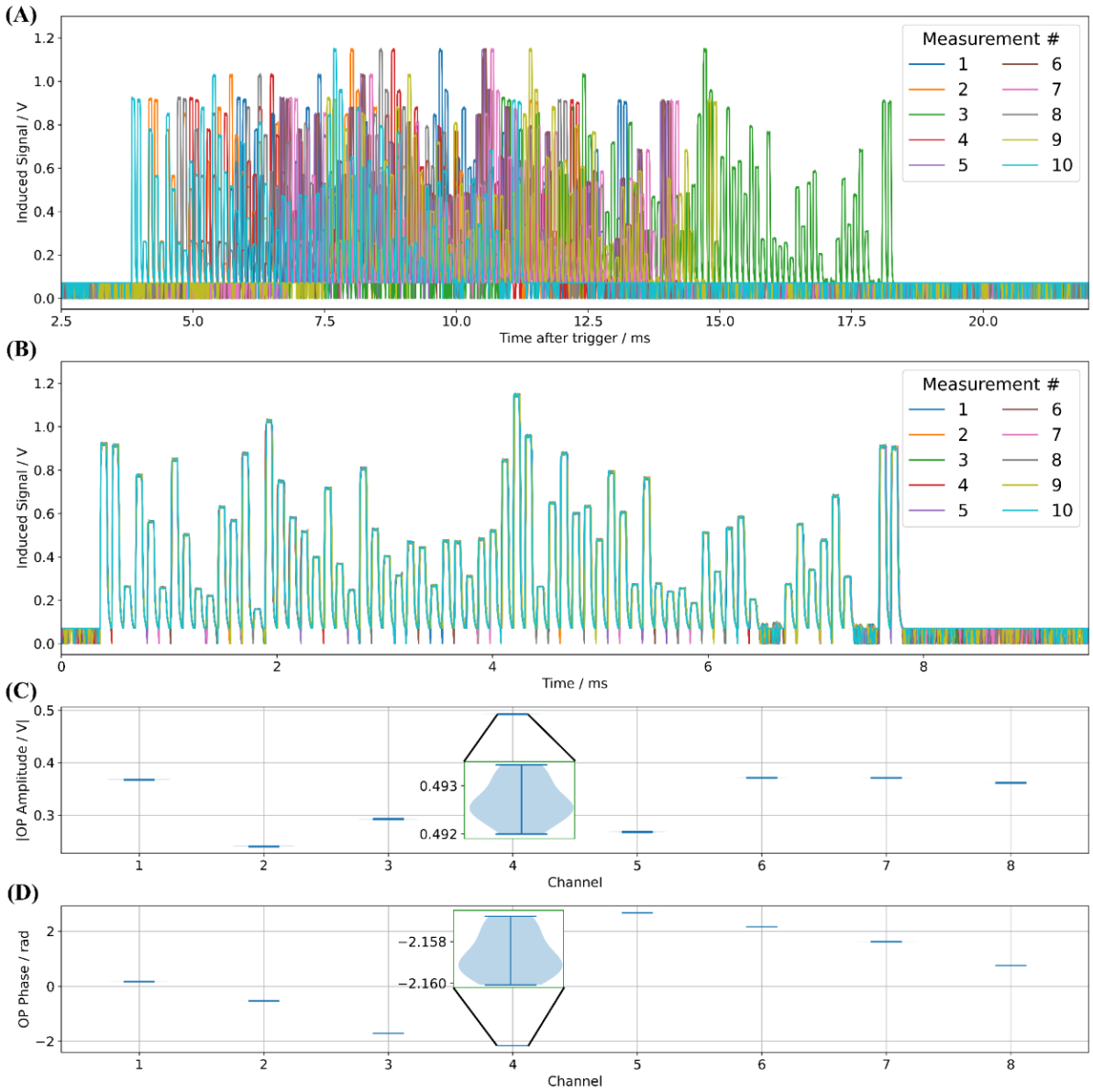

Figure 5.12 Timing synchronization of the wirelessly triggered $\boldsymbol{Q_S^E}$ acquisition and transmission. A) Measured $\boldsymbol{Q_S^E}$ raw data for 10-consecutive 7.5 ms long RF transmissions including timing uncertainties of the BLE timing interval of 7.5 ms. B) Corrected $\boldsymbol{Q_S^E}$ acquisitions. The first and last two RF pulse acquisitions are used as timestamps for the synchronization. The resulting amplitude C) and phase D) of the OP mode, is shown in a violin plot.[188] Since the standard deviation in the wirelessly acquired OP was less than 1%, channel #4 amplitude and phases are enlarged in (C) and (D).

The input power transmitted by the MR system vs the measured sensor signal in the reference implant is shown in Figure 5.13. The simulated non-linearity correction works as expected showing good linearity ($R^2 \geq 0.99$ for all eight channels) over the investigated range. Similar to testbed experiments, the implant cannot measure the voltages less than 0.08 V due to ADC sensitivity limits. On the

other hand, the measurements start to saturate after 1.6 V (cf. Figure 5.13: Channel-6) which is close to the maximum electrical limits of the SoC.

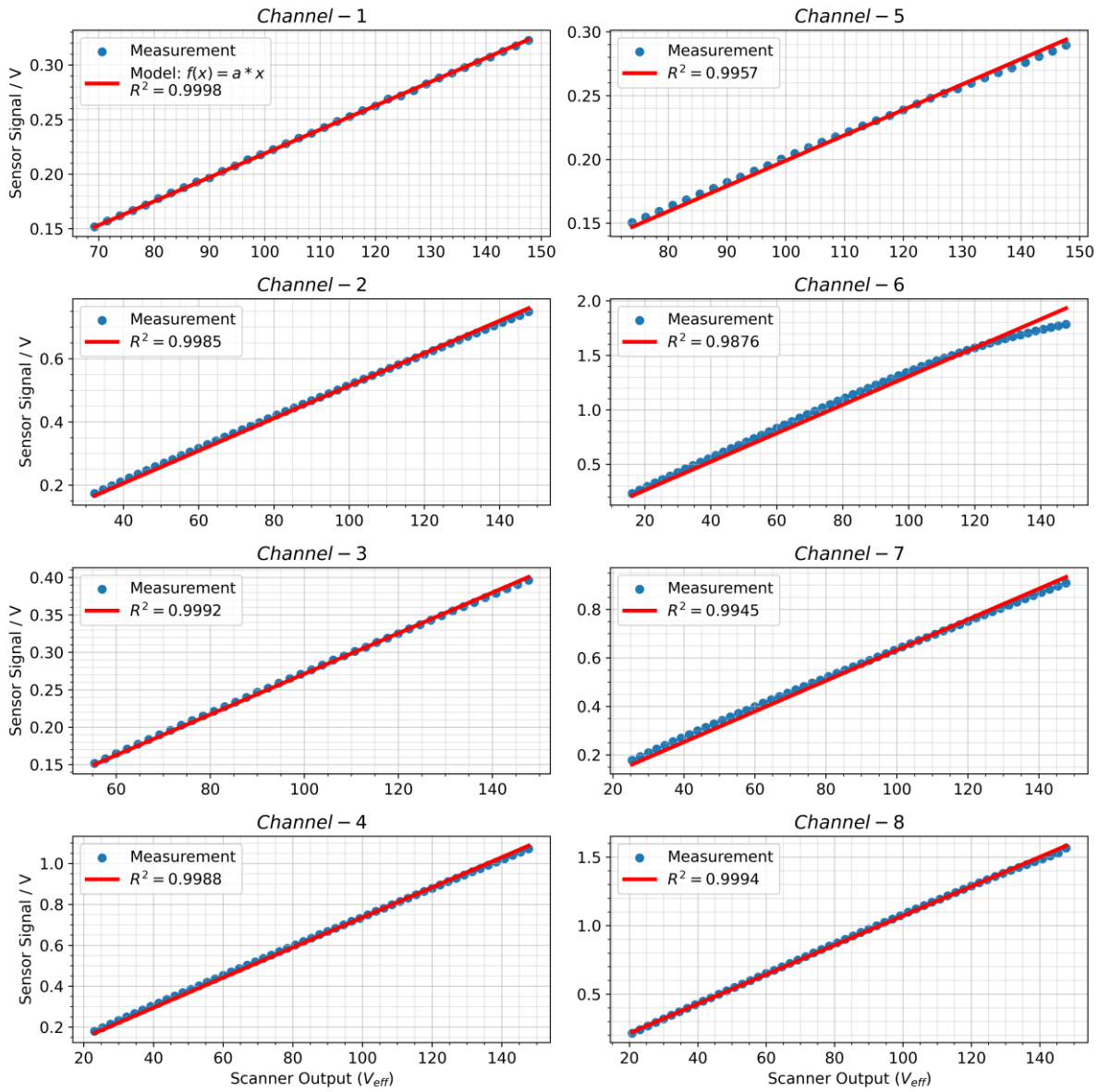

Figure 5.13 Implant sensor signal measurements versus scanner's effective output (adjusted via the MRI console) voltage of a single pTx channel at the MRI scanner. Above 1.6 V, the implant's ADC input saturates due to its power limits. Overall, the linearity between measured induced signals and the scanner input well correlated with an $R^2 \geq 0.99$.

5.3.3. MR experiments

The results of the MRI experiments for the RF safety metrics for all six realistic DBS lead trajectories are shown in Figure 5.14. In Figure 5.14A, the normalized amplitudes of the $\boldsymbol{Q}_S^E$ matrices demonstrate the channel contributions from the

various pTx channels, which were acquired with the wireless communication link between MRI and the constructed implant. It can be observed that each of the six DBS lead configurations shows a unique RF coupling behavior to the RF coil channels, even in the same homogeneous medium. Consequently, as demonstrated in Figure 5.14B, the RF-induced currents for the reference CP mode or WC mode transmission show different induced implant tip signals for the same transmitted total power. The RF induced signals measured by the implant were between 0.223-1.335 V for the CP mode and 0.572-1.841 V WC mode. The wireless pTx mitigation using the OP and NM modes reduced the RF-induced signals for all configurations. For the OP mode, the measured voltages varied between 0.002-0.137 V; for the NM, between 0.001-0.125 V.

The 67 s long RF-heating experiments for all DBS lead configurations and the pTx excitation modes are shown in Figure 5.14C. The temperature rises measured by the external fiber-optic probe and wirelessly measured RF-induced currents demonstrate that the RMS sensor in the implant case can measure the relevant pTx RF-safety parameters using $\boldsymbol{Q_S^E}$. As expected, the calculated WC mode has the maximum RF-induced heating (0.52-3.33 K), while CP heating varied with each configuration (0.07-1.28 K). The pTx mitigations were successful at all six configurations either using the OP or NM modes. The OP and NM modes reduced RF-induced heating for all DBS trajectories with temperature rises between 0.03-0.14 K and 0.00-0.07 K respectively. A detailed summary of the RF-induced signals and temperatures for each DBS lead configuration is given in Table 5-2.

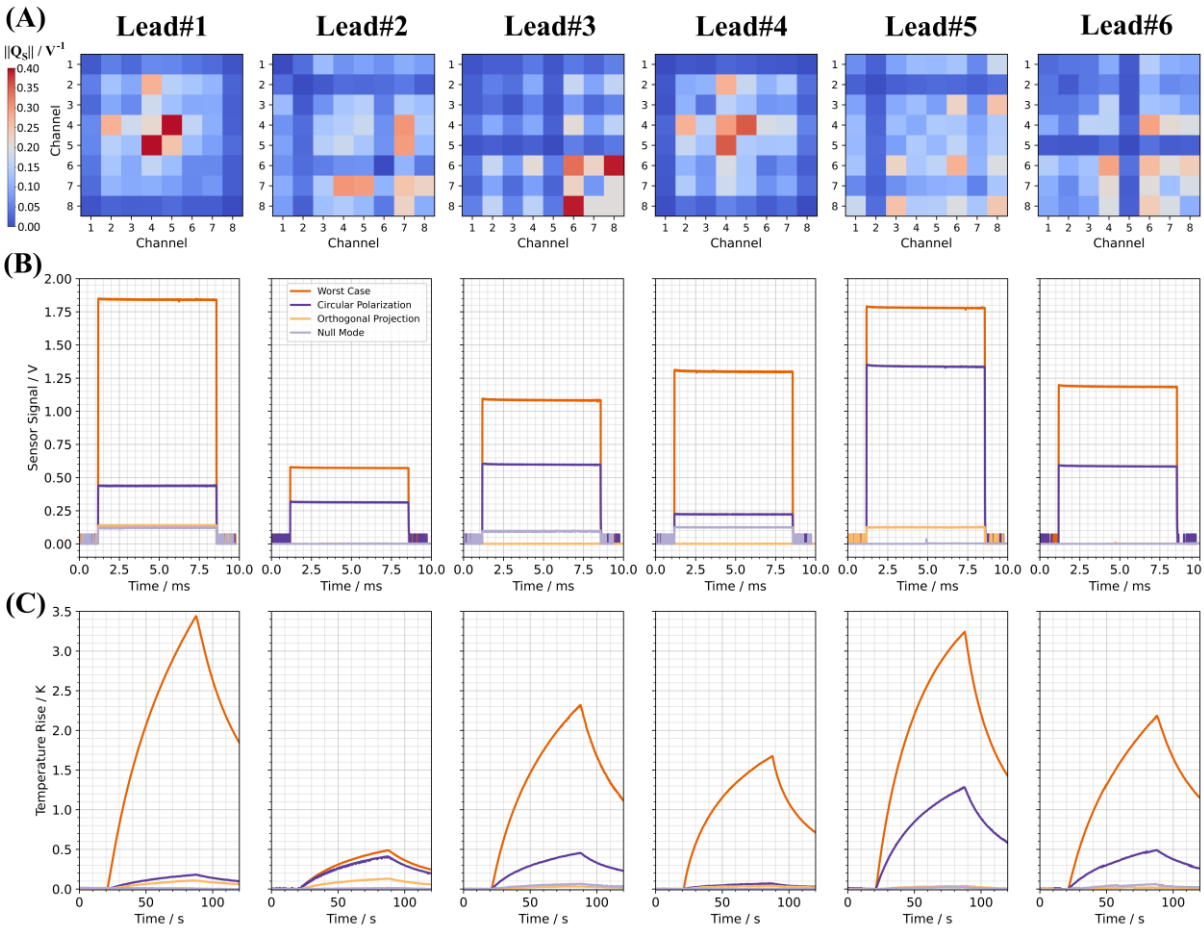

Figure 5.14 The results of the pTx mitigation experiments using all six realistic DBS lead trajectories at the 3T MR scanner. A) Normalized amplitudes of the calculated $\boldsymbol{Q}_S^E$ are shown. B) Wirelessly measured RF-induced signals by the implant are displayed for WC, CP and OP transmission modes. C) Corresponding RF-induced heating for all six implant lead configurations and all pTx transmission modes measured by fiber-optic temperature probes.

Table 5-2 The RF-induced signals and the corresponding temperature rises of the six realistic DBS implant leads for different pTx excitation modes. WC, OP, and NM were calculated by using wirelessly acquired $\boldsymbol{Q_S^E}$ in the MRI setting.

Lead#	Induced signal / V				Temperature rise / K			
	WC	CP	OP	NM	WC	CP	OP	NM
1	1.841	0.438	0.137	0.121	3.33	0.21	0.14	0.00
2	0.572	0.313	0.003	0.002	0.52	0.42	0.13	0.01
3	1.082	0.597	0.002	0.093	2.32	0.46	0.03	0.07
4	1.297	0.223	0.002	0.125	1.68	0.07	0.04	0.00
5	1.779	1.335	0.124	0.003	3.26	1.28	0.04	0.02
6	1.184	0.583	0.002	0.001	2.19	0.50	0.04	0.07

The longer (400 s) RF-heating experiments to evaluate the pTx mitigation performance for an average MR sequence timing are shown in Figure 5.15. During the pTx experiments, the WC mode RF-induced maximum temperature rise was 3.14 K (probe #1) and 2.24 K (probe #2). The CP mode RF-induced heating was 0.81 K and 0.67 K after 400 seconds for probes #1 and #2, respectively. The pTx mitigation using wirelessly acquired $\boldsymbol{Q_S^E}$ shows substantial RF-heating reduction for NM and OP. The RF-heating was <0.12 K for the NM and <0.05 K for the OP mode.

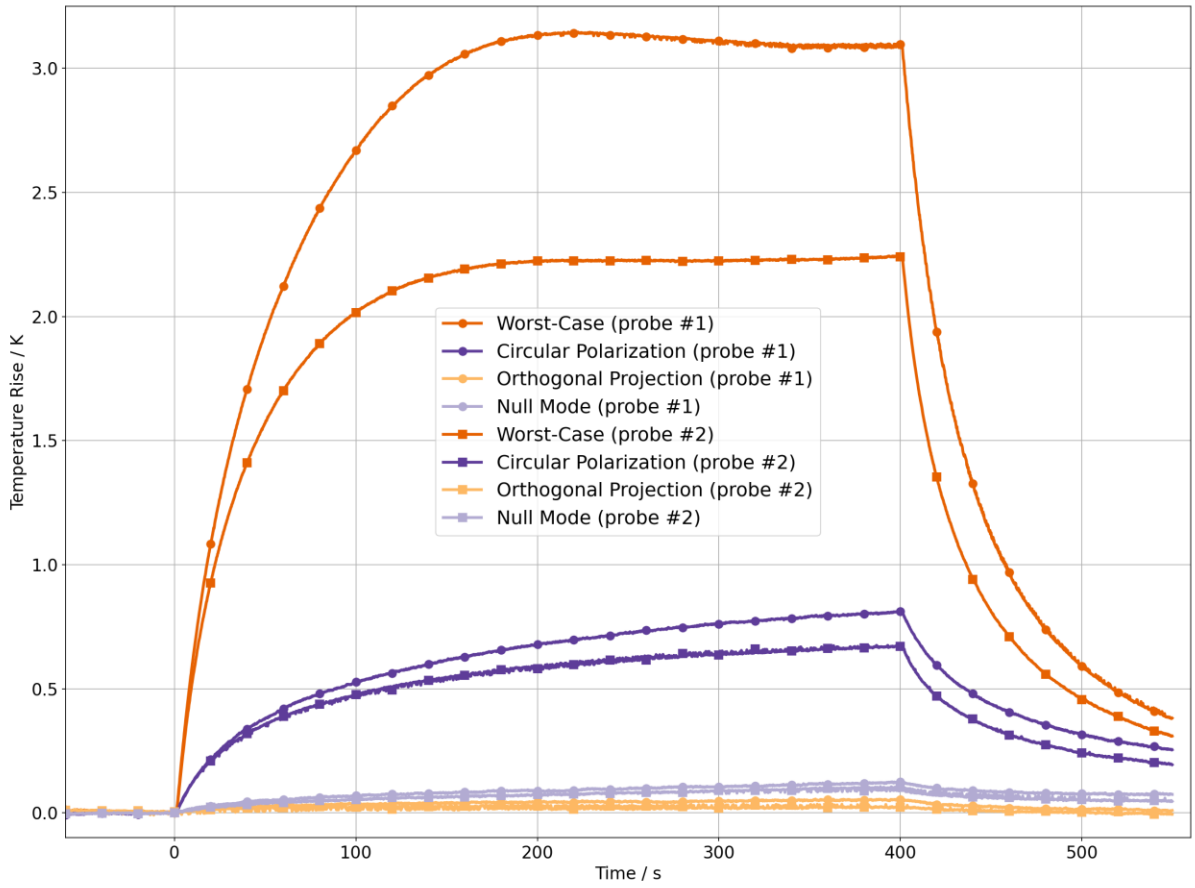

Figure 5.15 RF heating experiment (400 s performed with Lead #3.) for the pTx excitation modes WC, CP, OP and NM. The fiber-optic temperature probe locations are shown in Figure 5.4. The small spatial (~1 mm) difference in temperature probes effects the absolute temperature increase.

MR imaging experiments to further investigate the imaging performance of the pTx mitigations are shown in Figure 5.16. A single coronal slice that coincides with the implant tip was selected for all lead configurations. It is evident that the RF-induced signals close to the implant wire are the highest for WC, because the RF-induced currents create B_1^+ imaging artifacts around the conductive wire. NM and OP substantially reduce the artefacts, while NM has the overall lowest image quality considering the entire imaging region. For Lead #1, Lead #4 and Lead #6 imaging performance of OP is comparable to CP, while for Lead #2-3 and Lead #5 it is slightly degraded in some regions in the phantom.

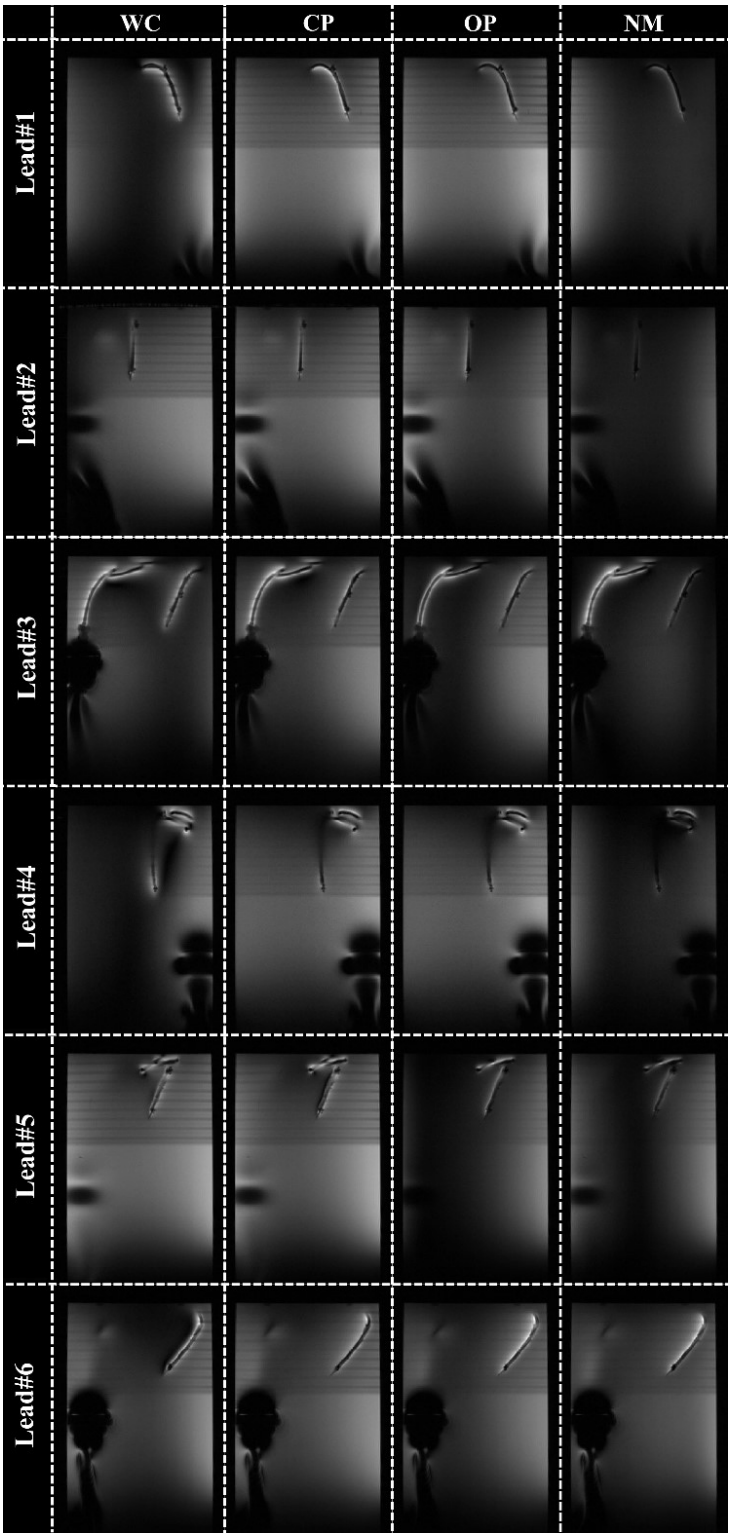

Figure 5.16 Coronal MR images of all realistic lead trajectories (Lead #1 to Lead #6) for pTx excitation modes WC, CP, OP, and NM that were calculated using the wirelessly transmitted implant sensor signal. The total transmit power and the scaling factor are the same for all imaging modes. OP mostly preserves the imaging quality.

5.4. Discussion

In this chapter, wireless reference implant hardware and a wireless communication workflow between the implant and an MRI scanner were implemented to demonstrate a potential RF safety workflow for AIMDs. The implant hardware is equipped with small RMS sensors and together with $\boldsymbol{Q_S^E}$ acquisition and OP mode calculations, safe excitation settings could be determined on-the-fly maintaining imaging quality.

5.4.1. Implant hardware and wireless communication

The presented implant hardware was constructed to acquire the information about the RF-induced signal at the implant tip by using a rectification circuit inside the implant casing. Some implants may already have similar electronic components that could be used for RF safety in MRI; for example, measuring activity from the neurons to implement a closed loop stimulation.[189,190]

Other detector designs to measure gradient-induced and RF-induced fields also exist.[191,192] The provided design can be improved by adapting other small-form RF-detector modules that are commonly implemented in millimeter-wave communication antennas.[193,194] The size of the on-chip RF power detectors can be even smaller than $0.04\ mm^2$.[195]

Using the SoC, the measured RF-induced signals at the implant tip could be measured by its ADC and its BLE link was used for the data transmission. The data transmission for the 8-channel $\boldsymbol{Q_S}$ was limited to 15 ms (7.5 ms $\boldsymbol{Q_S^E}$ + 7.5 ms BLE timing uncertainty). The BLE timing uncertainty could not be reduced any further because it is at the limit according to the current BLE standard.[186] Moreover, there was an adjusted 100 ms latency for the RF pulse after the RF-trigger from the MR scanner. The delay provides processing time to the SoC, which can be improved further by optimizing the firmware or using faster microprocessors.

There are other application specific timing limitations during the wireless data transfer. In this implementation, all $\boldsymbol{Q_S^E}$ raw data was transmitted from the SoC for the data analysis. This can be improved by implementing on-chip $\boldsymbol{Q_S^E}$ data

extraction and pTx excitation vector calculations. These calculations could reduce the transmitted data load more than several hundred times compared to the current implementation.

Even though the abovementioned timing limitations exist and can be improved, it should be noted that continuous $\boldsymbol{Q_S^E}$ acquisition is unnecessary for imaging patients with implants as long as field distribution is not changed (e.g., patient motion). Monitoring patients through rapid wireless E-field measurements embedded in a clinical sequence, with intervals in the order of seconds, can tremendously enhance RF safety for patients with implants. This improvement can be achieved without a pTx system as well because of direct E-field measurements from the implant.

5.4.2. Lead design

The realistic lead implementation in this chapter were used from open patient DBS data.[68] However, it should be noted that the fine details of the lead design can vary according to lead manufacturers. This would have changed the absolute value of the RF-induced heating values.[101,196,197] In this thesis, these structural differences were not addressed. Lead design may also alter the method how $\boldsymbol{Q_S^E}$ can be acquired. The RF-induced voltage between inner and outer conductor of the lead was utilized in this work. The outer conductor shields the spurious RF signals from the $\boldsymbol{Q_S^E}$ measurements. Although similar DBS leads exists,[198] other methods such as differential signaling can be implemented for unshielded DBS leads having multiple wires. Further investigations for the robustness of the $\boldsymbol{Q_S^E}$ for these types of leads should be conducted.

Although the main focus of this chapter is on the acquisition of the E-field based $\boldsymbol{Q_S}$ ($\boldsymbol{Q_S^E}$), which affected the lead design, the temperature-based $\boldsymbol{Q_S}$ ($\boldsymbol{Q_S^T}$) can be used as well. The temperature probes at the implant tip or ablation catheter were already discussed in the previous chapter.[120,156,157] It would be also straightforward to implement wireless communication for slower temperature measurements as well. The main advantage of these type of leads would be the option of direct

thermal dose calculations such as using the CEM43 concept in (Equation (2.8)).[83–85]

5.4.3. Sensor calibration

Although the same Schottky diode was used as in the previous chapter (4.3.), the dynamic range of the measurements were much higher in this chapter because the receiver circuit was matched. Therefore, the non-linearity of the Schottky diode became more visible and needed to be calibrated for better accuracy. The sensor can be calibrated for different MRI frequencies as shown at both 7T (Figure 5.10 and Figure 5.11) and 3T (Figure 5.13). This is needed to be performed for any sensor-embedded implant and for each MR frequency. Further calibrations can be performed to match sensor signal to temperature values at a given location by using temperature simulations considering the hotspot locations. It should be also noted that a safety factor should be added by considering the varying tissue parameters around the implant, which might influence the results.

Some technical remarks can also be made about the calibrations. The ADC of the used SoC can operate at a maximum number of 11.6 effective bits, which would indicate less than 4096 discrete voltage levels. This translates to approximately 1 mV resolution without considering the diode non-linearity correction. Therefore, the low-level fluctuations around the Schottky diode threshold can be attributed to the quantization errors and sensitivity problems at the ADC (Figure 5.10). For values above 1.6 V (see Figure 5.13), the SoC has its electrical limits. These types of limitations may affect the acquisition of the $\boldsymbol{Q_S^E}$. For example, $\boldsymbol{Q_S^E}$ acquired with very low-power settings may lead to uncertainties due to missing $\boldsymbol{Q_S^E}$ indices. Therefore, the dynamic range of the implant acquisition system needed to be considered and adjusted during the design step or a suitable RF transmission amplitude communicated by the implant to the MR system.

5.4.4. Wireless pTx mitigations

Wirelessly acquired $\boldsymbol{Q_S^E}$ data was sufficient to mitigate RF-induced heating at all six realistic DBS lead configurations demonstrated in 3T MRI experiments. The temperature rises for the WC mode were less than 4 K and for the reference CP

mode less than 2 K. These values should not indicate a realistic heating scenario for a patient with a DBS implant as the aim of the chapter is to demonstrate the safety concept of a sensor-equipped implant and its wireless communication with an MRI scanner. The 8-channel coil used in the experiments was driven with a relatively low-power (22 ± 0.5 W) for a coil with high losses. It should be also noted that it is a head-only pTx coil, where large parts of the implant lead and the AIMD casing are outside the main RF coil excitation region. Other volume coils such as body coil should also be investigated in future studies because unlike DBS implants, pacemakers may be entirely exposed to strong E-fields resulting in implant tip temperature rise of more than 25 K as demonstrated in other studies.[69]

It should be also noted that MR imaged-based methods can be used as a complementary method to determine if there is a current at the tip of the wire.[51,56,57,115,117,118] This would have the advantage, that no sensors are needed at an implant, which is a more general solution to the implant safety problem. The drawback of image-based methods is the additional time needed to assess the RF safety threat and its susceptibility to errors due to image artefacts. Sensors on the other hand provide fast and independent measurements that do not require MR scanner components used for imaging. A combination of both methods is also feasible to improve robustness.

A further remark can be made to extend the work to multiple implants and multiple leads.[53,199,200] $\boldsymbol{Q_S}$, acquired from multiple sources can be easily combined at the scanner to adjust pTx mitigation settings. This is an important argument in a complex configuration, since each implant and implant vendor would be responsible for the individual implant only determining the $\boldsymbol{Q_S}$ and sending this information to the MR system. The MR system on the other hand would be able to use the information of multiple $\boldsymbol{Q_S}$ implant sources and embed it in the overall safety assessment including the native RF safety case.[162]

5.4.5. Imaging performance of OP method

It was shown that OP still produces similar imaging quality to CP even for complex lead trajectories. However, it has been also observed that in some configurations e.g., for Lead#5, the imaging performance of the OP mode is significantly

degraded compared to the CP (Figure 5.16). For this particular lead trajectory, the amplitude distribution of the $\boldsymbol{Q}_S^E$ (Figure 5.14A) showed a more homogeneous distribution compared to other lead trajectories, where all channels could contribute to the RF-induced signals. Hence, the WC was similar to the CP mode, which was also confirmed by the sensor signals. Therefore, the OP method may not be sufficient since by definition, it is orthogonal to the WC vector. This condition is, however, easily detectable and other strategies for the imaging vector may be applied in this case. For example, another B_1-shim vector to image a dedicated area outside of the implant could be used for the projection with WC as demonstrated in Figure 4.17. Faster B_1^+-mapping techniques[201–203] to optimize $\boldsymbol{Q}_S$ based RF-induced heating calculations and the imaging using optimization methods similar to the Equation (2.23) can also be implemented in future works.

6. Conclusion

This thesis demonstrates the feasibility of using sensor-equipped implants for enhanced assessment and reduction of RF-induced heating by parallel transmission MRI.

First, a pTx hardware for automated implant safety testing was developed and constructed allowing measurements of an extensive range of various RF safety scenarios, which in quantity was limited, so far, to simulations only. Next, the Orthogonal Projection method was implemented, which rapidly calculates a transmission vector solely based on a sensor signal to substantially reduce the heating threat and maintain imaging quality. This methodology was tested on time-domain E-field probes and extended to root-mean-square sensors with the so-called sensor Q-matrix methodology. The utilization of miniaturized low-cost sensors that can potentially be embedded within the implant lead tip or the implant casing, demonstrated a realistic configuration that can be translated to actual implant hardware. Moreover, a wireless reference implant and wireless communication workflow were developed, implemented, and investigated. It highlights the potential of the presented work to be translated into a novel implant safety concept, where a “smart” implant communicates with an MR scanner utilizing on-the-fly safety related patient-specific and in-situ information improving patient safety and imaging. This novel safety concept was successfully tested in approximately 400 different implant configurations at 3T and 7T MRI frequencies, in four different phantoms, with complex lead trajectories, in and outside of the MR scanner.

A smart implant safety concept can drastically boost the current safety practice by evidently differentiating implant safety responsibilities among implant and MR manufacturers. Consequently, it would also alleviate the current burden on clinical personal assessing and implementing implant safety procedures.

7. References

1. OECD (2021). Trends in life expectancy. In: *Health at a Glance 2021: OECD Indicators*. OECD Publishing. Accessed August 26, 2022. https://doi.org/10.1787/e0d509f9-en

2. Winter L, Seifert F, Zilberti L, Murbach M, Ittermann B. MRI-Related Heating of Implants and Devices: A Review. *J Magn Reson Imaging*. doi:10.1002/jmri.27194

3. Barkhausen J, Kahn T, Krombach GA, Kuhl CK, Lotz J, Maintz D, Ricke J, Schönberg SO, Vogl TJ, Wacker FK, Radiology (KLR) GA of C in A. White Paper: Interventional MRI: Current Status and Potential for Development Considering Economic Perspectives, Part 1: General Application. *RöFo - Fortschritte Auf Dem Geb Röntgenstrahlen Bildgeb Verfahr*. 2017;189(7):611-623. doi:10.1055/s-0043-110011

4. Boy, 6, Dies Of Skull Injury During M.R.I. - The New York Times. Accessed August 25, 2022. https://www.nytimes.com/2001/07/31/nyregion/boy-6-dies-of-skull-injury-during-mri.html

5. Molloy M. Indian man dies after freak MRI machine accident at Mumbai hospital. *The Telegraph*. https://www.telegraph.co.uk/news/2018/01/29/indian-man-dies-freak-mri-machine-accident-mumbai-hospital/. Published January 29, 2018. Accessed August 25, 2022.

6. Glover PM. Interaction of MRI field gradients with the human body. *Phys Med Biol*. 2009;54(21):R99-R115. doi:10.1088/0031-9155/54/21/R01

7. Klein V, Davids M, Schad LR, Wald LL, Guérin B. Investigating cardiac stimulation limits of MRI gradient coils using electromagnetic and electrophysiological simulations in human and canine body models. *Magn Reson Med*. 2021;85(2):1047-1061. doi:10.1002/mrm.28472

8. International Electrotechnical Commission (IEC). *Medical Electrical Equipment. Particular Requirements for the Safety of Magnetic Resonance Equipment for Medical Diagnosis.*; 2010.

9. THE EUROPEAN PARLIAMENT AND OF THE COUNCIL of 5 April 2017. REGULATION (EU) 2017/745 on medical devices. *Official Journal of the European Union*. 2017;117:16.

10. Shellock FG, Crues JV. MR Procedures: Biologic Effects, Safety, and Patient Care. *Radiology*. 2004;232(3):635-652. doi:10.1148/radiol.2323030830

11. Erhardt JB, Fuhrer E, Gruschke OG, Leupold J, Wapler MC, Hennig J, Stieglitz T, Korvink JG. Should patients with brain implants undergo MRI? *J Neural Eng*. 2018;15(4):041002. doi:10.1088/1741-2552/aab4e4

12. Brühl R, Ihlenfeld A, Ittermann B. Gradient heating of bulk metallic implants can be a safety concern in MRI. *Magn Reson Med*. 2017;77(5):1739-1740. doi:10.1002/mrm.26652

13. Zilberti L, Bottauscio O, Chiampi M, Hand J, Lopez HS, Brühl R, Crozier S. Numerical prediction of temperature elevation induced around metallic hip prostheses by traditional, split, and uniplanar gradient coils. *Magn Reson Med*. 2015;74(1):272-279. doi:10.1002/mrm.25687

14. Arduino A, Bottauscio O, Brühl R, Chiampi M, Zilberti L. In silico evaluation of the thermal stress induced by MRI switched gradient fields in patients with metallic hip implant. *Phys Med Ampmathsemicolon Biol*. 2019;64(24):245006. doi:10.1088/1361-6560/ab5428

15. Zilberti L, Bottauscio O, Chiampi M, Hand J, Lopez HS, Crozier S. Collateral Thermal Effect of MRI-LINAC Gradient Coils on Metallic Hip Prostheses. *IEEE Trans Magn*. 2014;50(11):1-4. doi:10.1109/TMAG.2014.2323119

16. Nyenhuis JA, Sung-Min Park, Kamondetdacha R, Amjad A, Shellock FG, Rezai AR. MRI and implanted medical devices: basic interactions with an emphasis

on heating. *IEEE Trans Device Mater Reliab*. 2005;5(3):467-480. doi:10.1109/TDMR.2005.859033

17. Henderson JM, Tkach J, Phillips M, Baker K, Shellock FG, Rezai AR. Permanent neurological deficit related to magnetic resonance imaging in a patient with implanted deep brain stimulation electrodes for Parkinson's disease: case report. *Neurosurgery*. 2005;57(5):E1063; discussion E1063.

18. Spiegel J, Fuss G, Backens M, Reith W, Magnus T, Becker G, Moringlane JR, Dillmann U. Transient dystonia following magnetic resonance imaging in a patient with deep brain stimulation electrodes for the treatment of Parkinson disease. *J Neurosurg*. 2003;99(4):772-774. doi:10.3171/jns.2003.99.4.0772

19. Yeung CJ, Susil RC, Atalar E. RF heating due to conductive wires during MRI depends on the phase distribution of the transmit field. *Magn Reson Med*. 2002;48(6):1096-1098. doi:10.1002/mrm.10310

20. Yeung CJ, Susil RC, Atalar E. RF safety of wires in interventional MRI: using a safety index. *Magn Reson Med*. 2002;47(1):187-193.

21. ASTM F2503-13. Standard Practice for Marking Medical Devices and Other Items for Safety in the Magnetic Resonance Environment.

22. FDA-2019-D-2837. Testing and Labeling Medical Devices for Safety in the Magnetic Resonance (MR) Environment. U.S. Food and Drug Administration.

23. Tanaka R, Yumoto T, Shiba N, Okawa M, Yasuhara T, Ichikawa T, Tokunaga K, Date I, Ujike Y. Overheated and melted intracranial pressure transducer as cause of thermal brain injury during magnetic resonance imaging: Case report. *J Neurosurg*. 2012;117(6):1100-1109. doi:10.3171/2012.9.JNS12738

24. Russo R. Determining the risks of clinically indicated nonthoracic magnetic resonance imaging at 1.5 T for patients with pacemakers and implantable cardioverter-defibrillators: rationale and design of the MagnaSafe Registry. *Am Heart J*. 2013;165(3):266-272. doi:10.1016/j.ahj.2012.12.004

25. The MagnaSafe Registry. Accessed March 30, 2020. http://magnasafe.org/aboutmagnasafe.html

26. ASTM F2182 - 11 Standard Test Method for Measurement of Radio Frequency Induced Heating Near Passive Implants During Magnetic Resonance Imaging. Accessed March 22, 2020. https://www.astm.org/DATABASE.CART/HISTORICAL/F2182-11.htm

27. IEC 60601-2-33:2010+AMD1:2013+AMD2:2015 CSV | IEC Webstore. Accessed November 8, 2021. https://webstore.iec.ch/publication/22705

28. *ISO - ISO/TS 10974:2018 - Assessment of the Safety of Magnetic Resonance Imaging for Patients with an Active Implantable Medical Device*. Accessed October 13, 2019. https://www.iso.org/standard/65055.html

29. Park SM, Kamondetdacha R, Nyenhuis JA. Calculation of MRI-induced heating of an implanted medical lead wire with an electric field transfer function. *J Magn Reson Imaging*. 2007;26(5):1278-1285. doi:10.1002/jmri.21159

30. Boutet A, Chow CT, Narang K, Elias GJB, Neudorfer C, Germann J, Ranjan M, Loh A, Martin AJ, Kucharczyk W, Steele CJ, Hancu I, Rezai AR, Lozano AM. Improving Safety of MRI in Patients with Deep Brain Stimulation Devices. *Radiology*. 2020;296(2):250-262. doi:10.1148/radiol.2020192291

31. Ladd ME, Quick HH. Reduction of resonant RF heating in intravascular catheters using coaxial chokes. *Magn Reson Med*. 2000;43(4):615-619.

32. Gray RW, Bibens WT, Shellock FG. Simple design changes to wires to substantially reduce MRI-induced heating at 1.5 T: implications for implanted leads. *Magn Reson Imaging*. 2005;23(8):887-891. doi:10.1016/j.mri.2005.07.005

33. Bottomley PaulA, Edelstein WilliamA, Kumar Ananda, Allen JustinM, Karmarkar P. Resistance and Inductance Based MRI-Safe Implantable Lead Strategies. In: *Intl. Soc. Mag. Reson. Med.* ; 2009:4805. Accessed November 21, 2018. http://archive.ismrm.org/2009/4805.html

34. Bottomley PA, Kumar A, Edelstein WA, Allen JM, Karmarkar PV. Designing passive MRI-safe implantable conducting leads with electrodes. *Med Phys*. 2010;37(7Part1):3828-3843. doi:10.1118/1.3439590

35. Golestanirad L, Angelone LM, Kirsch J, Downs S, Keil B, Bonmassar G, Wald LL. Reducing RF-Induced Heating Near Implanted Leads Through High-Dielectric Capacitive Bleeding of Current (CBLOC). *IEEE Trans Microw Theory Tech*. 2019;67(3):1265-1273. doi:10.1109/TMTT.2018.2885517

36. Serano P, Angelone LM, Katnani H, Eskandar E, Bonmassar G. A Novel Brain Stimulation Technology Provides Compatibility with MRI. *Sci Rep*. 2015;5(1):9805. doi:10.1038/srep09805

37. Elwassif MM, Datta A, Rahman A, Bikson M. Temperature control at DBS electrodes using a heat sink: experimentally validated FEM model of DBS lead architecture. *J Neural Eng*. 2012;9(4):046009. doi:10.1088/1741-2560/9/4/046009

38. Acikel V, Silemek B, Atalar E. Wireless control of induced radiofrequency currents in active implantable medical devices during MRI. *Magn Reson Med*. 2020;83(6):2370-2381. doi:10.1002/mrm.28089

39. Özen AC, Silemek B, Lottner T, Atalar E, Bock M. MR safety watchdog for active catheters: Wireless impedance control with real-time feedback. *Magn Reson Med*. 2020;84(2):1048-1060. doi:10.1002/mrm.28153

40. Greatbatch W, Miller V, Shellock FG. Magnetic resonance safety testing of a newly-developed fiber-optic cardiac pacing lead. *J Magn Reson Imaging*. 2002;16(1):97-103. doi:10.1002/jmri.10129

41. Turner PF. Regional Hyperthermia with an Annular Phased Array. *IEEE Trans Biomed Eng*. 1984;BME-31(1):106-114. doi:10.1109/TBME.1984.325376

42. Arcangeli G, Lombardini PP, Lovisolo GA, Marsiglia G, Piattelli M. Focusing of 915 MHz Electromagnetic Power on Deep Human Tissues: A Mathematical

Model Study. *IEEE Trans Biomed Eng*. 1984;BME-31(1):47-52. doi:10.1109/TBME.1984.325369

43. Hand JW, Cheetham JL, Hind AJ. Absorbed Power Distributions from Coherent Microwave Arrays for Localized Hyperthermia. *IEEE Trans Microw Theory Tech*. 1986;34(5):484-489. doi:10.1109/TMTT.1986.1133380

44. Bardati F, Borrani A, Gerardino A, Lovisolo GA. SAR optimization in a phased array radiofrequency hyperthermia system. *IEEE Trans Biomed Eng*. 1995;42(12):1201-1207. doi:10.1109/10.476127

45. Seifert F, Rinneberg H. Adaptive Coil Control: SNR Optimization of a TR Volume Coil for Single Voxel MRS at 3T. In: *Intl. Soc. Mag. Reson. Med*. Vol 10. ; 2002:162.

46. Zhu Y. Parallel excitation with an array of transmit coils. *Magn Reson Med*. 2004;51(4):775-784. doi:10.1002/mrm.20011

47. Katscher U, Börnert P, Leussler C, Brink JS van den. Transmit SENSE. *Magn Reson Med*. 2003;49(1):144-150. doi:10.1002/mrm.10353

48. Ullmann P, Junge S, Wick M, Seifert F, Ruhm W, Hennig J. Experimental analysis of parallel excitation using dedicated coil setups and simultaneous RF transmission on multiple channels. *Magn Reson Med*. 2005;54(4):994-1001. doi:10.1002/mrm.20646

49. Eryaman Y, Guerin B, Akgun C, Herraiz JL, Martin A, Torrado-Carvajal A, Malpica N, Hernandez-Tamames JA, Schiavi E, Adalsteinsson E, Wald LL. Parallel transmit pulse design for patients with deep brain stimulation implants. *Magn Reson Med*. 2015;73(5):1896-1903. doi:10.1002/mrm.25324

50. Eryaman Y, Akin B, Atalar E. Reduction of implant RF heating through modification of transmit coil electric field. *Magn Reson Med*. 2011;65(5):1305-1313. doi:10.1002/mrm.22724

51. Eryaman Y, Turk EA, Oto C, Algin O, Atalar E. Reduction of the radiofrequency heating of metallic devices using a dual-drive birdcage coil. *Magn Reson Med*. 2013;69(3):845-852. doi:10.1002/mrm.24316

52. McElcheran CE, Yang B, Anderson KJT, Golenstani-Rad L, Graham SJ. Investigation of Parallel Radiofrequency Transmission for the Reduction of Heating in Long Conductive Leads in 3 Tesla Magnetic Resonance Imaging. Xu B, ed. *PLOS ONE*. 2015;10(8):e0134379. doi:10.1371/journal.pone.0134379

53. McElcheran CE, Yang B, Anderson KJT, Golestanirad L, Graham SJ. Parallel radiofrequency transmission at 3 tesla to improve safety in bilateral implanted wires in a heterogeneous model. *Magn Reson Med*. 2017;78(6):2406-2415. doi:10.1002/mrm.26622

54. McElcheran CE, Golestanirad L, Iacono MI, Wei PS, Yang B, Anderson KJT, Bonmassar G, Graham SJ. Numerical Simulations of Realistic Lead Trajectories and an Experimental Verification Support the Efficacy of Parallel Radiofrequency Transmission to Reduce Heating of Deep Brain Stimulation Implants during MRI. *Sci Rep*. 2019;9(1). doi:10.1038/s41598-018-38099-w

55. Yang B, Wei PS, McElcheran CE, Tam F, Graham SJ. A Platform for 4-Channel Parallel Transmission MRI at 3 T: Demonstration of Reduced Radiofrequency Heating in a Test Object Containing an Implanted Wire. *J Med Biol Eng*. 2019;39(6):835-844. doi:10.1007/s40846-019-00478-7

56. Sadeghi-Tarakameh A, Zulkarnain NIH, He X, Atalar E, Harel N, Eryaman Y. A workflow for predicting temperature increase at the electrical contacts of deep brain stimulation electrodes undergoing MRI. *Magn Reson Med*. 2022;88(5):2311-2325. doi:10.1002/mrm.29375

57. Eryaman Y, Kobayashi N, Moen S, Aman J, Grant A, Vaughan JT, Molnar G, Park MC, Vitek J, Adriany G, Ugurbil K, Harel N. A simple geometric analysis method for measuring and mitigating RF induced currents on Deep Brain Stimulation leads by multichannel transmission/reception. *NeuroImage*. 2019;184:658-668. doi:10.1016/J.NEUROIMAGE.2018.09.072

58. Guerin B, Angelone LM, Dougherty D, Wald LL. Parallel transmission to reduce absorbed power around deep brain stimulation devices in MRI: Impact of number and arrangement of transmit channels. *Magn Reson Med*. 2020;83(1):299-311. doi:10.1002/mrm.27905

59. Gudino N, Sonmez M, Yao Z, Baig T, Nielles-Vallespin S, Faranesh AZ, Lederman RJ, Martens M, Balaban RS, Hansen MS, Griswold MA. Parallel transmit excitation at 1.5 T based on the minimization of a driving function for device heating. *Med Phys*. 2014;42(1):359-371. doi:10.1118/1.4903894

60. Córcoles J, Zastrow E, Kuster N. On the estimation of the worst-case implant-induced RF-heating in multi-channel MRI. *Phys Med Biol*. 2017;62(12):4711-4727. doi:10.1088/1361-6560/aa641b

61. Etezadi-Amoli M, Stang P, Kerr A, Pauly J, Scott G. Controlling radiofrequency-induced currents in guidewires using parallel transmit. *Magn Reson Med*. 2015;74(6):1790-1802. doi:10.1002/mrm.25543

62. Seifert F, Weidemann G, Ittermann B. Q matrix approach to control implant heating by transmit array coils. In: *Intl. Soc. Mag. Reson. Med.* Vol 23. ; 2015:3212.

63. Winter L, Silemek B, Petzold J, Pfeiffer H, Hoffmann W, Seifert F, Ittermann B. Parallel transmission medical implant safety testbed: Real-time mitigation of RF induced tip heating using time-domain E-field sensors. *Magn Reson Med*. 2020;84(6):3468-3484. doi:https://doi.org/10.1002/mrm.28379

64. Silemek B, Seifert F, Petzold J, Hoffmann W, Pfeiffer H, Speck O, Rose G, Ittermann B, Winter L. Rapid safety assessment and mitigation of radiofrequency induced implant heating using small root mean square sensors and the sensor matrix Qs. *Magn Reson Med*. 2022;87(1):509-527. doi:10.1002/mrm.28968

65. Petzold J, Ittermann B, Seifert F. Robustness of pTx safety concepts to varying subjects and subject positions. In: *Intl. Soc. Mag. Reson. Med.* ; 2021:2488.

66. Christ A, Kainz W, Hahn EG, Honegger K, Zefferer M, Neufeld E, Rascher W, Janka R, Bautz W, Chen J, Kiefer B, Schmitt P, Hollenbach HP, Shen J, Oberle M, Szczerba D, Kam A, Guag JW, Kuster N. The Virtual Family — development of surface-based anatomical models of two adults and two children for dosimetric simulations. *Phys Med Biol*. 2010;55(2):N23-N38. doi:10.1088/0031-9155/55/2/N01

67. Gosselin MC, Neufeld E, Moser H, Huber E, Farcito S, Gerber L, Jedensjö M, Hilber I, Gennaro FD, Lloyd B, Cherubini E, Szczerba D, Kainz W, Kuster N. Development of a new generation of high-resolution anatomical models for medical device evaluation: the Virtual Population 3.0. *Phys Med Biol*. 2014;59(18):5287-5303. doi:10.1088/0031-9155/59/18/5287

68. Guerin B, Iacono MI, Davids M, Dougherty D, Angelone LM, Wald LL. The 'virtual DBS population': five realistic computational models of deep brain stimulation patients for electromagnetic MR safety studies. *Phys Med Biol*. 2019;64(3):035021. doi:10.1088/1361-6560/aafce8

69. Mattei E, Triventi M, Calcagnini G, Censi F, Kainz W, Mendoza G, Bassen HI, Bartolini P. Complexity of MRI induced heating on metallic leads: experimental measurements of 374 configurations. *Biomed Eng Online*. 2008;7:11. doi:10.1186/1475-925X-7-11

70. Kopanoglu E, Deniz CM, Erturk MA, Wise RG. Specific absorption rate implications of within-scan patient head motion for ultra-high field MRI. *Magn Reson Med*. 2020;84(5):2724-2738. doi:10.1002/mrm.28276

71. Schoen N, Seifert F, Petzold J, Metzger GJ, Speck O, Ittermann B, Schmitter S. The Impact of Respiratory Motion on Electromagnetic Fields and Specific Absorption Rate in Cardiac Imaging at 7T. *Magn Reson Med*. 2022;88(6):2645-2661. doi:10.1002/mrm.29402

72. Godinez F, Scott G, Padormo F, Hajnal JV, Malik SJ. Safe guidewire visualization using the modes of a PTx transmit array MR system. *Magn Reson Med*. 2020;83(6):2343-2355. doi:10.1002/mrm.28069

73. Godinez F, Tomi-Tricot R, Delcey M, Williams SE, Mooiweer R, Quesson B, Razavi R, Hajnal JV, Malik SJ. Interventional cardiac MRI using an add-on parallel transmit MR system: In vivo experience in sheep. *Magn Reson Med*. 2021;86(6):3360-3372. doi:10.1002/mrm.28931

74. Medical Implant Manufacturers' Safety Procedures (MIMAS). Published July 26, 2018. Accessed March 16, 2023. https://www.ptb.de/mimas/home/

75. Standardisation for safe implant scanning in MRI (STASIS). Accessed March 21, 2023. https://www.ptb.de/stasis/home

76. Bloch F, Hansen WW, Packard M. The Nuclear Induction Experiment. *Phys Rev*. 1946;70(7-8):474-485. doi:10.1103/PhysRev.70.474

77. Lauterbur PC. Image Formation by Induced Local Interactions: Examples Employing Nuclear Magnetic Resonance. *Nature*. 1973;242(5394):190-191. doi:10.1038/242190a0

78. Protection (ICNIRP)1 IC on NIR. Guidelines for Limiting Exposure to Electromagnetic Fields (100 kHz to 300 GHz). *Health Phys*. 2020;118(5):483-524.

79. Jackson JD. *Classical Electrodynamics*. 3rd Edition. John Wiley & Sons

80. Lorrain P, Corson DR, Lorrain F. *Electromagnetic Fields and Waves*. 3rd edition. W. H. Freeman and Company

81. Zhang X, Liu J, He B. Magnetic-Resonance-Based Electrical Properties Tomography: A Review. *IEEE Rev Biomed Eng*. 2014;7:87-96. doi:10.1109/RBME.2013.2297206

82. Wang Z, Lin JC, Mao W, Liu W, Smith MB, Collins CM. SAR and temperature: Simulations and comparison to regulatory limits for MRI. *J Magn Reson Imaging*. 2007;26(2):437-441. doi:10.1002/jmri.20977

83. Sapareto SA, Dewey WC. Thermal dose determination in cancer therapy. *Int J Radiat Oncol*. 1984;10(6):787-800. doi:10.1016/0360-3016(84)90379-1

84. Yarmolenko PS, Moon EJ, Landon C, Manzoor A, Hochman DW, Viglianti BL, Dewhirst MW. Thresholds for thermal damage to normal tissues: An update. *Int J Hyperthermia*. 2011;27(4):320-343. doi:10.3109/02656736.2010.534527

85. Van Rhoon GC, Samaras T, Yarmolenko PS, Dewhirst MW, Neufeld E, Kuster N. CEM43°C thermal dose thresholds: A potential guide for magnetic resonance radiofrequency exposure levels? *Eur Radiol*. 2013;23(8):2215-2227. doi:10.1007/s00330-013-2825-y

86. Brink VD, S J. Thermal Effects Associated with RF Exposures in Diagnostic MRI: Overview of Existing and Emerging Concepts of Protection. *Concepts Magn Reson Part B*. 2019;2019:e9618680. doi:10.1155/2019/9618680

87. Balanis CA. *Advanced Engineering Electromagnetics*. Second edition. John Wiley & Sons; 2012.

88. Dempsey MF, Condon B, Hadley DM. Investigation of the factors responsible for burns during MRI. *J Magn Reson Imaging*. 2001;13(4):627-631. doi:10.1002/jmri.1088

89. Balanis CA. *Antenna Theory Analysis and Design*. Third Edition. John Wiley & Sons; 2005.

90. Hasgall P, Di Gennaro F, Baumgartner C, Neufeld E, Lloyd B, Gosselin MC, Payne D, Klingenböck A, Kuster N. IT'IS Database for thermal and electromagnetic parameters of biological tissues, Version 4.1. Published online February 22, 2022. doi:10.13099/VIP21000-04-1

91. Li BK, Liu F, Weber E, Crozier S. Hybrid numerical techniques for the modelling of radiofrequency coils in MRI. *NMR Biomed*. 2009;22(9):937-951. doi:10.1002/nbm.1344

92. Neufeld E, Kühn S, Szekely G, Kuster N. Measurement, simulation and uncertainty assessment of implant heating during MRI. *Phys Med Biol*. 2009;54(13):4151-4169. doi:10.1088/0031-9155/54/13/012

93. Umashankar K, Taflove A. A Novel Method to Analyze Electromagnetic Scattering of Complex Objects. *IEEE Trans Electromagn Compat*. 1982;EMC-24(4):397-405. doi:10.1109/TEMC.1982.304054

94. Missoffe A, Aissani S. Experimental setup for transfer function measurement to assess RF heating of medical leads in MRI: Validation in the case of a single wire. *Magn Reson Med*. 2018;79(3):1766-1772. doi:10.1002/mrm.26773

95. Lottner T, Reiss S, Bitzer A, Bock M, Caglar Özen A. A Transfer Function Measurement Setup With an Electro-Optic Sensor for MR Safety Assessment in Cascaded Media. *IEEE Trans Electromagn Compat*. 2021;63(3):662-672. doi:10.1109/TEMC.2020.3040756

96. Feng S, Qiang R, Kainz W, Chen J. A Technique to Evaluate MRI-Induced Electric Fields at the Ends of Practical Implanted Lead. *IEEE Trans Microw Theory Tech*. 2015;63(1):305-313. doi:10.1109/TMTT.2014.2376523

97. Zastrow E, Yao A, Kuster N. Practical considerations in experimental evaluations of RF-induced heating of leaded implants. In: *2017 32nd General Assembly and Scientific Symposium of the International Union of Radio Science, URSI GASS 2017*. Vol 2017-January. ; 2017. doi:10.23919/URSIGASS.2017.8105350

98. Tokaya JP, Raaijmakers AJE, Luijten PR, van den Berg CAT. MRI-based, wireless determination of the transfer function of a linear implant: Introduction of the transfer matrix. *Magn Reson Med*. 2018;80(6):2771-2784. doi:10.1002/mrm.27218

99. Tokaya JP, Raaijmakers AJE, Luijten PR, Sbrizzi A, van den Berg CAT. MRI-based transfer function determination through the transfer matrix by jointly fitting the incident and scattered B1+ field. *Magn Reson Med*. 2020;83(3):1081-1095. doi:10.1002/mrm.27974

100. Tokaya JP, Berg CAT van den, Luijten PR, Raaijmakers AJE. Explaining RF induced current patterns on implantable medical devices during MRI using

the transfer matrix. *Med Phys*. 2021;48(1):132-141. doi:https://doi.org/10.1002/mp.14225

101. Acikel V, Atalar E. Modeling of radio-frequency induced currents on lead wires during MR imaging using a modified transmission line method. *Med Phys*. 2011;38(12):6623-6632. doi:10.1118/1.3662865

102. King RWP, Harrison C, Jr. *Antennas and Waves: A Modern Approach*. MIT Press; 1970.

103. Acikel V, Uslubas A, Atalar E. Modeling of electrodes and implantable pulse generator cases for the analysis of implant tip heating under MR imaging. *Med Phys*. 2015;42(7):3922-3931. doi:10.1118/1.4921019

104. Schmitz BL, Aschoff AJ, Hoffmann MHK, Grön G. Advantages and Pitfalls in 3T MR Brain Imaging: A Pictorial Review. *Am J Neuroradiol*. 2005;26(9):2229-2237.

105. Allison J, Yanasak N. What MRI Sequences Produce the Highest Specific Absorption Rate (SAR), and Is There Something We Should Be Doing to Reduce the SAR During Standard Examinations? *Am J Roentgenol*. 2015;205(2):W140-W140. doi:10.2214/AJR.14.14173

106. Susil RC, Yeung CJ, Halperin HR, Lardo AC, Atalar E. Multifunctional interventional devices for MRI: A combined electrophysiology/MRI catheter. *Magn Reson Med*. 2002;47(3):594-600. doi:10.1002/mrm.10088

107. Weiss S, Kuehne T, Brinkert F, Krombach G, Katoh M, Schaeffter T, Guenther RW, Buecker A. In vivo safe catheter visualization and slice tracking using an optically detunable resonant marker. *Magn Reson Med*. 2004;52(4):860-868. doi:10.1002/mrm.20214

108. Kocaturk O, Saikus CE, Guttman MA, Faranesh AZ, Ratnayaka K, Ozturk C, McVeigh ER, Lederman RJ. Whole shaft visibility and mechanical performance for active MR catheters using copper-nitinol braided polymer tubes. *J Cardiovasc Magn Reson*. 2009;11(1):29-38.

109. Krafft A, Müller S, Umathum R, Semmler W, Bock M. B1 field-insensitive transformers for RF-safe transmission lines. *Magn Reson Mater Phys Biol Med*. 2006;19(5):257-266. doi:10.1007/s10334-006-0055-x

110. Weiss S, Vernickel P, Schaeffter T, Schulz V, Gleich B. Transmission line for improved RF safety of interventional devices. *Magn Reson Med*. 2005;54(1):182-189. doi:10.1002/mrm.20543

111. Graesslin I, Homann H, Biederer S, Börnert P, Nehrke K, Vernickel P, Mens G, Harvey P, Katscher U. A specific absorption rate prediction concept for parallel transmission MR. *Magn Reson Med*. 2012;68(5):1664-1674. doi:10.1002/mrm.24138

112. Nelder JA, Mead R. A Simplex Method for Function Minimization. *Comput J*. 1965;7(4):308-313. doi:10.1093/comjnl/7.4.308

113. Rezai AR, Finelli D, Nyenhuis JA, Hrdlicka G, Tkach J, Sharan A, Rugieri P, Stypulkowski PH, Shellock FG. Neurostimulation systems for deep brain stimulation: In vitro evaluation of magnetic resonance imaging-related heating at 1.5 Tesla. *J Magn Reson Imaging*. 2002;15(3):241-250. doi:10.1002/jmri.10069

114. Nordbeck P, Weiss I, Ehses P, Ritter O, Warmuth M, Fidler F, Herold V, Jakob PM, Ladd ME, Quick HH, Bauer WR. Measuring RF-induced currents inside implants: Impact of device configuration on MRI safety of cardiac pacemaker leads. *Magn Reson Med*. 2009;61(3):570-578. doi:10.1002/mrm.21881

115. van den Bosch MR, Moerland MA, Lagendijk JJW, Bartels LW, van den Berg CAT. New method to monitor RF safety in MRI-guided interventions based on RF induced image artefacts. *Med Phys*. 2010;37(2):814-821. doi:10.1118/1.3298006

116. Venook RD, Overall WR, Shultz K, Conolly S, Pauly JM, Scott GC. Monitoring Induced Currents on Long Conductive Structures During MRI. In: *Intl. Soc. Mag. Reson. Med*. Vol 16. ; 2008:898.

117. Griffin GH, Anderson KJT, Celik H, Wright GA. Safely assessing radiofrequency heating potential of conductive devices using image-based current measurements. *Magn Reson Med*. 2015;73(1):427-441. doi:10.1002/mrm.25103

118. Griffin GH, Ramanan V, Barry J, Wright GA. Toward in vivo quantification of induced RF currents on long thin conductors. *Magn Reson Med*. 2018;80(5):1922-1934. doi:10.1002/mrm.27195

119. Overall WR, Pauly JM, Stang PP, Scott GC. Ensuring safety of implanted devices under MRI using reversed RF polarization. *Magn Reson Med*. 2010;64(3):823-833. doi:10.1002/mrm.22468

120. Silemek B, Acikel V, Oto C, Alipour A, Aykut ZG, Algin O, Atalar E. A temperature sensor implant for active implantable medical devices for in vivo subacute heating tests under MRI. *Magn Reson Med*. 2018;79(5):2824-2832. doi:10.1002/mrm.26914

121. Sadeghi-Tarakameh A, DelaBarre L, Zulkarnain NIH, Harel N, Eryaman Y. Implant-Friendly Excitation Strategies for Imaging DBS Electrodes at 7T. In: *Intl. Soc. Mag. Reson. Med.* ; 2021:414.

122. Griswold MA, Jakob PM, Heidemann RM, Nittka M, Jellus V, Wang J, Kiefer B, Haase A. Generalized autocalibrating partially parallel acquisitions (GRAPPA). *Magn Reson Med*. 2002;47(6):1202-1210. doi:10.1002/mrm.10171

123. Nordbeck P, Fidler F, Weiss I, Warmuth M, Friedrich MT, Ehses P, Geistert W, Ritter O, Jakob PM, Ladd ME, Quick HH, Bauer WR. Spatial distribution of RF-induced E-fields and implant heating in MRI. *Magn Reson Med*. 2008;60(2):312-319. doi:https://doi.org/10.1002/mrm.21475

124. Zanchi MG, Venook R, Pauly JM, Scott GC. An Optically Coupled System for Quantitative Monitoring of MRI-Induced RF Currents Into Long Conductors. *IEEE Trans Med Imaging*. 2010;29(1):169-178. doi:10.1109/TMI.2009.2031558

125. Vaughan J t., Garwood M, Collins C m., Liu W, DelaBarre L, Adriany G, Andersen P, Merkle H, Goebel R, Smith M b., Ugurbil K. 7T vs. 4T: RF power, homogeneity, and signal-to-noise comparison in head images. *Magn Reson Med*. 2001;46(1):24-30. doi:10.1002/mrm.1156

126. Vaughan JT, Hetherington HP, Otu JO, Pan JW, Pohost GM. High frequency volume coils for clinical NMR imaging and spectroscopy. *Magn Reson Med*. 1994;32(2):206-218. doi:10.1002/mrm.1910320209

127. Ibrahim TS, Lee R, Baertlein BA, Abduljalil AM, Zhu H, Robitaille PML. Effect of RF coil excitation on field inhomogeneity at ultra high fields: a field optimized TEM resonator. *Magn Reson Imaging*. 2001;19(10):1339-1347. doi:10.1016/S0730-725X(01)00404-0

128. Vaughan T, DelaBarre L, Snyder C, Tian J, Akgun C, Shrivastava D, Liu W, Olson C, Adriany G, Strupp J, Andersen P, Gopinath A, van de Moortele PF, Garwood M, Ugurbil K. 9.4T human MRI: Preliminary results. *Magn Reson Med*. 2006;56(6):1274-1282. doi:10.1002/mrm.21073

129. Feng K, Hollingsworth NA, McDougall MP, Wright SM. A 64-Channel Transmitter for Investigating Parallel Transmit MRI. *IEEE Trans Biomed Eng*. 2012;59(8):2152-2160. doi:10.1109/TBME.2012.2196797

130. Orzada S, Solbach K, Gratz M, Brunheim S, Fiedler TM, Johst S, Bitz AK, Shooshtary S, Abuelhaija A, Voelker MN, Rietsch SHG, Kraff O, Maderwald S, Flöser M, Oehmigen M, Quick HH, Ladd ME. A 32-channel parallel transmit system add-on for 7T MRI. *PLOS ONE*. 2019;14(9):e0222452. doi:10.1371/journal.pone.0222452

131. Kühne A. *Parallel Transmission in MRI: Electromagnetic Considerations and Advances in Signal Chain Hardware*. Otto-von-Guericke-University Magdeburg; 2016.

132. Kuehne A, Waxmann P, Hoffmann W, Pfeiffer H, Seemann R, Seifert F, Speck O, Ittermann B. It goes to 11: A scalable home-built transmit array beyond eight channels. In: *Proc. Intl. Soc. Mag. Reson. Med*. Vol 23. ; 2015:3147.

133. Silemek B. pTx implant safety testbed console repository. Published January 11, 2023. Accessed March 17, 2023. https://gitlab1.ptb.de/mri-lab/ptx-implant-safety-testbed

134. Seifert F, Pfeiffer H, Mekle R, Waxmann P, Ittermann B. 7T 8-Channel PTx Head Coil with High B1+ Efficiency Optimized for MRS. In: *24th Annual Meeting of ISMRM*. ; 2016:3545.

135. Han H, Moritz R, Oberacker E, Waiczies H, Niendorf T, Winter L. Open Source 3D Multipurpose Measurement System with Submillimetre Fidelity and First Application in Magnetic Resonance. *Sci Rep*. 2017;7(1):13452. doi:10.1038/s41598-017-13824-z

136. Taber KH, Hayman LA. Temperature monitoring during MR imaging: Comparison of fluoroptic and standard thermistors. *J Magn Reson Imaging*. 1992;2(1):99-101. doi:10.1002/jmri.1880020119

137. Standard Commands for Programmable Instruments (SCPI). Published online May 1999. Accessed March 5, 2022. https://www.ivifoundation.org/docs/scpi-99.pdf

138. Steinhart JS, Hart SR. Calibration curves for thermistors. *Deep Sea Res Oceanogr Abstr*. 1968;15(4):497-503. doi:10.1016/0011-7471(68)90057-0

139. Klepsch T, Linde TD, Hoffmann W, Botterweck H, Ittermann B, Seifert F. Calibration of fibre-optic RF E/H-field probes using a magnetic resonance (MR) compatible TEM cell and dedicated MR measurement techniques. *Biomed Eng Biomed Tech*. 2012;57(SI-1-Track-B). doi:10.1515/bmt-2012-4428

140. Silemek B, Winter L, Seifert F, Pfeiffer H, Ittermann B. Measurement based mitigation of RF related safety hazards of implants in parallel transmission using temperature matrix. In: *ISMRM Workshop on MR Safety: Ensuring Safety from First Principles to Best Practices*. ; 2019.

141. Silemek B, Winter L, Seifert F, Pfeiffer H, Ittermann B. Measurement-based safety assessment, prediction and mitigation of RF induced implant heating

with parallel transmission: temperature matrix. In: *28th Annual Meeting of ISMRM*. ; 2020:1135.

142. Silemek B, Winter L, Seifert F, Pfeiffer H, Seemann R, Hoffmann W, Ittermann B. Real-time safety assessment and mitigation of RF induced implant heating with parallel transmission and low-cost RMS sensors. In: *28th Annual Meeting of ISMRM*. ; 2020:4196.

143. Silemek B, Seifert F, Ittermann B, Winter L. Safe scanning of elongated implants with the sensor matrix Qs: Comparison of orthogonal projection and null mode based pTx mitigation. In: *29th Annual Meeting of ISMRM*. ; 2021:362.

144. Teixeira NJ, Godinez F, Malik SJ, Hajnal JV. Exploring the impact of nulling currents on a cardiac guidewire in reducing worst case SAR at 1.5T. In: *Proc. Intl. Soc. Mag. Reson. Med*. Vol 26 (2018). ; :299.

145. Teixeira NJ, Godinez F, Malik SJ, Hajnal JV. Planning Current Nulling for Worst Case SAR reduction in a Cardiac Guidewire Scenario at 1.5T. In: *Proc. Intl. Soc. Mag. Reson. Med*. Vol 27 (2019). ; :4179.

146. Graesslin I, Krueger S, Vernickel P, Achtzehn J, Nehrke K, Weiss S. Detection of RF unsafe devices using a parallel transmission MR system. *Magn Reson Med*. 2013;70(5):1440-1449. doi:10.1002/mrm.24558

147. Graesslin I, Vernickel P, Börnert P, Nehrke K, Mens G, Harvey P, Katscher U. Comprehensive RF safety concept for parallel transmission MR. *Magn Reson Med*. 2015;74(2):589-598. doi:10.1002/mrm.25425

148. Ellenor CW, Stang PP, Etezadi-Amoli M, Pauly JM, Scott GC. Offline impedance measurements for detection and mitigation of dangerous implant interactions: An RF safety prescreen. *Magn Reson Med*. 2015;73(3):1328-1339. doi:10.1002/mrm.25202

149. Weidemann G, Seifert F, Ittermann B. Reduction of the E field at the tip of implanted wires generated by pTx coils using RF current measurements. In:

24th Annual Meeting of ISMRM. ; 2016:2216. http://archive.ismrm.org/2016/2216.html

150. Silemek B, Açıkel V, Atalar E. RF safety of active implantable medical devices. *eMagRes*. 2019;8(2):103-120. doi:10.1002/9780470034590.emrstm1587

151. Yeung CJ, Atalar E. A Green's function approach to local rf heating in interventional MRI. *Med Phys*. 2001;28(5):826-832. doi:10.1118/1.1367860

152. Boulant N, Wu X, Adriany G, Schmitter S, Uğurbil K, Van De Moortele PF. Direct control of the temperature rise in parallel transmission by means of temperature virtual observation points: Simulations at 10.5 tesla. *Magn Reson Med*. 2016;75(1):249-256. doi:10.1002/mrm.25637

153. Bassen H, Smith G. Electric field probes–A review. *IEEE Trans Antennas Propag*. 1983;31(5):710-718. doi:10.1109/TAP.1983.1143126

154. Stuchly MA, Kraszewski A, Stuchly SS. Implantable Electric-Field Probes - Some Performance Characteristics. *IEEE Trans Biomed Eng*. 1984;BME-31(7):526-531. doi:10.1109/TBME.1984.325294

155. R. S. J. P. KAATEE GCVR. An electric field measurement system, using a two-dimensional array of diodes. *Int J Hyperthermia*. 1999;15(5):441-454. doi:10.1080/026567399285620

156. Iwasawa J, Koruth JS, Petru J, Dujka L, Kralovec S, Mzourkova K, Dukkipati SR, Neuzil P, Reddy VY. Temperature-Controlled Radiofrequency Ablation for Pulmonary Vein Isolation in Patients With Atrial Fibrillation. *J Am Coll Cardiol*. 2017;70(5):542-553. doi:10.1016/j.jacc.2017.06.008

157. Kautzner J, Albenque JP, Natale A, Maddox W, Cuoco F, Neuzil P, Poty H, Getman MK, Liu S, Starek Z, Dukkipati SR, Colley BJ, Al-Ahmad A, Sidney DS, McElderry HT. A Novel Temperature-Controlled Radiofrequency Catheter Ablation System Used to Treat Patients With Paroxysmal Atrial Fibrillation. *JACC Clin Electrophysiol*. 2021;7(3):352-363. doi:10.1016/j.jacep.2020.11.009

158. Wang Q, Kong W, Yao J, Chang A. Fabrication and electrical properties of the fast response Mn1.2Co1.5Ni0.3O4 miniature NTC chip thermistors. *Ceram Int*. 2019;45(1):378-383. doi:10.1016/j.ceramint.2018.09.177

159. Smith GS. Analysis of Miniature Electric Field Probes with Resistive Transmission Lines. *IEEE Trans Microw Theory Tech*. 1981;29(11):1213-1224. doi:10.1109/TMTT.1981.1130534

160. Meier K, Burkhardt M, Schmid T, Kuster N. Broadband calibration of E-field probes in lossy media. *IEEE Trans Microw Theory Tech*. 1996;44(10):1954-1962. doi:10.1109/22.539955

161. Eichfelder G, Gebhardt M. Local specific absorption rate control for parallel transmission by virtual observation points. *Magn Reson Med*. 2011;66(5):1468-1476. doi:https://doi.org/10.1002/mrm.22927

162. Petzold J, Schmitter S, Silemek B, Winter L, Speck O, Ittermann B, Seifert F. Towards an integrated RF safety concept for implant carriers in MRI based on sensor-equipped implants and parallel transmission. *NMR Biomed*.:e4900. doi:10.1002/nbm.4900

163. Tokaya JP, Raaijmakers AJE, Luijten PR, Bakker JF, Berg CAT van den. MRI-based transfer function determination for the assessment of implant safety. *Magn Reson Med*. 2017;78(6):2449-2459. doi:https://doi.org/10.1002/mrm.26613

164. Yao A, Zastrow E, Neufeld E, Kuster N. Efficient and Reliable Assessment of the Maximum Local Tissue Temperature Increase at the Electrodes of Medical Implants under MRI Exposure. *Bioelectromagnetics*. 2019;40(6):422-433. doi:https://doi.org/10.1002/bem.22208

165. Mukherjee RK, Chubb H, Roujol S, Razavi R, O'Neill MD. Advances in Real-Time MRI–Guided Electrophysiology. *Curr Cardiovasc Imaging Rep*. 2019;12(2):6. doi:10.1007/s12410-019-9481-9

166. Zuehlsdorff S, Umathum R, Volz S, Hallscheidt P, Fink C, Semmler W, Bock M. MR coil design for simultaneous tip tracking and curvature delineation of a catheter. *Magn Reson Med*. 2004;52(1):214-218. doi:https://doi.org/10.1002/mrm.20108

167. Silemek B, Seifert F, Ittermann B, Winter L. Wireless reference implant and communication methodology to assess and investigate RF safety and pTx mitigation strategies for AIMDs. In: *Proc. Intl. Soc. Mag. Reson. Med*. Vol 30. ; 2022:2010.

168. Silemek B, Seifert F, Brühl R, Guerin B, Montag R, Ittermann B, Winter L. Mitigation of RF-induced heating on realistic deep brain stimulator lead trajectories by wireless sensor Q-matrix and parallel transmission. In: *Proc. Intl. Soc. Mag. Reson. Med*. Vol 30. ; 2022:2009.

169. Silemek B, Seifert F, Petzold J, Ittermann B, Winter L. Smart Implants Interfaced with MR Scanners to Improve Implant Safety. In: *ISMRM Workshop on MR Safety: From Physics & Physiology to Policies & Practice*. ; 2022.

170. Silemek B. Smart implants and parallel transmission MRI for improved RF-safety and diagnostic imaging. In: *24. Jahrestagung Der Deutschen Sektion Der ISMRM*. Vol 24. ; 2022:47-52. Accessed December 26, 2022. https://dgmp-kongress.de/fileadmin/media/dgmp/pdf/Abstractband_DS-ISMRM2022_22-09-04_web.pdf#page=38

171. Mittendorff L, Young A, Sim J. A narrative review of current and emerging MRI safety issues: What every MRI technologist (radiographer) needs to know. *J Med Radiat Sci*. 2022;69(2):250-260. doi:10.1002/jmrs.546

172. Turner S, Singh SM. Skin burn after magnetic resonance imaging in a patient with an implantable cardioverter-defibrillator. *Hear Case Rep*. 2022;8(7):539-540. doi:10.1016/j.hrcr.2022.05.023

173. Tsunekawa Y, Sato H, Koyama C, Oka Y, Toriyama K. Breast reconstruction in a patient with an implanted deep brain stimulator. *JPRAS Open*. 2020;24:56-59. doi:10.1016/j.jpra.2020.03.007

174. Nelson BD, Karipott SS, Wang Y, Ong KG. Wireless Technologies for Implantable Devices. *Sensors*. 2020;20(16):4604. doi:10.3390/s20164604

175. Taleb H, Nasser A, Andrieux G, Charara N, Motta Cruz E. Wireless technologies, medical applications and future challenges in WBAN: a survey. *Wirel Netw*. 2021;27(8):5271-5295. doi:10.1007/s11276-021-02780-2

176. Medtronic. Cardiac Device Features - BlueSync Technology. Accessed February 26, 2021. https://europe.medtronic.com/xd-en/healthcare-professionals/therapies-procedures/cardiac-rhythm/cardiac-device-features/bluesync-technology.html

177. Vercise™ Genus DBS. www.bostonscientific.com. Accessed February 26, 2021. https://www.bostonscientific.com/en-EU/products/deep-brain-stimulation-systems/vercise-genus-dbs.html

178. About the Gallant ICD. Accessed August 27, 2022. https://www.cardiovascular.abbott/us/en/hcp/products/cardiac-rhythm-management/implantable-cardioverter-defibrillators/gallant/about.html

179. Luechinger R, Zeijlemaker VA, Pedersen EM, Mortensen P, Falk E, Duru F, Candinas R, Boesiger P. In vivo heating of pacemaker leads during magnetic resonance imaging. *Eur Heart J*. 2005;26(4):376-383. doi:10.1093/eurheartj/ehi009

180. Paff M, Loh A, Sarica C, Lozano AM, Fasano A. Update on Current Technologies for Deep Brain Stimulation in Parkinson's Disease. *J Mov Disord*. 2020;13(3):185-198. doi:10.14802/jmd.20052

181. Zhang J, Hu W, Chen H, Meng F, Li L, Okun MS. Implementation of a Novel Bluetooth Technology for Remote Deep Brain Stimulation Programming: The Pre– and Post–COVID-19 Beijing Experience. *Mov Disord*. 2020;35(6):909-910. doi:10.1002/mds.28098

182. Boston Scientific. *ImageReady MRI Guidelines for Boston Scientific Deep Brain Stimulation Systems*.; 2019.

https://www.bostonscientific.com/content/dam/Manuals/us/current-rev-en/92195369-01_ImageReady%E2%84%A2_MRI_Guidelines_for_Boston_Scientific_Deep_Brain_Stimulation_Systems_en-US_s.pdf

183. Abbott. *MRI Procedure Information for Abbott Medical MR Conditional Deep Brain Stimulation*.; 2020. https://manuals.sjm.com/Search-Form?re=North-America&cc=US&ln=all&ct=professional&qry=DBS&ipp=10

184. SimpleLink CC13x2 and CC26x2 software development kit. Published online January 29, 2021. Accessed January 15, 2022. https://www.ti.com/tool/download/SIMPLELINK-CC13X2-26X2-SDK/4.40.04.04

185. Code composer studio integrated development environment. Published online August 7, 2021. Accessed January 15, 2022. https://www.ti.com/tool/CCSTUDIO

186. Bluetooth Core Specification Version 5.2 Feature Overview. Bluetooth® Technology Website. Published January 7, 2020. Accessed November 10, 2021. https://www.bluetooth.com/bluetooth-resources/bluetooth-core-specification-version-5-2-feature-overview/

187. Guerin B, Serano P, Iacono MI, Herrington TM, Widge AS, Dougherty DD, Bonmassar G, Angelone LM, Wald LL. Realistic modeling of deep brain stimulation implants for electromagnetic MRI safety studies. *Phys Med Biol*. 2018;63(9):095015. doi:10.1088/1361-6560/aabd50

188. Hintze JL, Nelson RD. Violin Plots: A Box Plot-Density Trace Synergism. *Am Stat*. 1998;52(2):181-184. doi:10.1080/00031305.1998.10480559

189. Senova S, Chaillet A, Lozano AM. Fornical Closed-Loop Stimulation for Alzheimer's Disease. *Trends Neurosci*. 2018;41(7):418-428. doi:10.1016/j.tins.2018.03.015

190. Rosin B, Slovik M, Mitelman R, Rivlin-Etzion M, Haber SN, Israel Z, Vaadia E, Bergman H. Closed-Loop Deep Brain Stimulation Is Superior in Ameliorating Parkinsonism. *Neuron*. 2011;72(2):370-384. doi:10.1016/j.neuron.2011.08.023

191. Barbier T, Piumatti R, Hecker B, Odille F, Felblinger J, Pasquier C. An RF-induced voltage sensor for investigating pacemaker safety in MRI. *Magn Reson Mater Phys Biol Med*. 2014;27(6):539-549. doi:10.1007/s10334-014-0437-4

192. Barbier T, Aissani S, Weber N, Pasquier C, Felblinger J. A novel MR-compatible sensor to assess active medical device safety: stimulation monitoring, rectified radio frequency pulses, and gradient-induced voltage measurements. *Magn Reson Mater Phys Biol Med*. 2018;31(5):677-688. doi:10.1007/s10334-018-0682-z

193. Munzer DJ, Mannem NS, Garay E, Wang H. A Broadband Mm-Wave VSWR-Resilient Joint True-Power Detector and Impedance Sensor Supporting Single-Ended Antenna Interfaces. In: *2022 IEEE International Solid- State Circuits Conference (ISSCC)*. Vol 65. ; 2022:1-3. doi:10.1109/ISSCC42614.2022.9731769

194. Ji DF, Niu B, Tao HQ, Chen TS, Wang WB. A D Band Zero Bias Detector Chip Using Schottky Diode. In: *2022 Photonics & Electromagnetics Research Symposium (PIERS)*. ; 2022:752-754. doi:10.1109/PIERS55526.2022.9792773

195. Nakamoto H, Kudo M, Niratsuka K, Mori T, Yamaura S. A real-time temperature-compensated CMOS RF on-chip power detector with high linearity for wireless applications. In: *2012 Proceedings of the ESSCIRC (ESSCIRC)*. ; 2012:349-352. doi:10.1109/ESSCIRC.2012.6341326

196. Wang Y, Zheng J, Guo R, Wang Q, Kainz W, Long S, Chen J. A technique for the reduction of RF-induced heating of active implantable medical devices during MRI. *Magn Reson Med*. 2022;87(1):349-364. doi:10.1002/mrm.28953

197. Liu J, Zheng J, Wang Q, Kainz W, Chen J. A Transmission Line Model for the Evaluation of MRI RF-Induced Fields on Active Implantable Medical Devices.

IEEE Trans Microw Theory Tech. 2018;66(9):4271-4281. doi:10.1109/TMTT.2018.2851975

198. Stone RT, Conroy MJ, Liu W, Salminen GW. Shielded implantable medical lead with guarded termination. Published online December 22, 2015. Accessed November 3, 2022. https://patents.google.com/patent/US9216286/en

199. Golestanirad L, Kirsch J, Bonmassar G, Downs S, Elahi B, Martin A, Iacono MI, Angelone LM, Keil B, Wald LL, Pilitsis J. RF-induced heating in tissue near bilateral DBS implants during MRI at 1.5 T and 3T: The role of surgical lead management. *NeuroImage*. 2019;184:566-576. doi:10.1016/j.neuroimage.2018.09.034

200. Bhidayasiri R, M. Bronstein J, Sinha S, E. Krahl S, Ahn S, J. Behnke E, S. Cohen M, Frysinger R, G. Shellock F. Bilateral neurostimulation systems used for deep brain stimulation: in vitro study of MRI-related heating at 1.5 T and implications for clinical imaging of the brain. *Magn Reson Imaging*. 2005;23(4):549-555. doi:10.1016/j.mri.2005.02.007

201. Krueger F, Aigner CS, Hammernik K, Dietrich S, Lutz M, Schulz-Menger J, Schaeffter T, Schmitter S. Rapid estimation of 2D relative B1+-maps from localizers in the human heart at 7T using deep learning. *Magn Reson Med*. n/a(n/a). doi:10.1002/mrm.29510

202. Eberhardt B, Poser BA, Shah NJ, Felder J. B1 field map synthesis with generative deep learning used in the design of parallel-transmit RF pulses for ultra-high field MRI. *Z Für Med Phys*. 2022;32(3):334-345. doi:10.1016/j.zemedi.2021.12.003

203. Abbasi-Rad S, O'Brien K, Kelly S, Vegh V, Rodell A, Tesiram Y, Jin J, Barth M, Bollmann S. Improving FLAIR SAR efficiency at 7T by adaptive tailoring of adiabatic pulse power through deep learning estimation. *Magn Reson Med*. 2021;85(5):2462-2476. doi:10.1002/mrm.28590

List of Figures

List of Tables

List of publications during the thesis

14- **Silemek, B.**, Seifert, F., Petzold J., Rüdiger, B., Ittermann, B., & Winter, L. *Wirelessly interfacing active implantable medical devices and MRI for RF-safety.* Submitted to Magn. Reson Med (2023).

13- Petzold J., Schmitter S., **Silemek B.**, et al. *Towards an integrated RF safety concept for implant carriers in MRI based on sensor-equipped implants and parallel transmission.* NMR Biomed. Early view. doi:10.1002/nbm.4900 (2023).

12- **Silemek, B.**, Seifert, F., Petzold, J., Hoffmann, W., Pfeiffer, H., Speck, O., Georg, R., Ittermann, B. & Winter, L. *Rapid safety assessment and mitigation of radiofrequency induced implant heating using small RMS sensors and the sensor matrix* $\boldsymbol{Q_S}$*.* Magn. Reson Med. 87, 509–527 (2022).

11- Wenzel, K., Alhamwey, H., O'Reilly, T., Riemann, L., **Silemek, B.** & Winter, L. *B0-shimming methodology for affordable and compact low-field magnetic resonance imaging magnets.* Front. Phys. Med. Phys. Imag., https://doi.org/10.3389/fphy.2021.704566 (2021).

10- Winter*, L., **Silemek, B.***, Seifert, F., Petzold, J., Pfeiffer, H., Hoffmann, W. & Ittermann, B. *Parallel transmission (pTx) medical implant safety testbed: real-time mitigation of RF induced tip heating using time-domain E-field sensors.* Magnetic Resonance in Medicine 84, 3468–3484 (2020).

9- Özen, A., **Silemek, B.**, Lottner, T., Atalar, E. & Bock, M. *MR safety watchdog for active catheters: wireless impedance control with real-time Feedback.* Magnetic Resonance in Medicine 84, 1048–1060 (2020).

8- **Silemek, B.**, Seifert, F., Ittermann, B. & Winter, L. Smart implants and parallel transmission MRI for improved RF-safety and diagnostic imaging. in 53. Jahrestagung der Deutschen Gesellschaft für Medizinische Physik & 24. Jahrestagung der Deutschen Sektion der ISMRM. (Aachen, Germany, 2022).

7- **Silemek, B.**, Seifert, F., Brühl, R., Guerin, B., Montag, R., Ittermann, B. & Winter, L. *Mitigation of RF-induced heating on realistic deep brain stimulator lead trajectories by wireless sensor Q-matrix and parallel transmission.* in Proceedings of the Joint Annual Meeting of ISMRM EMSRMB (London, UK, 2022), 2010.

6- **Silemek, B.**, Seifert, F., Ittermann, B. & Winter, L. *Wireless reference implant and communication methodology to assess and investigate RF safety and pTx mitigation strategies for AIMDs.* in Proceedings of the Joint Annual Meeting of ISMRM-EMSRMB (London, UK, 2022), 2009.

5- **Silemek, B.**, Seifert, F., Ittermann, B. & Winter, L. *Safe scanning of elongated implants with the sensor matrix Qs: Comparison of orthogonal projection and null*

mode based pTx mitigation. in Proceedings of the 29th Annual Meeting of ISMRM (Virtual, 2021),362.

4- **Silemek, B.**, Winter, L., Seifert, F., Pfeiffer, H. & Ittermann, B. *Measurement-based safety assessment, prediction and mitigation of RF induced implant heating with parallel transmission: temperature matrix*. in Proceedings of the 28th Annual Meeting of ISMRM (Virtual, 2020), 1135.

3- **Silemek, B.**, Winter, L., Seifert, F., Pfeiffer, H., Seemann, R., Hoffmann, W. & Ittermann, B. *Real-time safety assessment and mitigation of RF induced implant heating with parallel transmission and low-cost RMS sensors*. in Proceedings of the 28th Annual Meeting of ISMRM (Virtual, 2020), 4196.

2-Özen, A., **Silemek, B.**, Lottner, T., Atalar, E. & Bock, M. *MR Safety watchdog for safe active catheters: wireless impedance controller with real-time feedback*. in Proceedings of the 27th Annual Meeting of ISMRM (Montreal, Quebec, Canada, 2019), 792.

1-**Silemek, B.**, Winter, L., Seifert, F., Pfeiffer, H. & Ittermann, B. *Measurement-Based Mitigation of RF Related Safety Hazards of Implants in Parallel Transmission Using Temperature Matrix*. in ISMRM Workshop on MR Safety (Utrecht, Netherlands, 2019).

Declaration of Honor

„I hereby declare that I produced this thesis without prohibited external assistance and that none other than the listed references and tools have been used. I did not make use of any commercial consultant concerning graduation. A third party did not receive any nonmonetary perquisites neither directly nor indirectly for activities which are connected with the contents of the presented thesis.

All sources of information are clearly marked, including my own publications.

In particular I have not consciously:

- Fabricated data or rejected undesired results

- Misused statistical methods with the aim of drawing other conclusions than those warranted by the available data

- Plagiarized data or publications

- Presented the results of other researchers in a distorted way

I do know that violations of copyright may lead to injunction and damage claims of the author and also to prosecution by the law enforcement authorities. I hereby agree that the thesis may need to be reviewed with an electronic data processing for plagiarism. This work has not yet been submitted as a doctoral thesis in the same or a similar form in Germany or in any other country. It has not yet been published as a whole."

Magdeburg, 25.04.2023